

**TIC 172900988: A Transiting Circumbinary Planet Detected in One Sector of TESS Data**

Veselin B. Kostov^{1,2,3} , Brian P. Powell¹ , Jerome A. Orosz⁴ , William F. Welsh⁴ , William Cochran^{5,6} , Karen A. Collins⁷ , Michael Endl⁶ , Coel Hellier⁸ , David W. Latham⁷ , Phillip MacQueen⁶ , Joshua Pepper⁹ , Billy Quarles^{10,11} , Lalitha Sairam¹² , Guillermo Torres⁷ , Robert F. Wilson¹³ , Serge Bergeron¹⁴ , Pat Boyce¹⁵ , Allyson Bieryla⁷ , Robert Buchheim¹⁶ , Caleb Ben Christiansen⁴ , David R. Ciardi¹⁷ , Kevin I. Collins¹⁸ , Dennis M. Conti³⁵ , Scott Dixon²⁰ , Pere Guerra²¹ , Nader Haghighipour^{22,23} , Jeffrey Herman²⁰ , Eric G. Hintz²⁴ , Ward S. Howard²⁵ , Eric L. N. Jensen²⁶ , John F. Kielkopf²⁷ , Ethan Kruse¹ , Nicholas M. Law²⁵ , David Martin^{28,65} , Pierre F. L. Maxted²⁹ , Benjamin T. Montet^{30,31} , Felipe Murgas^{32,33} , Matt Nelson¹³ , Greg Olmschenk^{1,34} , Sebastian Otero¹⁹ , Robert Quimby⁴ , Michael Richmond³⁶ , Richard P. Schwarz³⁷ , Avi Shporer³⁸ , Keivan G. Stassun³⁹ , Denise C. Stephens⁴⁰ , Amaury H. M. J. Triaud¹² , Joe Ulowetz⁴¹ , Bradley S. Walter⁴² , Edward Wiley⁴³ , David Wood²⁰ , Mitchell Yenawine⁴ , Eric Agol⁴⁴ , Thomas Barclay^{1,45} , Thomas G. Beatty⁴⁶ , Isabelle Boisse⁴⁷ , Douglas A. Caldwell² , Jessie Christiansen¹⁷ , Knicole D. Colón¹ , Magali Deleuil⁴⁷ , Laurance Doyle² , Michael Fausnaugh³⁸ , Gábor Fűrész³⁸ , Emily A. Gilbert^{1,3,45,48,49} , Guillaume Hébrard⁵⁰ , David J. James⁵¹ , Jon Jenkins⁵² , Stephen R. Kane⁵³ , Richard C. Kidwell Jr.⁵⁴ , Ravi Kopparapu¹ , Gongjie Li¹⁰ , Jack J. Lissauer⁵⁵ , Michael B. Lund⁵⁶ , Steve R. Majewski¹³ , Tsevi Mazeh⁵⁷ , Samuel N. Quinn⁷ , Elisa Quintana¹ , George Ricker³⁸ , Joseph E. Rodriguez⁵⁸ , Jason Rowe⁵⁹ , Alexander Santerne⁴⁷ , Joshua Schlieder¹ , Sara Seager^{38,60,61} , Matthew R. Standing¹² , Daniel J. Stevens^{62,63,66} , Eric B. Ting⁵² , Roland Vanderspek³⁸ , and Joshua N. Winn⁶⁴

¹ NASA Goddard Space Flight Center, 8800 Greenbelt Road, Greenbelt, MD 20771, USA; veselin.b.kostov@nasa.gov

² SETI Institute, 189 Bernardo Avenue, Suite 200, Mountain View, CA 94043, USA

³ GSFC Sellers Exoplanet Environments Collaboration, USA

⁴ Department of Astronomy, San Diego State University, 5500 Campanile Drive, San Diego, CA 92182, USA

⁵ Center for Planetary Systems Habitability and McDonald Observatory, The University of Texas, Austin, TX 78712, USA

⁶ McDonald Observatory, The University of Texas, Austin, TX 78712-0259, USA

⁷ Center for Astrophysics, Harvard & Smithsonian, 60 Garden Street, Cambridge, MA 02138, USA

⁸ Astrophysics Group, Keele University, Staffordshire, ST5 5BG, UK

⁹ Department of Physics, Lehigh University, 413 Deming Lewis Lab, 16 Memorial Drive, East Bethlehem, PA 18015, USA

¹⁰ Center for Relativistic Astrophysics, School of Physics, Georgia Institute of Technology, 770 State Street NW, Atlanta, GA 30313, USA

¹¹ Department of Physics, Astronomy, Geosciences and Engineering Technology, Valdosta State University, GA 31698, USA

¹² School of Physics & Astronomy, University of Birmingham, Edgbaston, Birmingham B15 2TT, UK

¹³ Department of Astronomy, University of Virginia, 530 McCormick Road, Charlottesville, VA 22904, USA

¹⁴ UCLAN, Casselman, Ontario, Canada

¹⁵ Boyce Research Initiatives and Education Foundation, 3540 Carleton Street, San Diego, CA 92106, USA

¹⁶ Lost Gold Observatory, Society for Astronomical Sciences, Gold Canyon, AZ 85118, USA

¹⁷ NASA Exoplanet Science Institute—Caltech-IPAC, 1200 E California Avenue, MS100-22 Pasadena, CA 91125, USA

¹⁸ George Mason University, 4400 University Drive, Fairfax, VA 22030, USA

¹⁹ American Association of Variable Star Observers, USA

²⁰ San Diego Astronomy Association, P.O. Box 23215, San Diego, CA 92193-3215, USA

²¹ Observatori Astronòmic Albanyá, Camí de Bassegoda S/N, Albanyá E-17733, Girona, Spain

²² Planetary Science Institute, 1700 East Fort Lowell, Tucson, AZ 85719, USA

²³ Institute for Astronomy, University of Hawaii—Manoa, 2680 Woodlawn Drive, Honolulu, HI 96822, USA

²⁴ Department of Physics and Astronomy, Brigham Young University, Provo, UT 84602, USA

²⁵ Department of Astronomy, University of North Carolina at Chapel Hill, Phillips Hall, CB #3255, 120 E. Cameron Avenue, Chapel Hill, NC 27599, USA

²⁶ Department of Physics & Astronomy, Swarthmore College, Swarthmore, PA 19081, USA

²⁷ Department of Physics and Astronomy, University of Louisville, Louisville, KY 40292, USA

²⁸ Department of Astronomy, The Ohio State University, 4055 McPherson Laboratory, Columbus, OH 43210, USA

²⁹ Keele University, Staffordshire, ST5 5BG, UK

³⁰ School of Physics, University of New South Wales, Sydney NSW 2052, Australia

³¹ UNSW Data Science Hub, University of New South Wales, Sydney, NSW 2052, Australia

³² Instituto de Astrofísica de Canarias (IAC), E-38205 La Laguna, Tenerife, Spain

³³ Departamento de Astrofísica, Universidad de La Laguna (ULL), E-38206 La Laguna, Tenerife, Spain

³⁴ Universities Space Research Association, 7178 Columbia Gateway Drive, Columbia, MD 21046, USA

³⁵ American Association of Variable Star Observers, 49 Bay State Road, Cambridge, MA 02138, USA

³⁶ School of Physics and Astronomy, Rochester Institute of Technology, RIT Observatory, USA

³⁷ Patashnick Voorheesville Observatory, Voorheesville, NY 12186, USA

³⁸ Department of Physics and Kavli Institute for Astrophysics and Space Research, Massachusetts Institute of Technology, Cambridge, MA 02139, USA

³⁹ Department of Physics & Astronomy, Vanderbilt University, 6301 Stevenson Center Lane, Nashville, TN 37235, USA

⁴⁰ Brigham Young University, N486 ESC, Provo, UT 84602, USA

⁴¹ Center for Backyard Astrophysics, 855 Fair Lane, Northbrook, IL 60062, USA

⁴² Central Texas Astronomical Society, Paul and Jane Meyer Observatory, Waco TX, USA

⁴³ Stellar Skies Observatories, AAVSO, 125 Mountain Creek Pass, Georgetown, TX 78633, USA

⁴⁴ Department of Astronomy, University of Washington, USA

⁴⁵ University of Maryland, Baltimore County, 1000 Hilltop Circle, Baltimore, MD 21250, USA

⁴⁶ Department of Astronomy and Steward Observatory, University of Arizona, Tucson, AZ 85721, USA

⁴⁷ Aix Marseille Univ CNRS CNES LAM Marseille, France

⁴⁸ Department of Astronomy and Astrophysics, University of Chicago, 5640 S. Ellis Avenue, Chicago, IL 60637, USA

⁴⁹ The Adler Planetarium, 1300 South Lakeshore Drive, Chicago, IL 60605, USA

⁵⁰ Institut d'Astrophysique de Paris, UMR7095 CNRS, Université Pierre & Marie Curie, 98bis boulevard Arago, F-75014 Paris, France

⁵¹ ASTRAVEO LLC, P.O. Box 1668, MA 01931, France⁵² NASA Ames Research Center, Moffett Field, CA 94035, USA⁵³ Department of Earth and Planetary Sciences, University of California, Riverside, 900 University Avenue, Riverside, CA 92521, USA⁵⁴ Mikulski Archive for Space Telescopes, Space Telescope Science Institute, USA⁵⁵ Space Science and Astrobiology Division, MS 245-3, NASA Ames Research Center, Moffett Field, CA 94035, USA⁵⁶ NASA Exoplanet Science Institute, Caltech/IPAC 1200 E. California Avenue, Pasadena, CA 91125, USA⁵⁷ Department of Astronomy and Astrophysics, Tel Aviv University, 69978 Tel Aviv, Israel⁵⁸ Department of Physics and Astronomy, Michigan State University, East Lansing, MI 48824, USA⁵⁹ Department of Physics and Astronomy, Bishop's University, 2600 College Street, Sherbrooke, QC J1M 1Z7, Canada⁶⁰ Department of Earth, Atmospheric and Planetary Sciences, Massachusetts Institute of Technology, Cambridge, MA 02139, USA⁶¹ Department of Aeronautics and Astronautics, MIT, 77 Massachusetts Avenue, Cambridge, MA 02139, USA⁶² Center for Exoplanets and Habitable Worlds, The Pennsylvania State University, 525 Davey Lab, University Park, PA 16802, USA⁶³ Department of Astronomy & Astrophysics, The Pennsylvania State University, 525 Davey Lab, University Park, PA 16802, USA⁶⁴ Department of Astrophysical Sciences, Princeton University, Princeton, NJ 08544, USA

Received 2021 May 13; revised 2021 August 18; accepted 2021 August 26; published 2021 November 10

Abstract

We report the first discovery of a transiting circumbinary planet detected from a single sector of Transiting Exoplanet Survey Satellite (TESS) data. During Sector 21, the planet TIC 172900988b transited the primary star and then five days later it transited the secondary star. The binary is itself eclipsing, with a period $P \approx 19.7$ days and an eccentricity $e \approx 0.45$. Archival data from ASAS-SN, Evryscope, KELT, and SuperWASP reveal a prominent apsidal motion of the binary orbit, caused by the dynamical interactions between the binary and the planet. A comprehensive photodynamical analysis of the TESS, archival and follow-up data yields stellar masses and radii of $M_1 = 1.2384 \pm 0.0007 M_\odot$ and $R_1 = 1.3827 \pm 0.0016 R_\odot$ for the primary and $M_2 = 1.2019 \pm 0.0007 M_\odot$ and $R_2 = 1.3124 \pm 0.0012 R_\odot$ for the secondary. The radius of the planet is $R_3 = 11.25 \pm 0.44 R_\oplus$ ($1.004 \pm 0.039 R_{\text{Jup}}$). The planet's mass and orbital properties are not uniquely determined—there are six solutions with nearly equal likelihood. Specifically, we find that the planet's mass is in the range of $824 \lesssim M_3 \lesssim 981 M_\oplus$ ($2.65 \lesssim M_3 \lesssim 3.09 M_{\text{Jup}}$), its orbital period could be 188.8, 190.4, 194.0, 199.0, 200.4, or 204.1 days, and the eccentricity is between 0.02 and 0.09. At $V = 10.141$ mag, the system is accessible for high-resolution spectroscopic observations, e.g., the Rossiter–McLaughlin effect and transit spectroscopy.

Unified Astronomy Thesaurus concepts: [Exoplanet detection methods \(489\)](#); [Exoplanets \(498\)](#); [Exoplanet astronomy \(486\)](#); [Eclipsing binary stars \(444\)](#)

1. Introduction

Long before Kepler's discovery of transiting circumbinary planets (CBPs, Doyle et al. 2011; Welsh & Orosz 2018), Schneider & Chevreton (1990) discussed an unusual observational signature such planets would have—the occurrence of multiple transits during one conjunction. This effect is caused by the planet transiting one or both stars of the host eclipsing binary (EB) several times over the course of a fraction of its orbital period. The configuration of such transits depends on the relative sky-projected velocities of the CBP and the stars being transited. Importantly, the orbital period of the CBP can be estimated from such transits provided the host system is a double-lined spectroscopic binary, as argued by Schneider & Chevreton (1990) and Kostov et al. (2020b), and demonstrated in Kostov et al. (2016). In this methodology, the radial velocities of both the primary and secondary stars are required to calculate the sky positions of the transited star(s) during the observed transits. The situation is similar to that of triply eclipsing stellar triples that produce multiple sets of eclipses and occultations (e.g., Marsh et al. 2014; Borkovits et al. 2020).

Several groups attempted to detect transits of circumbinary planets (CBP) from the ground before the turn of the century—single conjunction or otherwise—but were ultimately hampered by the limited time sampling (e.g., Doyle et al. 1996; Deeg et al. 1997). Fortunately, thanks to its long dwell time and high photometric precision, NASA's Kepler mission enabled the discovery of roughly a dozen transiting CBPs and also

demonstrated that the occurrence of pairs of transits during one conjunction is common. Four of the eleven known Kepler CBP systems exhibit such transits—Kepler-16, -34, -35, and -1647 (see Kostov et al. 2020b for more details).

Kostov et al. (2020a) recently found a transiting CBP (TOI-1338b) using data from the Transiting Exoplanet Survey Satellite (TESS, Ricker et al. 2015), highlighting its detection potential. By virtue of residing in the southern continuous viewing zone of TESS,⁶⁷ TOI-1338b was observed in 12 consecutive sectors (about 336 days). This provided sufficient observational coverage for this CBP to be at conjunction three times and produce one transit across the primary star at each conjunction. In this regard, the discovery process of TESS's first CBP was identical to that used for Kepler's CBPs—the orbital period of TOI-1338b was well constrained from the TESS photometry alone prior to the detailed photodynamical modeling, and the analysis of the system followed a familiar path (Welsh et al. 2015; Kostov et al. 2020a).

Most of the sky, however, is continuously covered by only a single sector of TESS observations (about 27.4 days). Compared to the orbital periods of Kepler's CBPs with a minimum of 49.5 days and median of 175 days (Martin 2018; Welsh & Orosz 2018; Socia et al. 2020), the observing duration of one TESS sector is too short to allow for the detection of more than one conjunction. Fortunately, the duration is more than sufficient to detect a CBP producing two (or more) transits during a single conjunction as these occur over a small fraction of the planet's orbital period (Kostov et al. 2020b). For the four

⁶⁵ NASA Sagan Fellow.⁶⁶ Eberly Fellow.⁶⁷ The continuous viewing zones are regions of the sky near the ecliptic poles that are covered by multiple TESS sectors.

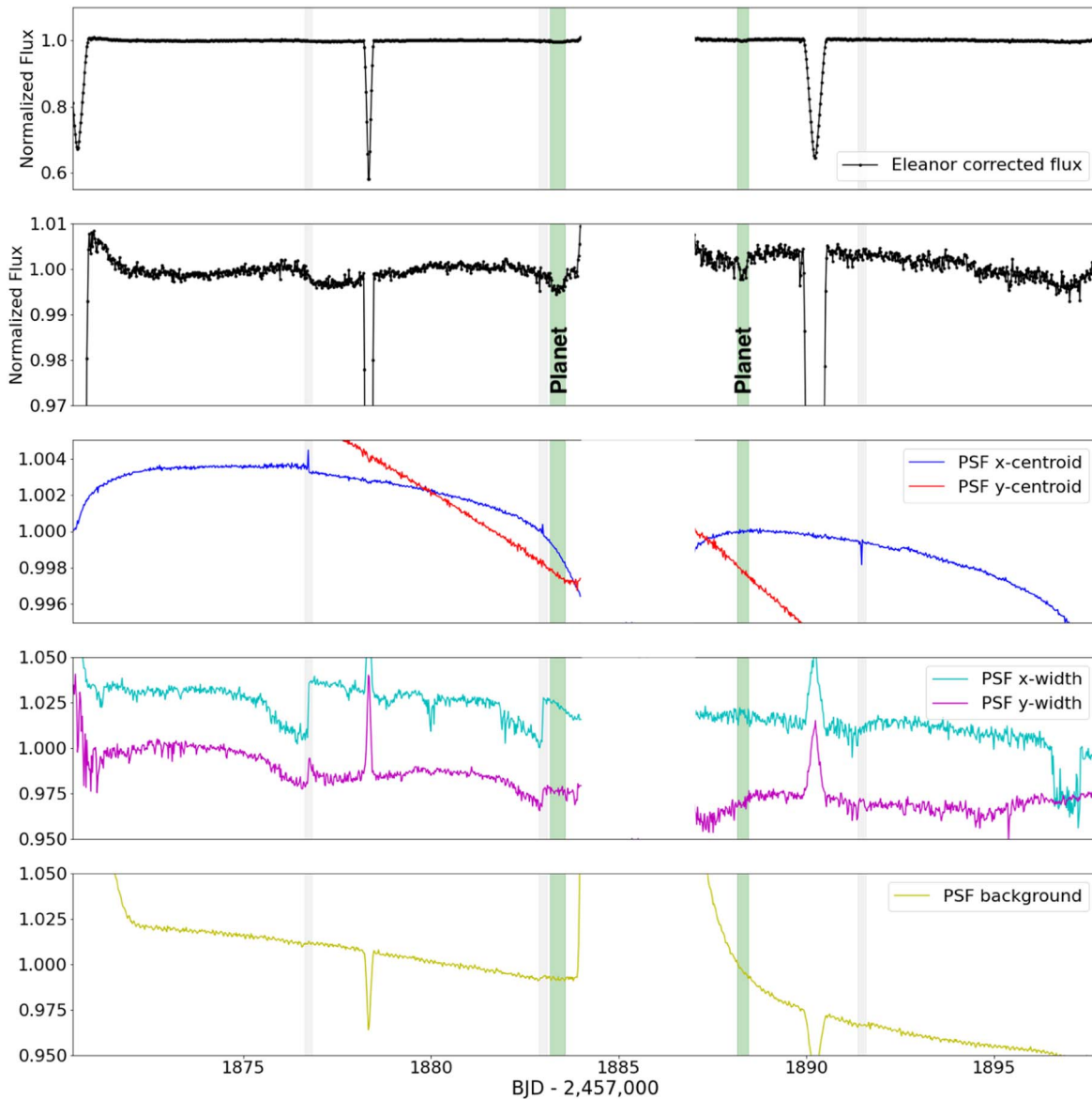


Figure 1. First panel from top: *eleanor*’s Corrected Flux light curve of TIC 1729 for Sector 21. The primary eclipse is at day 1878.3, the two secondary eclipses are at days 1870.57 and 1890.23. The CBP transits are highlighted in green. Momentum dump events are highlighted in light gray. Second panel: same as above but zoomed in to showcase the two CBP transits. Third to fifth panels: diagnostic tests to rule out photocenter shift or systematic artifacts associated with the CBP transits. Third panel: normalized x - and y -photocenters as a function of time. Fourth panel: x - and y -widths of the point-spread function (PSF) used for light-curve extraction. Fifth panel: same as above but for the background. There are no significant photocenter shifts or systematic artifacts associated with the CBP transits, confirming them as real signals.

Kepler CBPs exhibiting pairs of transits during one conjunction, the separation between these “1–2 punch” events was at most several days—well within the 27.4 days span of a TESS sector. As demonstrated by Kostov et al. (2020b), measuring the times of such transits, when supplemented with radial-velocity data for both stars in the host binary system, yields an estimate of the orbital period of the planet with an uncertainty of $\lesssim 10\%$. This is a remarkable result given that it is based on observational data covering a small fraction of the planet’s orbit. Perhaps even more importantly, finding such transits in TESS EB data is the only pathway toward detecting a significant number of transiting CBPs for years to come (Kostov et al. 2020b). These detections will enable improved population studies of a large number of these interesting worlds and provide a deeper understanding of

the formation of circumbinary planets. We note that CBPs, i.e., P-type planets (Dvorak 1986), represent a small fraction of exoplanets discovered in binary star systems. The majority of exoplanets with binary star hosts are in an S-type configuration (e.g., Haghighipour 2010; Ciardi et al. 2015; Furlan et al. 2017; Matson et al. 2018; Mugrauer & Michel 2020; Howell et al. 2021; Ziegler et al. 2021, and references therein) and a comprehensive understanding of planet formation in binary star systems depends on the analysis of both populations.

Here, we report the discovery of the first TESS CBP using the multiple transits in one conjunction technique. This paper is organized as follows. In Section 2, we describe the detection and preliminary analysis of the system in the TESS data, as well as the archival data and new observations of the system.

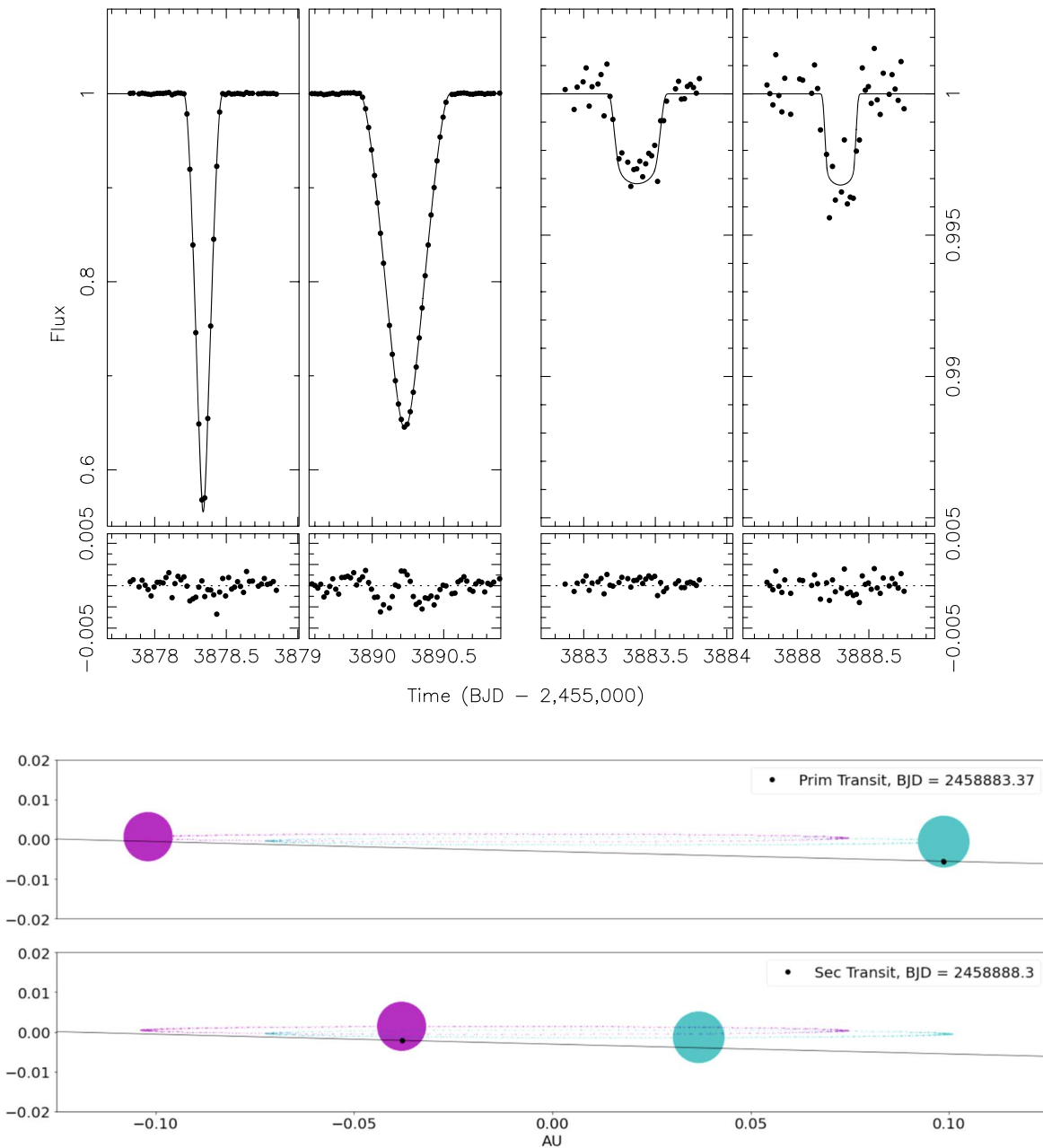


Figure 2. Upper panels, from left to right: the TESS data for the primary eclipse, the secondary eclipse, the planet transit of the primary, and the planet transit of the secondary. We note that the vertical scale on the transit panels is zoomed in by a factor of $30\times$. Also shown are the best-fitting model from Family 5 (described below), along with the residuals of the fit. Lower panels: to-scale configuration of the system at the times of the two transits. The primary star is in cyan color and the secondary is in magenta color.

Section 3 presents the comprehensive photometric-dynamical analysis of the system. We discuss the results in Section 4 and draw our conclusions in Section 5.

2. Detection

Finding transiting planets orbiting around binary stars is much more difficult than around single stars. The transits are shallower (due to the constant “third-light” dilution from the binary companion), noisier (due to starspots and stellar activity from two stars), and can be blended with the stellar eclipses.⁶⁸ This

⁶⁸ We note that the first two complications are also present when searching for transiting planets in S-type configurations.

difficulty is greatly compounded when the observations cover a single conjunction and, even if multiple transits are detected as in the system presented here, they are neither periodic, nor have the same depth and duration (e.g., Kostov et al. 2014; Windemuth et al. 2019; Martin & Fabrycky 2021). The transit times and shapes depend on the orientation and motion of the binary stars and of the CBP at the observed times. The complexity of such transits is both a curse and a blessing: it is much more difficult to find them, but once identified and confirmed as real events rather than instrumental artifacts, and shown to be originating from the same source as the eclipses, there are very few viable false-positive scenarios that can explain the morphology of the transit(s); (Kostov et al. 2020a). When combined with additional observations and modeling,

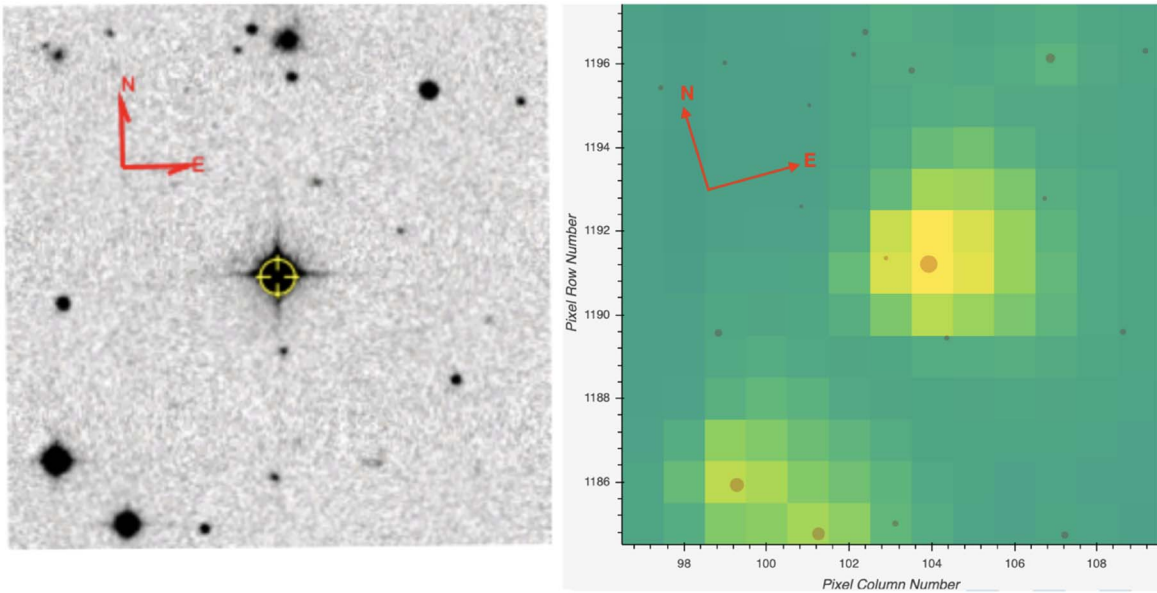


Figure 3. Left: $4/3 \times 4/3$ DSS red image of the target (highlighted with yellow cross hair). Right: $4/3 \times 4/3$ Skyview image superimposed on the TESS pixels of the target for Sector 21, showing all nearby resolved Gaia sources down to $G = 21$ mag. For clarity in matching the images, we note that the bright source due N of the target and near the upper edge of the left image is the galaxy LEDA 1954290 and is not present in the Skyview image.

the information that can be extracted from such transits is richer than what can be obtained from a single transit of a single-star planet, as these transits enable the direct estimation of the planet’s period for double-lined spectroscopic binary stars, regardless of the stellar radius or impact parameters.

As part of our TESS GI Cycle 2 and 3 programs, V. Kostov is leading a group that is performing a search for transiting CBPs using targets from the GSFC TESS EB Catalog (E. Kruse et al. 2021, in preparation). The catalog is generated by a neural network classifier and is based on the long-cadence *eleanor* light curves (Feinstein et al. 2019) we created locally from the TESS Full Frame Images (FFIs). The calibrated FFIs were produced by the Science Processing Operations Center (SPOC) and NASA Ames Research Center (Jenkins et al. 2016). The neural network, a one-dimensional adaptation of ResNet (He et al. 2015) modified for light-curve vector input, was trained to identify eclipse-like features, without any requirement for periodicity or consistency in the shape of the light curves. While this approach does allow for eclipse-shaped noise to be classified as an EB, it also provides for the identification of single-eclipse EBs. The lack of a requirement for multiple eclipses maximizes the utility of the GSFC TESS EB Catalog for a CBP search in that it allows for a greater number of candidates to be selected for further examination.

Emphasizing the need for single-eclipse detection, transit features are most readily identifiable on a light curve with a flat baseline and are found predominantly in detached binaries (in contrast to the variable baselines of semi-detached or contact binaries). Long-period detached binaries are ideal in that the flat baseline is present for a longer duration. Transit-like events are found through visual examination of the baseline from stellar systems identified in the GSFC TESS EB Catalog. While nearly all of these events have been determined through extensive vetting to be false alarms, there have been several that cannot be ruled out as false positives. TIC 172900988 exhibited two such transit-like events that are on target and proved to be caused by a \sim Jupiter-sized object on a circumbinary orbit.

2.1. TESS Data

TESS observed TIC 172900988 (hereafter TIC 1729) during Sector 21 (2020 January 21 through 2020 February 18). Preliminary inspection of the light curve revealed one primary and two secondary eclipses (the first of which is only partially covered) with depths of $\approx 40\%$ and $\approx 35\%$, respectively, and indicated an EB orbital period of ≈ 19.7 days with a significantly nonzero eccentricity. The light curve exhibits two additional transit-like events at days 1883.37 (BJD–2,457,000) and 1888.30 (just before and right after the downlink data gap), with depths of ≈ 3000 ppm (0.3%) and durations of ≈ 0.4 days and ≈ 0.27 days, respectively. Figure 1 shows the FFI *eleanor* light curve, both full scale to present the stellar eclipses and also zoomed in to highlight the CBP transits, as well as the diagnostic tests we used to rule out artifacts associated with the latter. The variations in the durations of the transits, combined with the lack of significant photocenter shift or systematic artifacts during the two events rule out false-positive scenarios due to a background EB or instrumental artifacts, and indicate a circumbinary body.

The CBP transits, the stellar eclipses in TESS data, and the configuration of the system at the transit times are shown in more detail in Figure 2. The two transits are present in all four light-curve extractions from *eleanor* (“Raw,” “Corrected,” “PCA”⁶⁹, and “PSF”⁷⁰ Flux) and are independent of the aperture used for the extraction, and the contamination from nearby sources is low ($\approx 2 \times 10^{-4}$). The closest and brightest known source inside the 13×13 target pixels, TIC 172900986, has an angular separation of $\approx 37''$ and is ≈ 8 mag fainter (see Figure 3), resulting in a maximum flux contamination of ≈ 500 ppm—much smaller than the measured transit depths. The latter, combined with the catalog stellar radius ($2.02R_{\odot}$ from the TIC, $2.1R_{\odot}$ from Gaia⁷¹), indicates that the size of the transiting body is $\approx 10R_{\oplus}$, further strengthening the CBP hypothesis. We

⁶⁹ Based on principal component analysis.

⁷⁰ Based on point-spread function analysis.

⁷¹ We note that these values do not take into account the binary nature of the target.

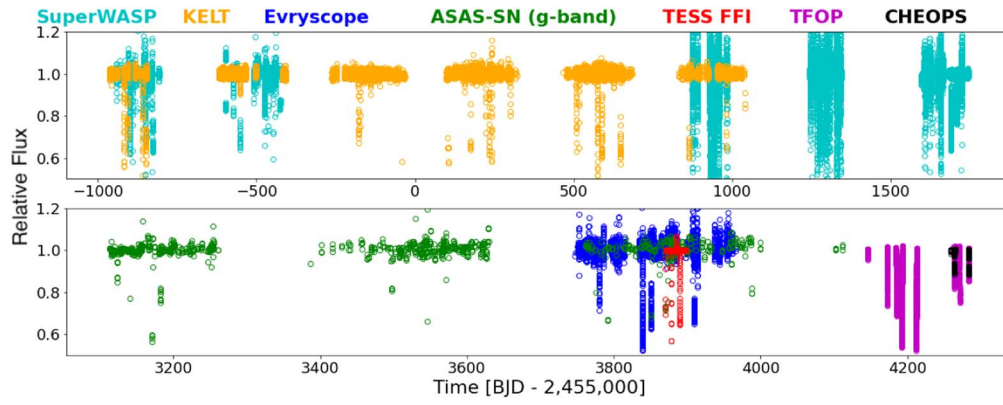


Figure 4. Archival and follow-up photometric observations of TIC 1729 highlighting the baseline covered from the available data. The colors and symbols correspond to: SuperWASP (cyan circles), KELT (orange triangles), ASAS-SN (green upside-down triangles), Evryscope (blue crosses), TESS (red squares), and TFOP (magenta crosses). The binary eclipses are in detected in all data sets.

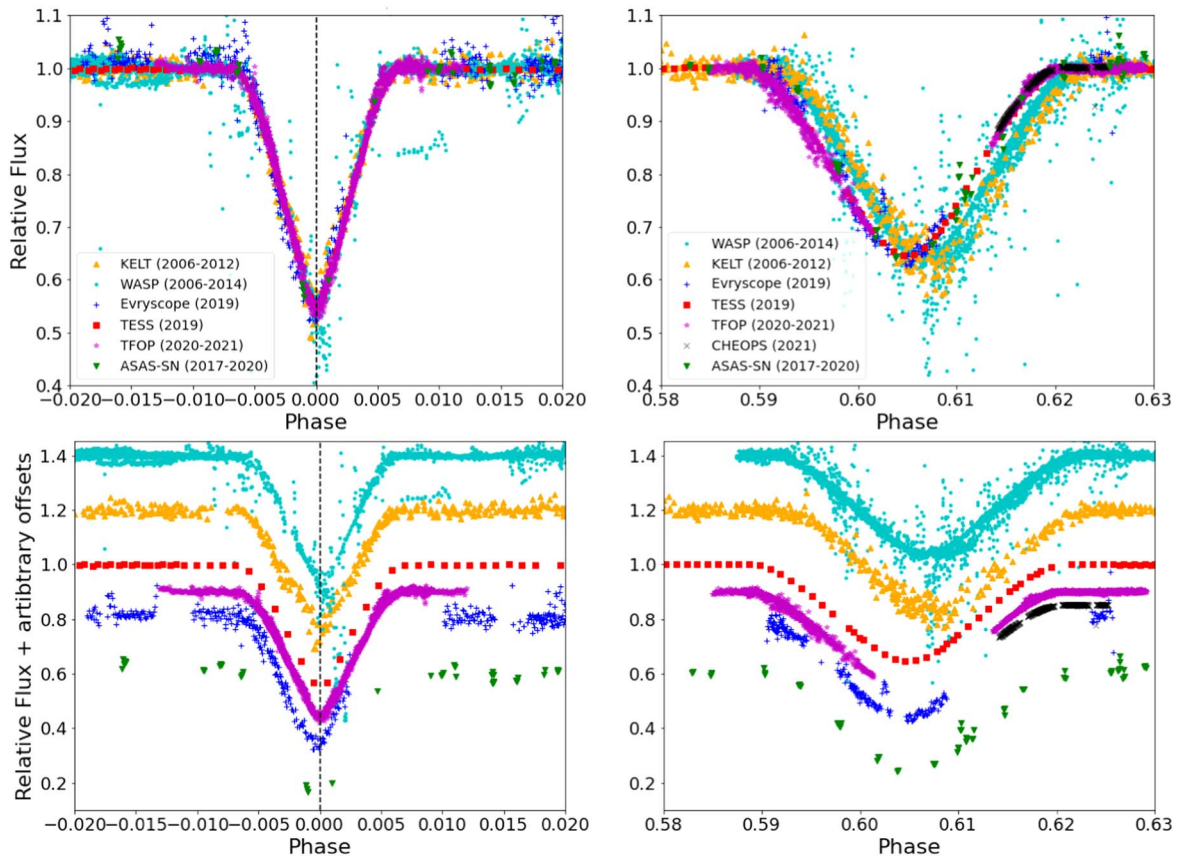


Figure 5. The photometric data shown in Figure 4 phase-folded on a linear period $P = 19.65802$ days. The left panels show the primary eclipse and the right panels show the secondary eclipse. The different data sets are vertically offset in the lower panels for clarity. The phase change of the secondary eclipse relative to the primary—indicative of the apsidal motion of the binary—is clearly seen in the right panels.

note that there is a contact binary just at the edge of the default 13×13 target pixel array for TIC 1729 (TIC 172900982, near Column 101, Row 1185 on Figure 3) but it is not a source of contamination as it is separated from TIC 1729 by almost 10 pixels and does not overlap the PSF, and the timescale of the variability ($P = 0.23$ days) is unrelated to the CBP transits.

2.2. Archival Photometry

As a relatively bright target ($V = 10.141 \pm 0.006$ mag), there is an extensive archive of photometric data on TIC 1729

from multiple sources and with long baselines. The target was observed by ASAS-SN (Shappee et al. 2014; Kochanek et al. 2017), Evryscope (Law et al. 2015; Ratzloff et al. 2019), KELT (Pepper et al. 2007), and SuperWASP (Pollacco et al. 2006), and the stellar eclipses are detected in all data sets (see Figure 4). Analysis of the archival data confirmed the orbital period of the EB estimated from TESS data and also showed a clear change in the phase of the secondary eclipse relative to the primary eclipse (see Figure 5). This phase change is indicative of apsidal precession where the argument

Table 1
Follow-up Eclipse Observations

Observatory:	Astrosberge Private Observatory	Boyce Astro Research Observatory (BARO)	Lost Gold Observatory	Terry Arnold Robotic Observatory (TARO)	RIT Observatory
Observer:	Serge Bergeron	Pat Boyce	Robert Buchheim	Scott Dixon	Michael Richmond
Location:	Casselman, Ontario, Canada	San Diego, CA	Gold Canyon, AZ	Tierra Del Sol, CA	Rochester, NY
Aperture (m):	0.305	0.431	0.400	0.400	0.300
Filter:	<i>V</i>	Sloan <i>i</i>	<i>V</i>	Sloan <i>i</i>	Bessell <i>R</i>
Exposure time (s):	45	4.6	90	3	20
Duration (hr):	2.72	2.7	3.25	2.8	3.1
CCD make/ model:	SBIG ST10XME	FLI Proline 4710 Midband	ST-8XE	Apogee U16M 18803	ATIK 11000
Calibration software:	AIJ + VPhot 4.0.6	AIJ	MPO CANOPUS / PHOTORED	AIJ	XVista
Observatory:	Northbrook Meadow Observatory	Paul and Jane Meyer Observatory (PJMO)	Stellar Skies Observatories	Mt. Laguna Observatory	
Location:	Northbrook, IL	Waco, TX	Pontotoc, TX	Mt. Laguna, CA	
Observer:	Joe Ulowetz	Bradley Walter	Edward Wiley	Mitchell Yenawine	
Aperture(m):	0.235	0.610	0.280	1.00	
Filter:	<i>V</i>	<i>R</i>	<i>B</i>	<i>V</i>	
Exposure time (s):	45	10	60	3	
Duration (hr):	2.35	3.7	3	4.2	
CCD make/ model:	QSI-583w	Princeton Instruments PIXIS 3048B eXcelon	Moravian G1600	e2v CCD42-40	
Calibration software:	CCDStack2 + MaxIm DL5	AIJ	AIJ	AIJ	

of periastron of the binary changes with time, and constrains the mass of the CBP.

SuperWASP-North was an array of eight cameras located at the Roque de los Muchachos Observatory on La Palma. Each 200 mm/f1.8 lens was backed by $2k \times 2k$ CCDs operating with a wide-band, 400–700 nm filter (Pollacco et al. 2006). TIC 172900988 was observed in 2006 July, accumulating 6000 photometric data points, then again in 2008, obtaining another 2000 points, and again from 2011 December to 2014, accumulating 12,000 more data points. TIC 172900988 is the only bright star in the $48''$ extraction aperture.

The Kilodegree Extremely Little Telescope (KELT, Pepper et al. 2007, 2012) is a ground-based, small-aperture, wide-field photometric survey searching for transiting exoplanets, using a nonstandard passband equivalent to a broad $V + R + I$ filter. It has a pixel scale of $23'' \text{ pixel}^{-1}$, and the photometric reduction procedures are described in Siverd et al. (2012). The KELT-North telescope at Winer Observatory in Arizona observed TIC 1729 from 2006 October 27 to 2012 April 22, obtaining 8059 observations.

We used g' -band observations from Evryscope-North, located at Mount Laguna Observatory, approximately 44 miles (70 km) southeast of Palomar Observatory in southern California. The Evryscope pair of robotic all-sky telescopes, sited in Chile and California, are arrays of 6 cm telescopes designed to cover the entire accessible sky from each observing site in every exposure. Together, the Evryscopes survey an instantaneous field of view (FOV) of 16,512 square degrees at 2 minutes cadence with $13.2''$ resolution. The Evryscope system design and survey strategy are described in Law et al. (2015) and Ratzloff et al. (2019). The data were filtered to exclude observations with signal-to-noise ratios less than 40. A total of 93 points were rejected (1.56% of the observations). Eight additional points near HJD 2458909.84 were identified as outliers and omitted; unfortunately

these were during a secondary eclipse. A total of 5656 points remained, and the HJD dates were converted to BJD_{TBD} using Jason Eastman's website tool⁷² (Eastman et al. 2010). The pipeline magnitudes were converted to normalized fluxes by dividing by the out-of-eclipse median, and the uncertainties in fluxes were obtained from the geometric mean of the upper and lower uncertainties in magnitudes. The error bars were then scaled by a factor of 2.53 so that the uncertainties matched the rms scatter in the out-of-eclipse portions of the light curve.

2.3. Follow-up Observations

2.3.1. Photometry

With the archival data supporting our hypothesis that TIC 1729 was a CBP candidate based on the clear apsidal motion, we quickly turned our attention to obtaining follow-up observations. We contacted Dr. Dennis Conti of the American Association of Variable Star Observers (AAVSO) who was able to rally the AAVSO observers on 2020 May 6 for observations later that night (May 7 UT; AAVSO Alert Notice 704). We obtained eight independent light curves from AAVSO members, plus an additional light curve from Mount Laguna Observatory. The observers were located across most of the North American continent and thus, despite the target setting early in the evening, we were able to record much of the eclipse. The observations were obtained in the $BVRi$ bandpasses and these data are discussed in Section 3.1. The details of the photometric observations are given in Table 1.

We also acquired ground-based time-series follow-up photometry of TIC 172900988 as part of the TESS Follow-up Observing Program (TFOP).⁷³ We used the TESS Transit Finder, which is a customized version of the Tapir software package

⁷² <http://astroutils.astronomy.ohio-state.edu/time/utc2bjd.html>

⁷³ <https://tess.mit.edu/followup>

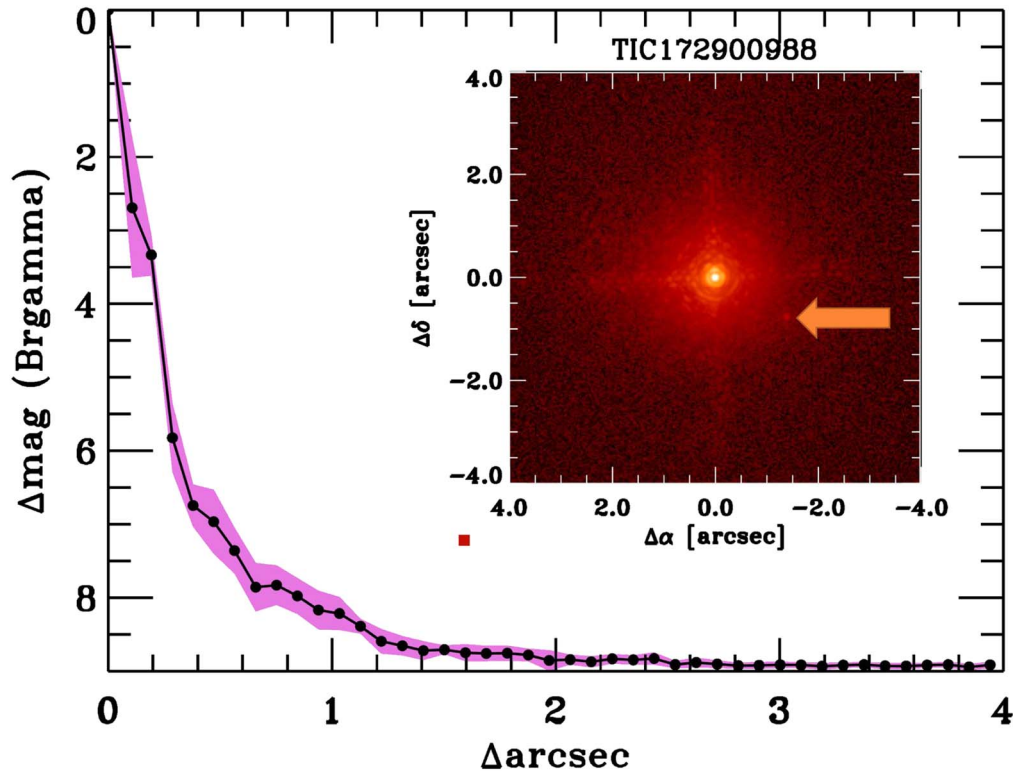


Figure 6. Companion sensitivity for the Palomar adaptive optics imaging. The black points represent the 5σ limits and are separated in steps of 1 FWHM ($\sim 0''.097$); the purple represents the azimuthal dispersion (1σ) of the contrast determinations (see text). The inset image is of the primary target. The detected companion is marked with an arrow and there are no additional companions to within $3''$ of the target. The location of the detected companion in the contrast plot (Δmag vs. Δarcsec) is shown by the red square, such that the size of the square is approximately equal to the uncertainty on the magnitude and separation.

Table 2
TESS Follow-up Observing Program Observations

Observatory/Location	Date (UTC)	Filter	Exposure (s)	Total (hr)	Aperture (m)	Pixel Scale (arcsec)	FOV (arcmin)
<i>Primary Observations</i>							
LCOGT, Haleakala, Hawaii	2020 Nov 19	<i>z</i> s	75	4.9	0.4	0.57	29.2×19.5
LCOGT, Haleakala, Hawaii	2020 Dec 9	<i>z</i> s	75	5.1	0.4	0.57	29.2×19.5
Brigham Young Univ. Obs.	2020 Dec 9	<i>R</i>	30	6.8	0.2	1.42	25.7×17.4
LCOGT, Teide Observatory, Canary Islands	2020 Dec 28	<i>z</i> s	75	7.5	0.4	0.57	29.2×19.5
Observatori Astronòmic Albanya, Spain	2020 Dec 28	<i>I</i> c	120	5.6	0.4	1.44	36.0×36.0
<i>Secondary Observations</i>							
LCOGT, Haleakala, Hawaii	2020 Oct 23	<i>z</i> s	75	3.2	0.4	0.57	29.2×19.5
LCOGT, CTIO, Chile	2020 Dec 1	<i>z</i> s	18	2.5	1.0	0.39	26.5×26.5
LCOGT, McDonald Observatory, Texas	2020 Dec 1	<i>z</i> s	18	6.4	1.0	0.39	26.5×26.5

(Jensen 2013), to schedule our transit observations. The photometric data were extracted using *AstroImageJ* (Collins et al. 2017). Observations were acquired using the Las Cumbres Observatory Global Telescope (LCOGT; Brown et al. 2013) network, Brigham Young Observatory, and Observatori Astronòmic Albanya as described in Table 2.

As discussed below, our photodynamical model produced several solutions with nearly equal likelihood but a CBP orbital period that differs by a few days (other system parameters are mostly the same). Naturally, these solutions produced distinct predictions for the 2021 February conjunction of the CBP, separated by about a week and mutually exclusive. Catching these predicted transits from the ground is challenging due to their shallow depth, relatively wide window, and the usual diurnal and weather issues. Thus we pursued follow-up observations of the predicted transits with CHEOPS (Benz et al. 2021) through DDT

program #004. The combination of precision photometry, instrument stability, duty cycle, and response time makes CHEOPS well suited for these observations. The target was observed over the course of five visits, each about 5 hr long and partially covering an expected transit corresponding to four of the solutions mentioned above (see Figure 4). The observations were processed with the CHEOPS data reduction pipeline (Hoyer et al. 2020), and their analysis is presented in Section 3.

2.3.2. High Angular Resolution Imaging

As part of our standard process for validating transiting exoplanets to assess the effect of any contamination by bound or unbound companions on the derived planetary radii (Ciardi et al. 2015), we observed TIC 1729 with infrared high-resolution adaptive optics (AO) imaging at Palomar Observatory. The

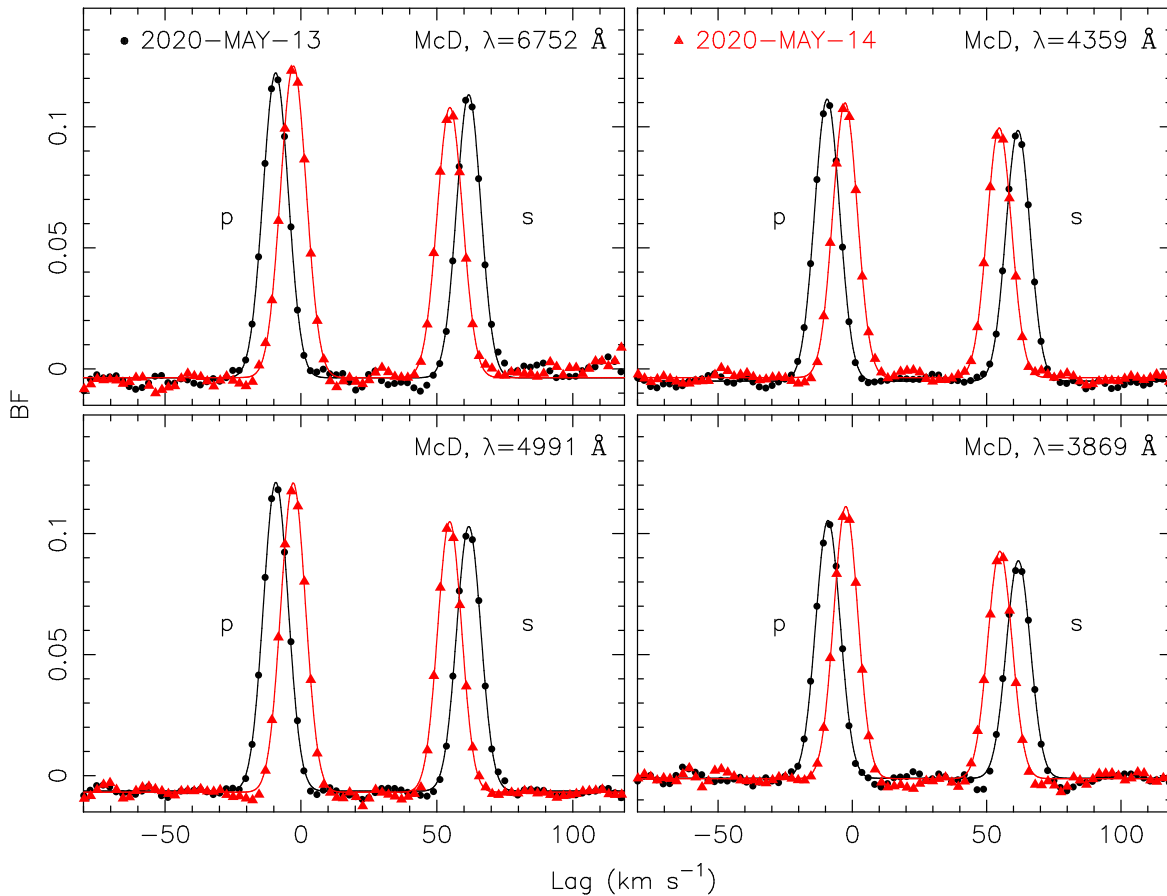


Figure 7. Broadening Functions (BFs) derived from the McDonald spectra are shown for four echelle orders (the central wavelengths are indicated in each panel). The BFs themselves are shown with the symbols, and the solid lines show the best-fitting double Gaussian functions. The peaks from the two components are clearly resolved and marked with a “p” for the peak due to the primary star and an “s” for the peak due to the secondary star. The Doppler shift between the first spectrum from the night of 2020 May 13 (filled circles) and the spectrum from May 14 (filled triangles) is evident. No other peaks from additional stars are evident.

Palomar Observatory observations were made with the PHARO instrument (Hayward et al. 2001) behind the natural guide star AO system P3K (Dekany et al. 2013) on 2021 February 24 UT in a standard five-point quincunx dither pattern with steps of $5''$. Each dither position was observed three times, offset in position from each other by $0''.5$ for a total of 15 frames.

The camera was in the narrow-angle mode with a full field of view of $\sim 25''$ and a pixel scale of approximately $0''.025$ per pixel. Observations were made in the narrowband Br γ filter ($\lambda_o = 2.1686$; $\Delta\lambda = 0.0326 \mu\text{m}$) with an integration time of 5.6 s per frame (118 s total).

The AO data were processed and analyzed with a custom set of IDL tools. The science frames were flat-fielded and sky-subtracted. The flat fields were generated from a median average of dark-subtracted flats taken on sky. The flats were normalized such that the median value of the flats is unity. The sky frames were generated from the median average of the 15 dithered science frames; each science image was then sky-subtracted and flat-fielded. The reduced science frames were combined into a single combined image using an intrapixel interpolation that conserves flux, shifts the individual dithered frames by the appropriate fractional pixels, and median-coadds the frames. The final resolution of the combined dither was determined from the FWHM of the point-spread function to be $0''.097$ (Figure 6).

The sensitivities of the final combined AO image were determined by injecting simulated sources azimuthally around

the primary target every 20° at separations of integer multiples of the central source’s FWHM (Furlan et al. 2017). The brightness of each injected source was scaled until standard aperture photometry detected it with 5σ significance. The resulting brightness of the injected sources relative to the target set the contrast limits at that injection location. The final 5σ limit at each separation was determined from the average of all of the determined limits at that separation and the uncertainty on the limit was set by the rms dispersion of the azimuthal slices at a given radial distance (Figure 6).

A single faint companion was detected $1''.59 \pm 0''.01$ to the southwest at a position angle of $237^\circ \pm 1^\circ$. The companion star is $\Delta K_s = 7.22 \pm 0.07$ mag fainter than the primary star, yielding an apparent magnitude of $K_2 = 16.0 \pm 0.1$ mag. Because the companion was only detected in the final reduced data, observations in a second filter were not obtained for a determination of the color temperature of the star. Further, the companion star is not detected in Gaia DR3. As such, we are unable to determine if the companion is bound to TIC 172900988 or if it is a background/foreground star. Based upon the analysis of the inner binary star, the two stars are late-F and early-G main-sequence stars (see Section 4.1 below). Thus if the detected companion is bound, it has a relative K -band brightness consistent with the star being a late-M dwarf ($\sim M8V$). If it is indeed an M8V, the TESS magnitude to infrared color should be $Tmag - Kmag \approx 3.5$ mag, making the real apparent TESS magnitude 10.5 mag fainter than the combined brightness of the primary stars

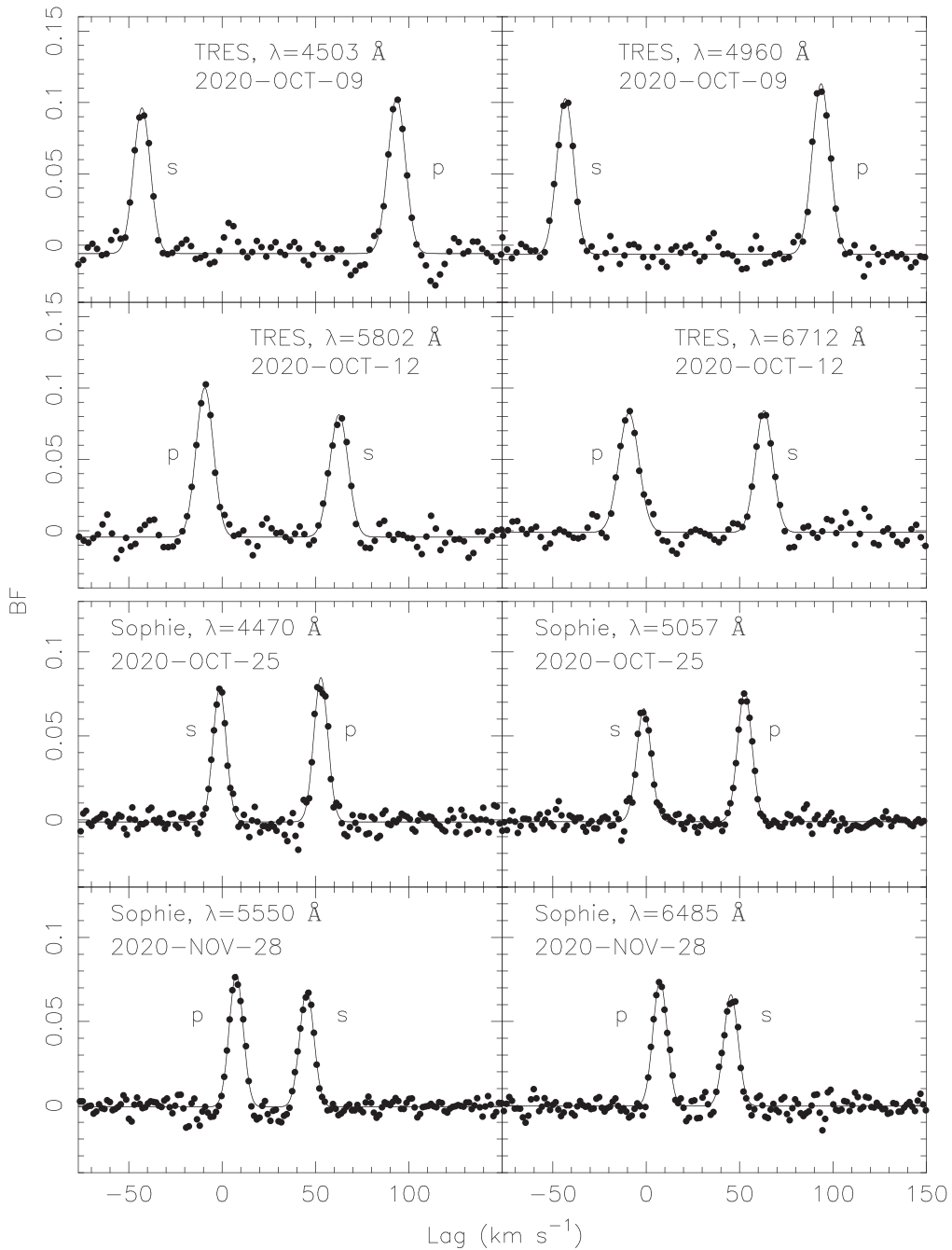


Figure 8. Similar to Figure 7, but for the TRES spectra (top 4 panels) and the Sophie spectra (bottom 4 panels).

—far too faint to be responsible for the observed planetary transits of ≈ 3000 ppm. If the companion star is bound to the binary and the distance of the system is ≈ 240 pc (Gaia DR3 and see below), the M8V star ($M \approx 0.08M_{\odot}$) has a projected separation of 380 au, which would correspond to an orbital period of ≈ 5000 yr. If the companion star is not bound and has a typical color $T_{\text{mag}} - K_{\text{mag}} \approx 2$ mag, it is still too faint to be responsible for the observed transits.

2.3.3. Spectroscopy

We obtained four spectra of TIC 1729 using the Tull Coudé spectrograph (Tull et al. 1995) on the Harlan J. Smith 2.7 m telescope (HJST) at McDonald Observatory in West Texas.

Three spectra with net exposure times of 1200 s each were obtained 2020 May 13 and one additional spectrum with an exposure time of 1200 s was obtained 2020 May 14. The total wavelength coverage was 3760–10000 Å with a resolving power of $R = 60,000$. An iodine (I_2) cell was used, and I_2 absorption lines are superimposed on the stellar absorption lines between about 4992 Å and 6200 Å. The spectra were reduced using custom scripts based on standard IRAF⁷⁴ routines. The reduced

⁷⁴ IRAF is distributed by the National Optical Astronomy Observatories, which are operated by the Association of Universities for Research in Astronomy, Inc., under cooperative agreement with the National Science Foundation.

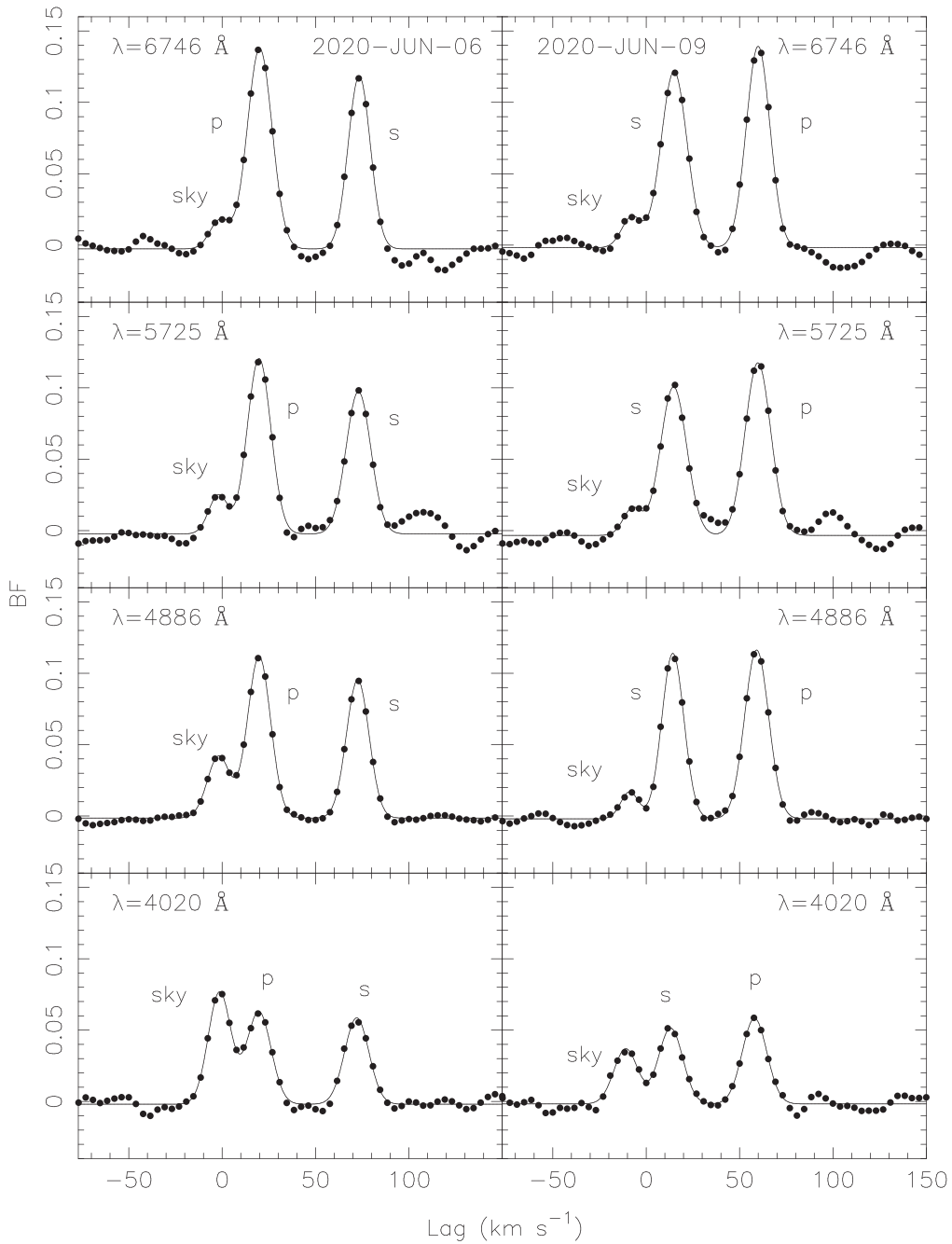


Figure 9. Similar to Figure 7, but for the ARCES spectra. In this case, an extra peak in the BFs due to sky contamination is seen near zero velocity. The strength of that peak depends on the wavelength as it generally gets stronger for the bluer orders. For these BFs, a triple Gaussian model was used to find the velocities of each peak.

spectra have signal-to-noise ratios of between about 80 at 4400 Å to 120 per pixel at 6500 Å.

Four spectra of TIC 1729 were obtained using the Tillinghast Reflector Echelle Spectrograph (TRES, Szentgyorgyi & Furész 2007; Buchave et al. 2010) on the 1.5m telescope at the Fred L. Whipple Observatory in southern Arizona in October and December of 2020. These spectra cover a wavelength range from about 3850 to 9100 Å with a resolving power of $R \approx 44,000$, and have signal-to-noise ratios of 30 to 35 per resolution element of 6.8 km s^{-1} near 5200 Å. The spectra were reduced using the standard TRES data reduction pipeline described by Buchave et al. (2010).

We obtained spectra of TIC 1729 on 2020 June 3 and 9 (one spectrum from each night) using the ARC Echelle Spectrograph (ARCES; Wang et al. 2003) on the Astrophysical Research Consortium 3.5 m telescope at Apache Point Observatory (APO) in New Mexico. ARCES has a resolving power of $R \approx 32,500$ and a wide spectral coverage of 3200–10000 Å. Each night we obtained three 5 minutes exposures just after sunset at relatively high airmass (≈ 2.5 –3). Quartz lamps were taken at the beginning of each half night, and thorium-argon lamps were taken at the beginning and end of each half night to perform wavelength calibration. The images were bias- and dark-subtracted using the Python

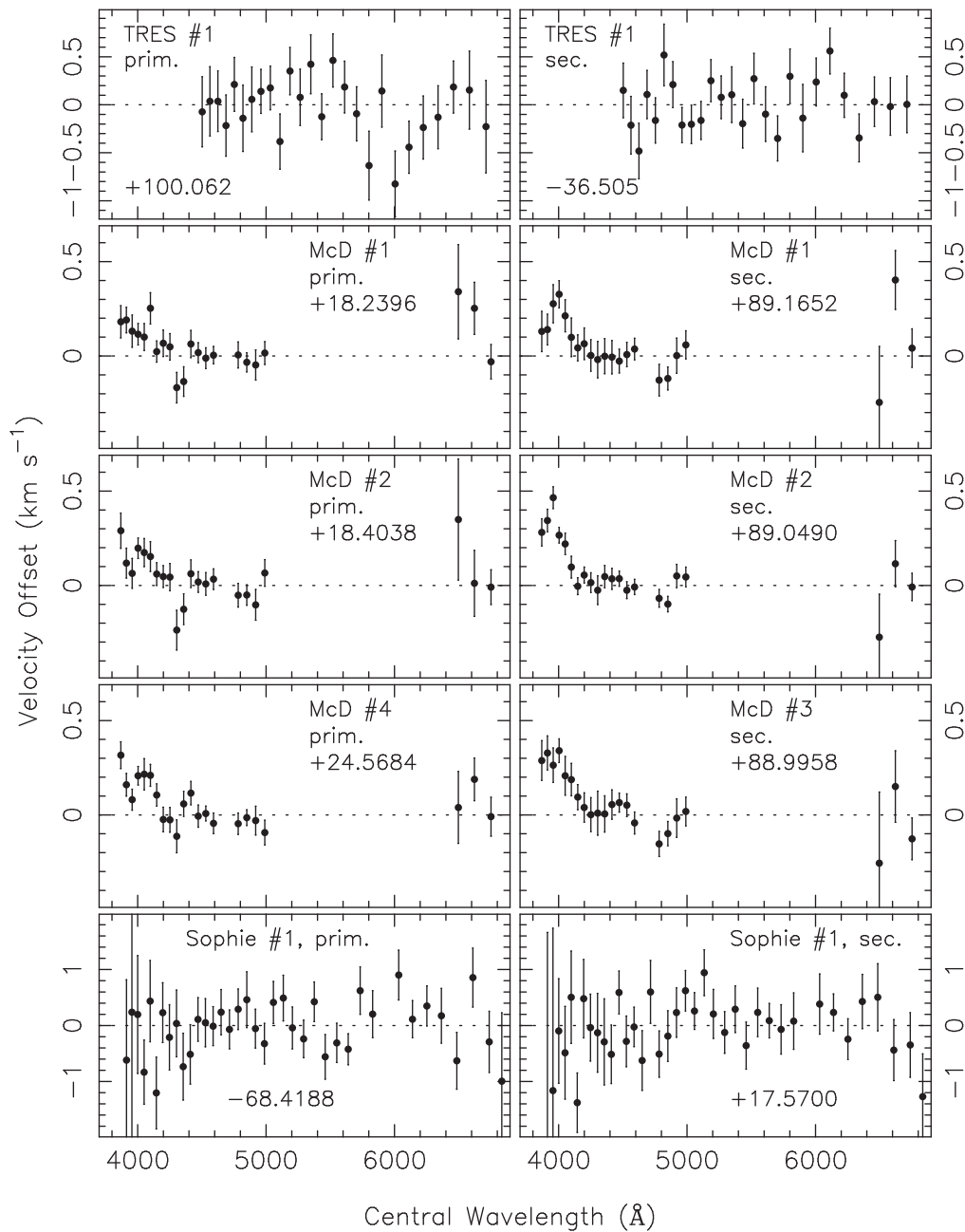


Figure 10. The radial velocities found from each echelle order as a function of the central wavelength, relative to the final adopted value for the first TRES spectrum (top panels), three of the McDonald spectra (middle panels), and the first Sophie spectrum (bottom panels). The velocities for the primary are on the left and the velocities for the secondary are on the right.

package `ccdproc` (Craig et al. 2017). The spectral extraction, initial wavelength calibration, and normalization were performed using custom Python routines. The initial wavelength solution was performed by fitting a fourth-order polynomial individually for each order and then refined with a two-dimensional dispersion solution using the `echelle` package of the IRAF software.

Finally, eight spectra of the target were also obtained on the high-resolution spectrograph SOPHIE (Perruchot et al. 2008), which is mounted on the 193 cm telescope at Observatoire de Haute Provence (OHP), in France, and was designed and constructed to detect exoplanets (e.g., Bouchy et al. 2009). The instrument has a long-term stability of 2 m s^{-1} . The spectra were all taken with an exposure time of 900 s between 2020

November 15 and December 6 to cover several phases of the binary period.

There are no indications of additional stars in any of the obtained spectra. To extract the radial velocities of each star from the spectra we used the “broadening function” (BF) technique (Rucinski 1992, 2002). A high signal-to-noise ratio spectrum of a slowly rotating star is needed as a template for the BF analysis. For the McDonald spectra, high signal-to-noise ratio spectra (≈ 1000 per pixel) of diffused daytime sky near the zenith are routinely obtained, and we used one such spectrum obtained on 2020 May 12 as the template. This spectrum was obtained with the “Solar Port,” which is a ground quartz diffuser on the roof of the coudé slit room. This sends the light falling on it into the spectrograph. That light is a combination of direct sunlight (the

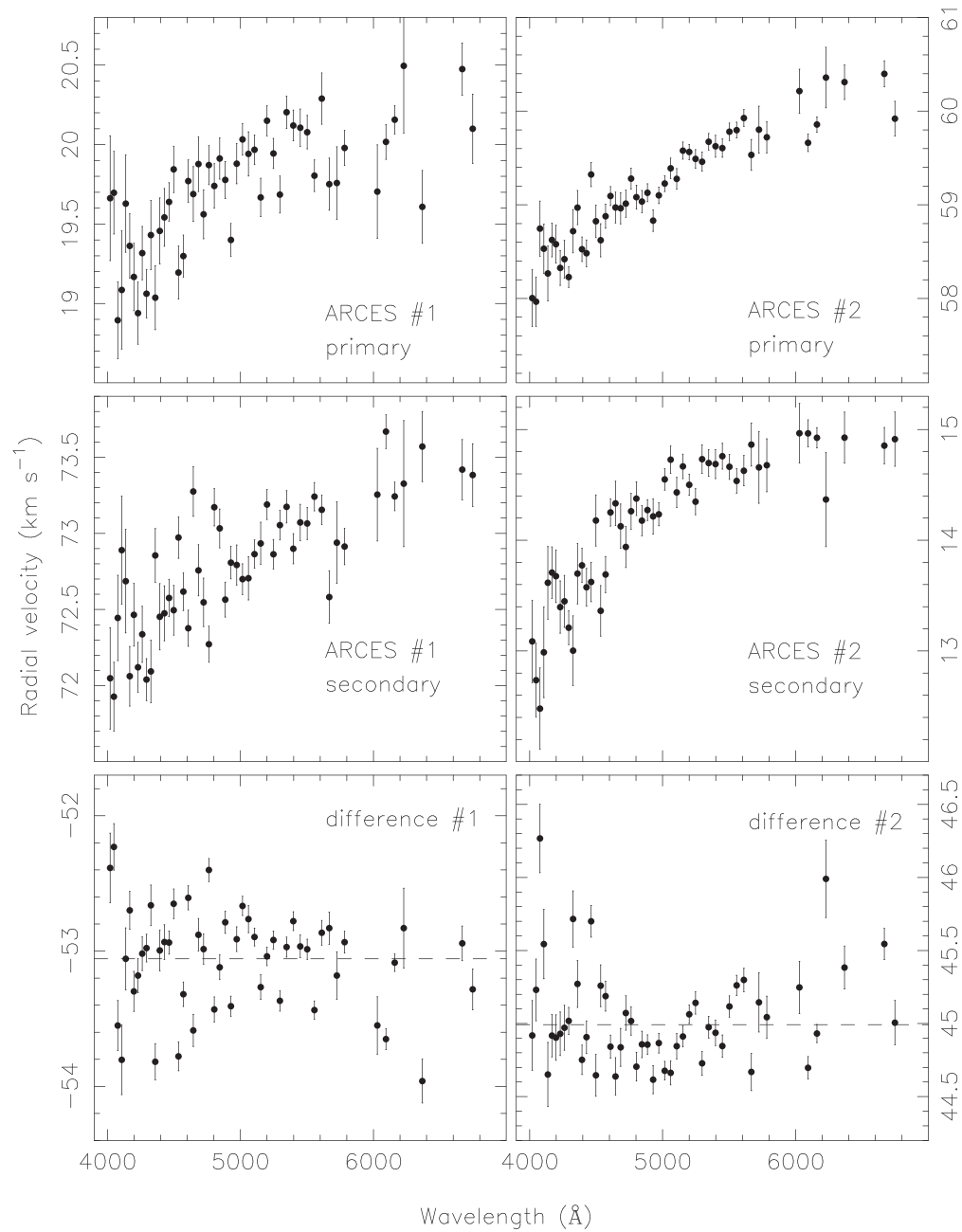


Figure 11. The radial velocities found from each echelle order as a function of the central wavelength for the 2020 June 3 ARCES spectrum (left panels) and the 2020 June 9 ARCES spectrum (right panels). There are clear trends in both the primary and secondary velocities with wavelength (top two panels). By contrast, there is no apparent trend in the difference between the primary and secondary velocity with wavelength (bottom panels). The dashed lines show the respective weighted averages of the differences.

dominant component) and general daytime skylight. A spectrum of HD 182488 taken 2018 May 31 was used as the template for the TRES spectrum. A spectrum of HD 185144 taken 2021 June 13 was used as the template for the Sophie spectra. Finally, a spectrum of the twilight sky was used as the template for the ARCES spectra. The BFs were extracted separately for each order (in preparation for this analysis, the spectra were normalized to their local continua using spline fitting as implemented in IRAF). Representative BFs are shown for each instrument in Figures 7–9. With the exception of two Sophie observations (those from 2020 October 31 and November 11), the BF peaks from the primary and secondary stars are cleanly resolved, and no

other peaks from additional stars (either bound to the system or along the line of sight) are evident. The BFs from the ARCES spectra (Figure 9) show a third component near zero velocity from night sky background.

To obtain the final velocities for each spectrum, the following procedures were used. For the TRES spectra, we used 26 orders covering roughly 4500–6700 Å. The BFs were fitted with a double Gaussian model to find the velocity shifts and widths. There were no apparent trends with central wavelength (Figure 10). A horizontal line was fitted to the velocities and the error bars on the individual measurements were scaled to give $\chi^2_{\min} = N_{\text{dof}}$ for this fit. After the errors were scaled, a weighted average was

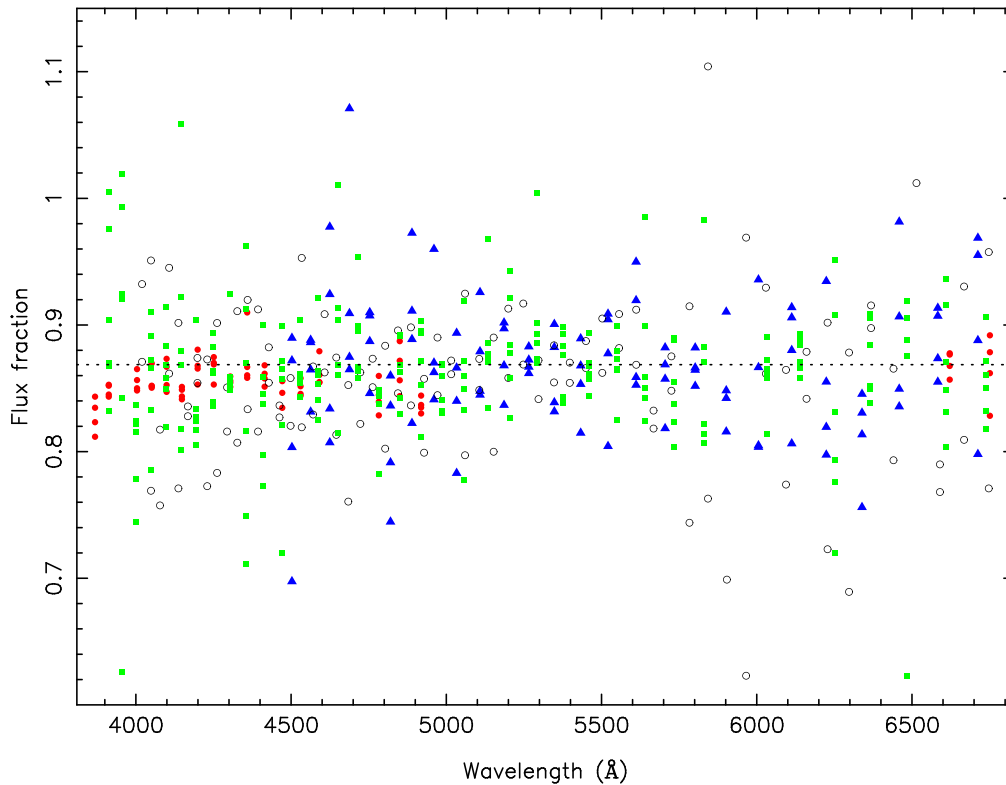


Figure 12. The flux fractions (the secondary flux divided by the primary flux) as a function of wavelength for the McDonald spectra (red filled circles), the TRES spectra (blue filled triangles), the Sophie spectra (filled green squares) and the ARCES spectra (black open circles). The two stars have similar spectral energy distributions as there are no trends with wavelength. The dotted horizontal line is the adopted flux fraction of 0.8669 for all bandpasses used in the photodynamical analysis.

computed to get the velocity for the primary and the velocity for the secondary (Table 4). A similar procedure was used for the Sophie spectra, where we used 39 orders covering roughly 3950–6830 Å. The adopted radial velocities for the six double-lined spectra are reported in Table 4.

For the McDonald spectra, we used 22 orders covering roughly 3900–6700 Å. Orders 42 and 43 were skipped owing to a “picket fence” artifact caused by internal reflections, and orders 23–37 were skipped owing to the iodine lines (while the pipeline for extracting precise radial velocities for single-lined spectra taken with the I_2 cell is well developed, a similar pipeline for double-lined spectra is not quite perfected). The BFs were fitted with double Gaussian models to find the velocity shifts and widths. There was an odd trend with wavelength in that the six bluest orders had velocities that were shifted to slightly larger values (Figure 10). This systematic shift seemed to be stronger in velocities for the secondary. Given this systematic shift, we skipped the first six bluest orders when computing the final velocities. As before, a horizontal line was fitted to the remaining velocities, and the individual error bars were scaled to give $\chi^2_{\min} = N_{\text{dof}}$. After the errors were scaled, a weighted average was computed to get the velocity for the primary and the velocity for the secondary (Table 4).

The ARCES spectra were the most challenging to extract radial velocities from. There were 51 orders used, covering from about 4000 Å to about 6700 Å (a few of the orders with strong telluric absorption lines were skipped). After the BFs were found, it was apparent that there was residual sky contamination, and that the sky contamination was stronger in the bluer orders. Given the extra peak, a triple Gaussian model was used to fit the BFs (Figure 9). There was a clear and strong

trend seen in the velocities from individual orders (Figure 11). Although the wavelengths of the sky peaks seemed to be roughly constant with the echelle order, the velocities for both the primary and the secondary showed an almost linear trend with the central wavelength of the echelle order. This trend was most likely a result of atmospheric refraction at high airmass as the slit width ($1''.6$) was larger than the seeing-limited image of the star ($\approx 1''$) on the given nights, resulting in a chromatic shift in the stellar line-spread function not seen in the residual sky spectrum that evenly filled the slit. The velocities at the reddest orders were nearly 2 km s^{-1} larger than the velocities at the bluest orders. However, the velocity difference between the two peaks stayed reasonably constant over wavelength. Thus, for each night, we measured the separation between the two peaks in a manner similar to what was done for the TRES spectra and used the velocity differences in the photodynamical fitting described below.

The flux fraction, which we define as the secondary flux divided by the primary flux, is a useful constraint on the photodynamical model. The BFs in each echelle order were modeled either with a double Gaussian model (McDonald, Sophie, and TRES) or a triple Gaussian model (ARCES), and the ratio of the areas under each peak was taken to be the flux fraction for that echelle order. Figure 12 shows the individual flux fractions as a function of the central wavelengths. The two stars are pretty similar, and there are no apparent trends in the flux fractions over these wavelengths (≈ 3900 to ≈ 6800 Å). The average flux fractions are 0.8687 ± 0.0052 for TRES, 0.8555 ± 0.0018 for the McDonald spectra, 0.8632 ± 0.0043 for Sophie, and 0.8544 ± 0.0079 for ARCES. To adopt a flux fraction for the photodynamical model, we combined the flux

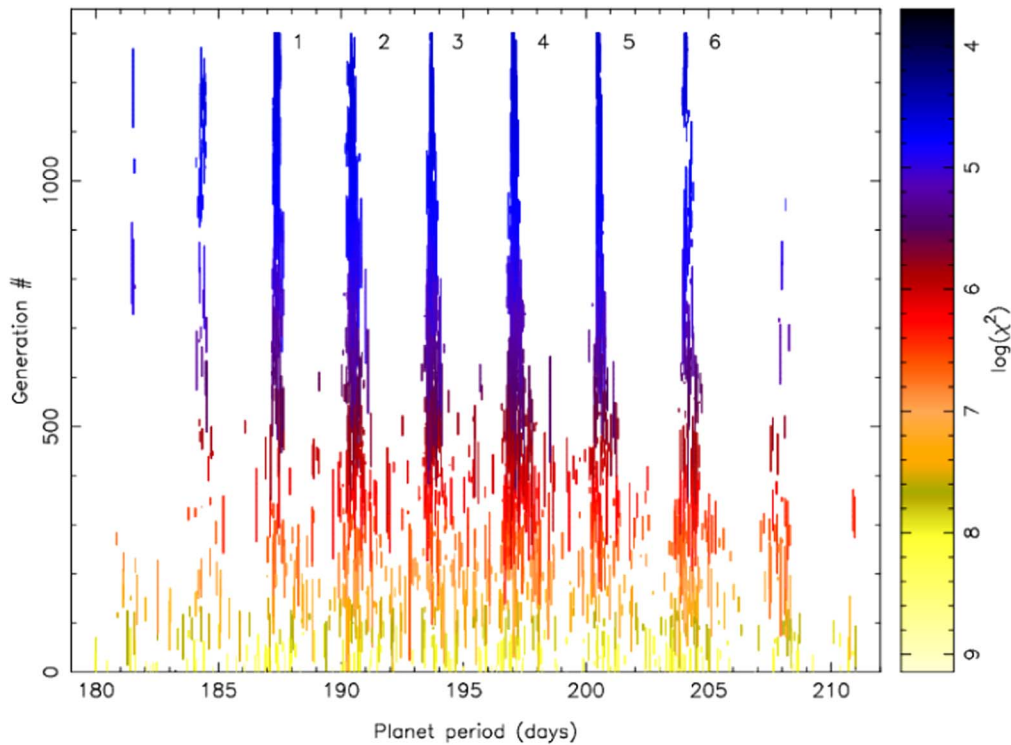


Figure 13. Nested sampling photodynamical solutions showing the evolution of the live points as a function of the CBP period. The colors of the points give the χ^2 values of the points, as indicated in the color bar. Points with lighter colors have relatively large values of χ^2 , and points with the darker colors have relatively small values of χ^2 . As better solutions are found by the algorithm, the live points evolve to regions of higher likelihood. For the CBP period, there are six families (“fingers”) that remain populated and have comparable likelihood. The number next to the right of each finger indicates the family number shown in Tables 5 and 6. The fingers with periods near ≈ 181 , 184, 208, and 211 days have many fewer live points in them, and the live points that remain there have lower likelihoods than the live points in the fingers labeled 1 through 6. For these reasons these outlying fingers were not considered further. Note that this is a representative figure based on the 2020 data; the “fingers” persist after the inclusion of the 2021 data but recreating this figure with all available data proved to be computationally prohibitive. The best-fit planet periods shift by about a day between the numbers in the figure and those listed in Tables 5 and 6. See text for details.

fractions from the TRES and Sophie instruments and computed a weighted average of 0.8669 ± 0.0037 . The McDonald flux fractions were excluded since the iodine-free echelle orders have very little overlap with the filters used for the photometry (the B band with a peak near $\approx 4650 \text{ \AA}$ and filters redward of this). The ARCES flux fractions were excluded owing the contamination from night sky lines. Since the stars are very similar, we adopted a flux fraction of 0.8669 ± 0.0037 for all bandpasses in the photodynamical analysis described below.

3. Photodynamical Analysis of the Light and Velocity Curves

We used the Eclipsing Light Curve (ELC) code of Orosz & Hauschildt (2000) to model the light and radial-velocity curves of TIC 1729 (see Orosz et al. 2019, for a recent discussion of the modifications relevant for the analysis of circumbinary systems). We performed a full photodynamical analysis in which the sky positions of the various bodies as a function of time are found by using a numerical integrator to solve the Newtonian equations of motion. The equations of motion have extra terms to account for precession due to General Relativity, for precession due to tidal bulges on each star (Eggleton et al. 1998; Mardling & Lin 2002), and light-travel time across the orbits. The numerical integrator that ELC uses is a symplectic, twelfth-order Gaussian Runge–Kutta (GRK12) routine based on methods and codes devised by Hairer et al. (2006). For TIC 1729, the step size for the GRK12 routine was 0.05 day. After the integrator is run, we have the sky positions of each

body as a function of time. Then, given the sky positions and information about the radiative properties of the components, the observed light curves can be computed using the algorithm discussed in Short et al. (2018), assuming spherical bodies with quadratic limb-darkening laws.

3.1. Observational Data through 2020

We have light curves in eight distinct bandpasses: the TESS bandpass, B , V , R , Sloan i (see Table 1), Sloan g (ASAS-SN and Evryscope), KELT, and WASP. A secondary eclipse was partially covered at the start of the TESS observations, and these data were not used in the fitting owing to difficulties with normalizing the light curve. We only want to fit photometric data near an eclipse or a transit event, and the selection of observations near these events from the archival data requires a good ephemeris. Fortunately it was not difficult to find a suitable ephemeris ($P = 19.658025$, $T_0 = 3878.33860$, where the time convention is BJD $-2,455,000$) using the TESS data, the RV data, and some of the early WASP data where partially covered primary eclipses are seen. Using this ephemeris, we selected data with phases within 0.02 of phase zero (e.g., the primary eclipse) and also with phases between 0.575 and 0.645 (e.g., the secondary eclipse) from the KELT, WASP, and Evryscope data sets. All of the photometric data were converted to flux units as necessary, and then normalized to have an out-of-eclipse flux of 1.0. In an effort to facilitate the fitting, we also fit for the measured times of the primary eclipse, the secondary eclipse, and the two transits in the TESS data. Experience has

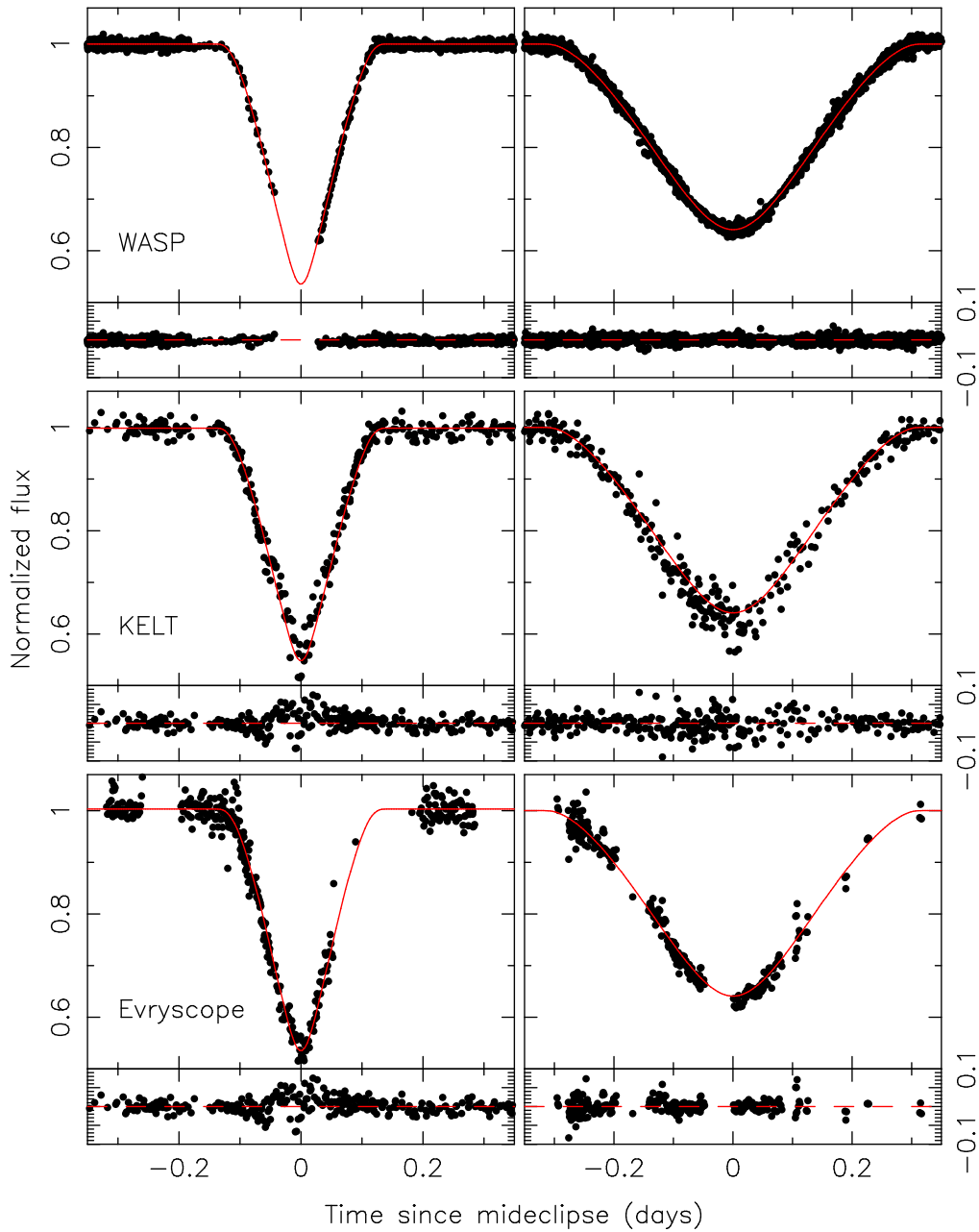


Figure 14. The archival photometric data during primary eclipse (left column) and secondary eclipse (right column). From top to bottom, the WASP data, the KELT data, and Evryscope data are shown, where the time of each observation has been converted to the difference in time from the nearest corresponding model (Family 5) eclipse. Comparing this figure to Figure 5 we see that the effects of the apsidal motion on the phase of the secondary have been accounted for in the model.

shown us that it is important to include the transit times in the fitting because the χ^2 penalty of the light-curve fit does not change once the predicted model transit does not overlap with the observed transit. When including the times, the likelihood of a model increases as the predicted transits get closer to the observed ones. We also have five “sets” of radial velocities: McDonald, TRES, Sophie, ARCES #1, and ARCES #2 (in the case of ARCES, we are fitting for the velocity difference between the two components). The systemic velocities for each set were fit separately as nuisance parameters, with primary and secondary velocities initially forced to have the same systemic velocity offset within each set.

For the model setup for TIC 1729, we have a total of 54 free parameters. There are parameters related to the orbit of the planet: the orbital period P_2 , the time of barycentric (inferior)

conjunction $T_{\text{conj},2}$, the eccentricity parameters $\sqrt{e_2} \cos \omega_2$ and $\sqrt{e_2} \sin \omega_2$, the inclination angle i_2 , and the nodal angle Ω_2 . There are similar parameters related to the binary orbit: the orbital period P , the time of barycentric conjunction T_{conj} , the eccentricity parameters $\sqrt{e} \cos \omega$ and $\sqrt{e} \sin \omega$, and the inclination angle i (the nodal angle of the binary is set to $\Omega = 0$). The mass and radius of the planet are specified by the mass ratio $Q_3 \equiv (M_1 + M_2)/M_3$ (i.e., the ratio of the binary mass to the planet mass) and the radius ratio R_1/R_3 (primary radius to planet radius). The component masses and radii for the binary are specified by the primary mass M_1 , the binary mass ratio $Q \equiv M_2/M_1$, the primary radius R_1 , and the radius ratio R_1/R_2 . The effective temperatures of the two stars are specified by the primary temperature T_1 and the temperature ratio T_2/T_1 . We have light curves in eight bandpasses, so

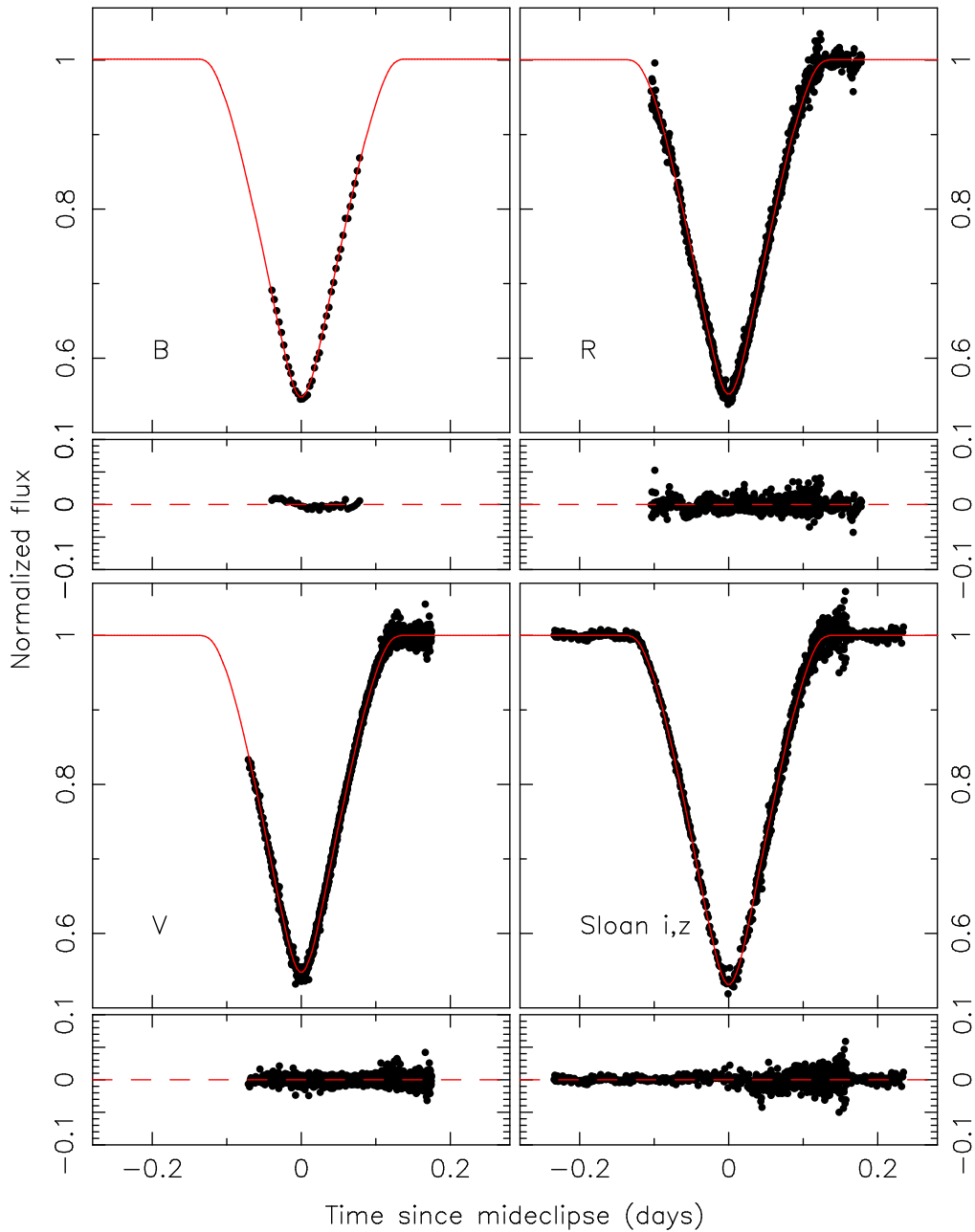


Figure 15. The ground-based follow-up photometry obtained after the transits were identified are shown for *B* (top left), *V* (bottom left), *R* (top right), and Sloan *i* and *z* (bottom right; see Tables 1 and 2 for details). The model curves are the best-fitting solution from Family 5.

consequently we have 32 sets of limb-darkening coefficients with two per star per bandpass. The standard quadratic limb-darkening law given by

$$I/I_0 = 1 - u_1(1 - \mu) + u_2(1 - \mu)^2$$

was used (where $\mu = \cos \theta$ is the projected distance from the center of the stellar disk), but with the “triangular” sampling technique of Kipping (2013) with coefficients given by $q_1 = (u_1 + u_2)^2$ and $q_2 = 0.5u_1(u_1 + u_2)^{-1}$. The remaining free parameters are the apsidal constants for the primary ($k_{2,1}$) and secondary ($k_{2,2}$), and a contamination parameter to account for the other sources of light in the TESS aperture.

ELC has several fitting algorithms available. For TIC 1729, the algorithms we used were a simple Markov Chain Monte Carlo (MCMC) algorithm outlined in Tegmark et al. (2004), a “differential evolution” MCMC algorithm (DE-MCMC, Ter Braak 2006), and the nested sampling algorithm outlined by Skilling (2006). In the case of TIC 1729, the size of the parameter space to search is relatively large given that most of the orbital parameters of the planet are not immediately known. The planet’s orbit is presumably close to edge-on given the two observed transits, but other than that the range of possibilities for the planet’s orbital period, eccentricity, and argument of periastron are fairly large. Regarding the orbital period of the planet, we can compute the minimum orbital period based on dynamical stability, and we find $P_{3,\min} \approx 129.7$ days (Quarles et al. 2018). As discussed in

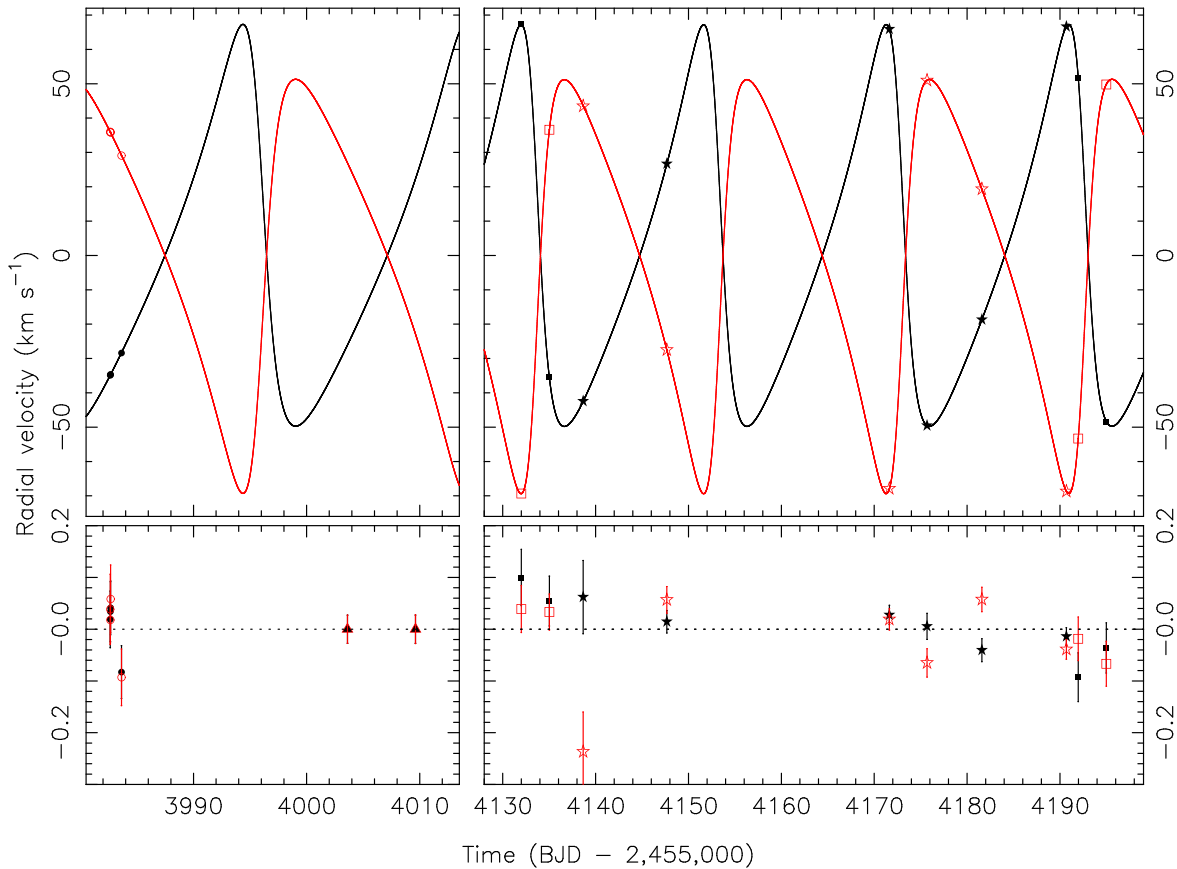


Figure 16. The radial velocities for the primary (black symbols) and the secondary (red symbols) and the best-fitting models from Family 5. The filled circles and open circles are the primary and secondary velocities from the McDonald spectra, respectively; the filled and open triangles are the primary and secondary velocities from the ARCES spectra, respectively (these were not used in the final fitting); the filled and open squares are the primary and secondary velocities from the TRES spectra, respectively; and the filled and open stars are the primary and secondary velocities from the SOPHIE spectra, respectively.

Kostov et al. (2020b), the orbital period of the planet can be estimated from the timings and durations of the two transits and the detailed knowledge of the binary’s orbit. Using this method, we estimated that the planet’s orbital period is likely in the range between 150 and 340 days for an eccentricity smaller than 0.2 (details presented below).

Our basic strategy was to use the nested sampling algorithm to find possible solutions, and then to use the MCMC and the DE-MCMC algorithms to refine them. In the nested sampling algorithm, one defines the parameter space by giving minimum and maximum values of the free parameters. One then randomly selects “live points,” where the number of them (N_{live}) should be at least twice the number of free parameters (N_{param}). The likelihood values for each live point are computed. The “sampling” part of the nested sampling algorithm is relatively straightforward. Select a point in parameter space at random, and evaluate the likelihood. If that likelihood is better than the likelihood of the worst live point, then replace that live point with the new point. The discarded live point goes into the list of “dead points.” If the new point has a worse likelihood than that of the worst live point, then that new point is discarded and not considered again. To make the sampling practical in a reasonably short period of time, the N_{param} -dimensional hyper-ellipsoid that bounds the live points is computed, and new possible points are randomly selected from the hyper-ellipsoid (for large dimensions, the volume of the hyper-ellipsoid can be orders of magnitude smaller than the volume of the

hyper-cube defined by the ranges of each fitting parameter). As better live points are found, the volume of the hyper-ellipsoid shrinks and potential replacement points are sampled from increasingly relevant regions of parameter space. Skilling (2006) showed that if the volume of the hyper-ellipsoid is successively scaled by a factor proportional to $1/N_{\text{live}}$, then the live points and dead points can be used to compute the Bayesian evidence and also to construct a posterior sample. Unfortunately, when the number of parameters N_{param} is larger than about 20, the statistically scaled volume of the hyper-ellipsoid is usually orders of magnitude larger than the actual volume of the hyper-ellipsoid. As a result, it can take a very long time (a few weeks of wall-clock time or longer for cases like TIC 1729) to run the nested sampling algorithm to completion, even when using a parallelized version that runs on multiple computer cores since the random samples usually come from regions of parameter space that are far from the region that has the largest likelihood. In our implementation of the nested sampling algorithm, we have the option of omitting the statistical scaling of the volume of the hyper-ellipsoid. The advantage of this is that it is much faster to find replacements for the live points since the volume from which the random samples are drawn is generally much smaller. Although we forfeit the ability to compute a posterior sample or to compute the evidence, the increased speed at which the algorithm can find good solutions as starting points for other algorithms makes up for this shortcoming.

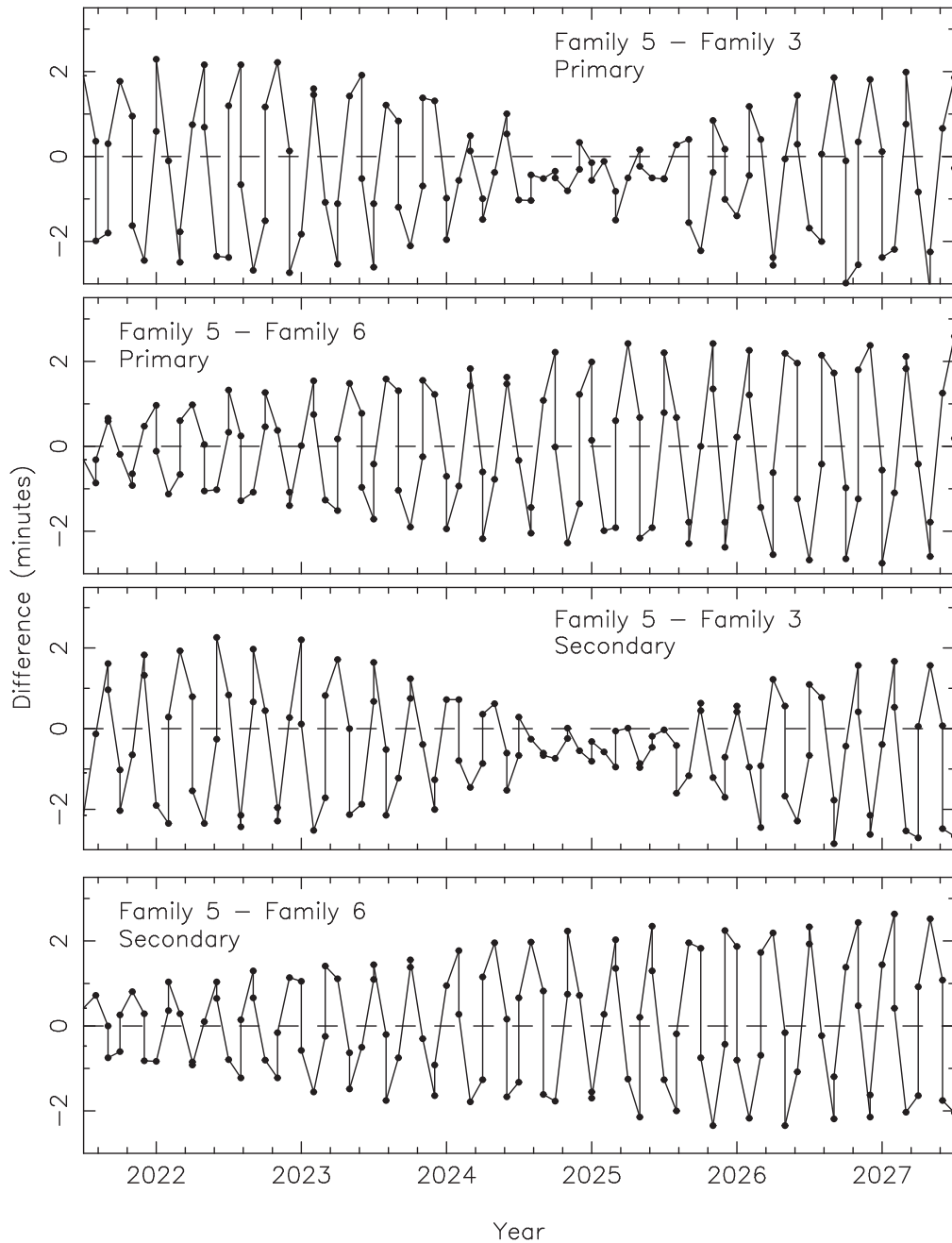


Figure 17. Differences in the times of predicted eclipses between the Family 3, Family 5, and Family 6 solutions out to the middle of the year 2027. The differences can be up to ≈ 2 minutes (the timing depends on the combination of which families are in the difference) and should be measurable.

Our quest to find good model solutions proceeded by iteration. When running the nested sampling algorithm, we kept the limb-darkening coefficients fixed, which left us with 22 free parameters and 44 live points. It is usually the case that when modeling circumbinary systems, reasonably good parameters for the binary can be found quickly, whereas good parameters for the planet (its orbital parameters and its mass) take longer to find. Once a good solution for the binary’s parameters was found in the first run of the nested sampling, we used the MCMC and the DE-MCMC algorithms to refine the solution, which included the limb-darkening coefficients. With better values for the limb-darkening parameters, the nested sampling was run again with the limb-darkening coefficients fixed at better values. For the second iteration of the nested sampling,

we used 66 live points. As the progress of the second run was monitored, it was found that not all values of the orbital period of the planet near the best value were possible. Instead, there are distinct families of solutions as shown in Figure 13. The figure shows the evolution of the live points as they are replaced with better models. We note that this is a representative figure based on the 2020 data. The “fingers” persist after the inclusion of the 2021 data (discussed below) but recreating this figure with all available data proved to be computationally prohibitive. However, we confirmed the pattern by using brute-force steppers in the planet period and found that regions of high χ^2 quickly emerge between the fingers, and the best-fit planet periods shift by about a day (compare location of fingers here to the periods listed in

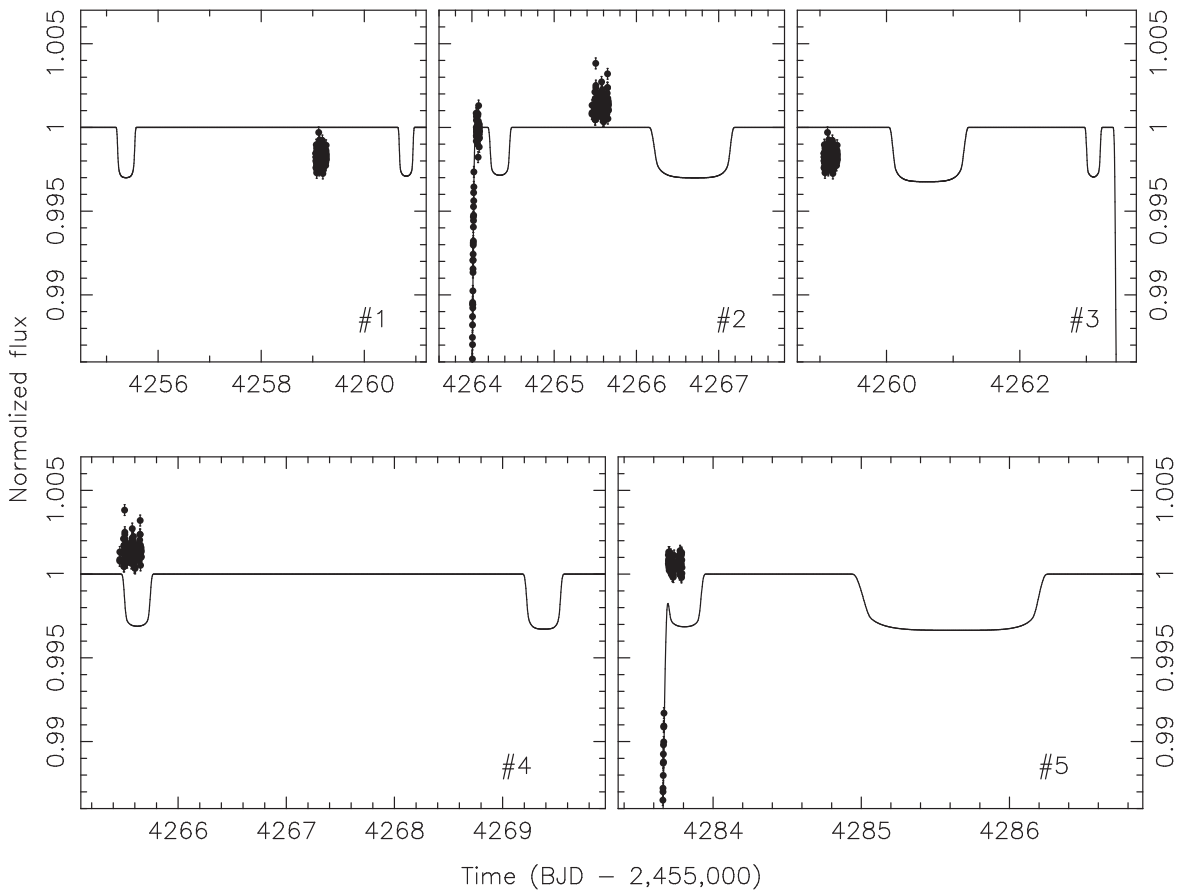


Figure 18. The five CHEOPS visits from 2021 February and March along with the predicted eclipses from Families 1 through 5 (note the data near day 4259 are shown twice). The egress part of an eclipse and some of the out-of-eclipse light curve were observed near day 4264, and the data from all five visits were normalized to that out-of-eclipse part of the light curve. Small but significant zero-point offsets are seen.

Table 6). At first (small y -values in the plot), the planet’s period among the live points fills the range between about 180 and 210 days nearly uniformly. As better live points are found (moving up the y -axis), distinct “fingers” develop, and at the end, six families of solutions remain (top of the y -axis). This represents a problem for the nested sampling algorithm. The range of the planet periods is still fairly large, so the hyper-ellipsoid cannot become very small. Moreover, many, if not most, of the randomly selected points will fall in between the fingers where the likelihood is not very high. As a result, the convergence of the algorithm is slowed. In cases like this, the “multinest” routine discussed by Feroz et al. (2009), might offer relief, but we do not have an implementation of multinest within ELC.

As an aside, we do not have a good explanation of why we see these families of solutions with distinct values of the planet’s period, as opposed to a smooth distribution of points with a range of $\approx 10\%$ – 20% around the best value that one might expect based on the discussion in Kostov et al. (2020b). It is tempting to think that these discrete solutions are somehow analogous to some kind of aliasing caused by cycle count ambiguities over the relatively long time baseline we have (about 5600 days or about 15 yr). However, the fingers still appear when we only include the TESS data and the follow-up photometric data that were taken after the transits were identified. We note that the CBP Kepler-34 produced a “1–2 punch” where a pair of transits about 5 days apart were observed with Kepler (Welsh et al. 2012), but when we fit only

those two transits (along with the stellar eclipses and radial-velocity data) using the nested sampling in a similar manner that was used on TIC 1729, we found only a broad range of possible planet periods with no distinct and separate families of solutions. Thus, it appears that the appearance of these distinct families of solutions is related to the peculiarities of TIC 1729 itself rather than being a generic feature of only having a pair of observed transits with a few days between them.

These distinct families of solutions with regions of low likelihood between them also present problems for the MCMC and the DE-MCMC algorithms. We therefore broke up the parameter space into six regions where the range of the planet’s period was restricted in such a way to isolate each family, and leaving the ranges of the other 53 parameters to be the same (the identifying numbers for each family are shown in Figure 13). Using the best nested sampling solution from each family as an initial seed (see Orosz et al. 2019, for a discussion on how the chains are initialized), the DE-MCMC algorithm was run on each family. After these preliminary runs, we noticed two minor issues. First, the residuals for the secondary star radial velocities were systematically larger than the residuals for the primary star radial velocities by $\approx 75 \text{ m s}^{-1}$. Second, a comparison of the stellar masses and radii with stellar evolution models (see Section 4.1) showed a poor fit. We therefore made two modifications. First, with a physical interpretation in mind such as convective blueshift and gravitational redshift, we allowed the systemic radial velocities of the primary and secondary star to vary independently

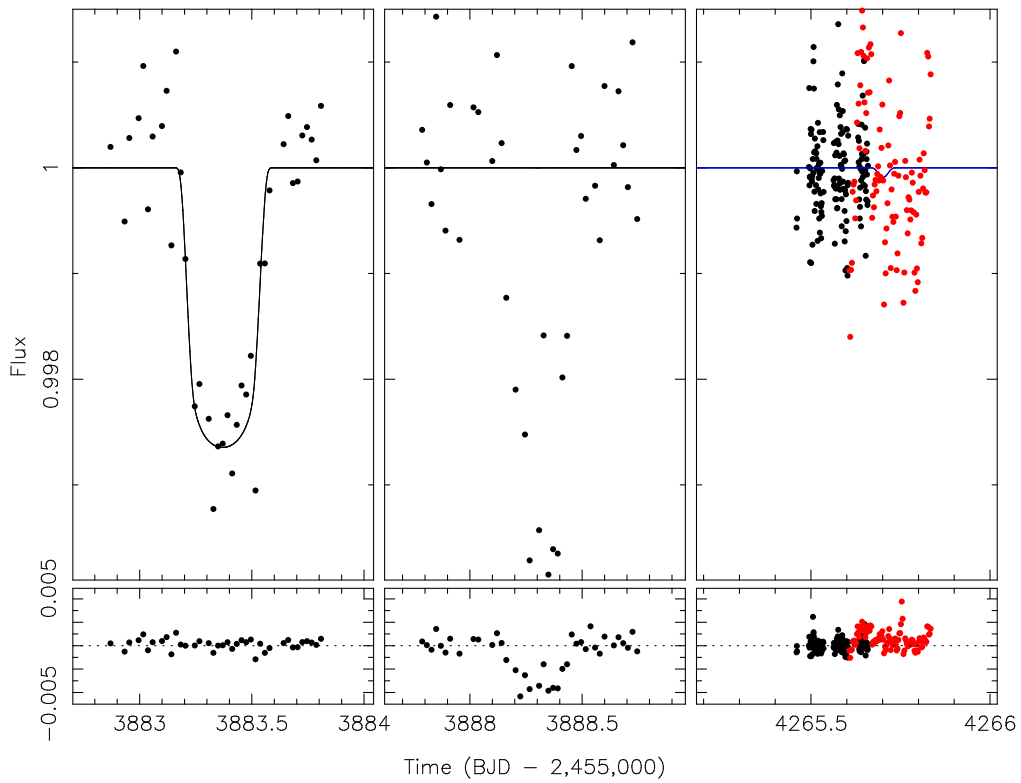


Figure 19. Left: the transit of the primary star observed by TESS according to the best-fitting Family 4 model and using only the CHEOPS data. Middle: same as the left panel but for the transit of the secondary star. Right: CHEOPS data (black points) and KeplerCam data (red points, binned to ≈ 2 minutes) during a potential transit of the secondary for the Family 4 solution. The best-fitting model is the solid line. The transit of the secondary observed by TESS is not matched and thus Family 4 can be likely ruled out (see text for details).

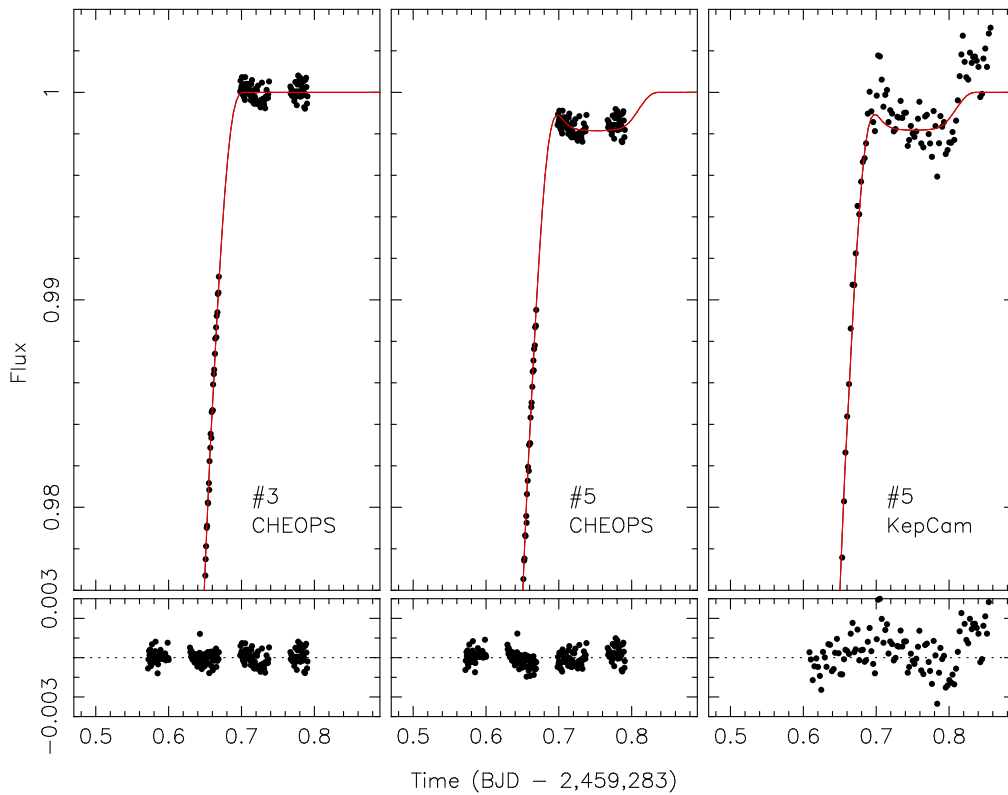


Figure 20. Left: the CHEOPS data from day 4283 with the best-fitting Family 3 model. Middle: the same CHEOPS data with the best-fitting Family 5 model. Right: The nearly simultaneous KeplerCam data (binned to ≈ 2 minutes), with the best-fitting Family 5 model. Overall, Family 5 remains a viable solution.

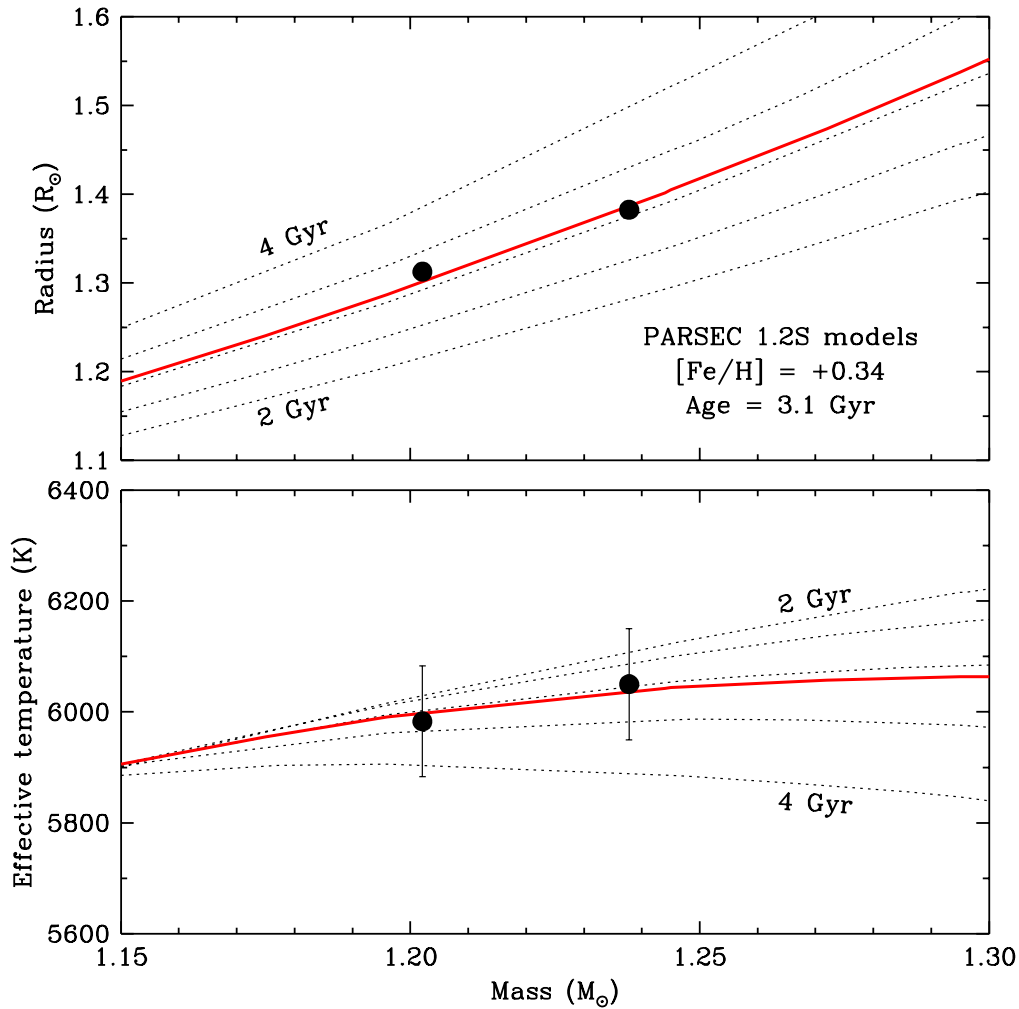


Figure 21. Comparison of the mass, radius, and temperature determinations for the components of TIC 1729 against stellar evolution models from the PARSEC series (Chen et al. 2014) for the best-fitting composition of $[\text{Fe}/\text{H}] = +0.34$, and solar-scaled abundances ($[\alpha/\text{Fe}] = 0.0$). Top: mass–radius diagram with isochrones from 2 to 4 Gyr, every 0.5 Gyr, indicated with dotted lines. The best fit for an age of 3.1 Gyr is shown by the red line. Error bars are smaller than the symbol size. Bottom: mass–temperature diagram showing the same isochrones as above.

for each radial-velocity set. With this modification we can no longer use the ARCES velocities since we were fitting for the difference between the primary and secondary velocities. Second, we used the flux fraction as an observed constraint. As discussed previously, there is no apparent trend in the flux fractions with wavelength, so we adopted a flux fraction of 0.8669 ± 0.0037 for each bandpass.

After these modifications, the DE-MCMC code was run seven times for each family, with each run lasting 15,000 generations. After a generous burn-in period of 7500 generations, posterior samples were taken from every 1500th generation for each run and combined. For each posterior distribution (each of which had 8064 samples), the numbers are sorted and we computed the median value X_{med} , the value $X_{15.85}$ that marks the point where 15.85% of the distribution is smaller, and the value of $X_{84.15}$ that marks the point where 15.85% of the distribution is larger (i.e., 68.3% of the distribution is between $X_{15.85}$ and $X_{84.15}$). The adopted parameter value is taken to be the median X_{med} , and the 1σ uncertainty is taken to be the larger of $(X_{\text{med}} - X_{15.85})$ or $(X_{84.15} - X_{\text{med}})$. The results for the fitted parameters are shown in Table 5, and for some derived parameters of interest in Table 6. From looking at Table 5, the solution for Family 5 (where $P_3 = 200.452$ days) has the smallest overall χ^2 , with $\chi^2_{\text{min}} = 11,348.96$. The solutions for the

other families are nearly as good with χ^2_{min} values within ≈ 280 . At this time it is difficult to choose between these these families with high confidence.

Figures 2, 14, and 15 show the various photometric data and the best-fitting models (for Family 5). There do not appear to be any large systematic problems with the model fits. Comparing Figure 5, where the data are phased with a linear ephemeris, and Figure 14, where the times are relative to the nearest corresponding eclipse, we see that the apsidal motion is accounted for in the model. Finally, Figure 16 shows the radial velocities and the best-fitting model (for Family 5). The velocity residuals are all less than 200 meters per second. The residuals for the McDonald spectra are even tighter still, with a scatter of around 20 meters per second.

In each of the three spectroscopic data sets the fitted center-of-mass velocities for the primary and secondary components are systematically different, and are always larger for the secondary. The differences (secondary minus primary) are $+0.030 \pm 0.023 \text{ km s}^{-1}$ for McDonald, $+0.082 \pm 0.005 \text{ km s}^{-1}$ for TRES, and $+0.076 \pm 0.008 \text{ km s}^{-1}$ for SOPHIE. While in principle this could result from instrumental effects, the fact that the sign is the same for all three instruments, and the magnitudes quite similar, suggests an alternate explanation of an astrophysical nature. The

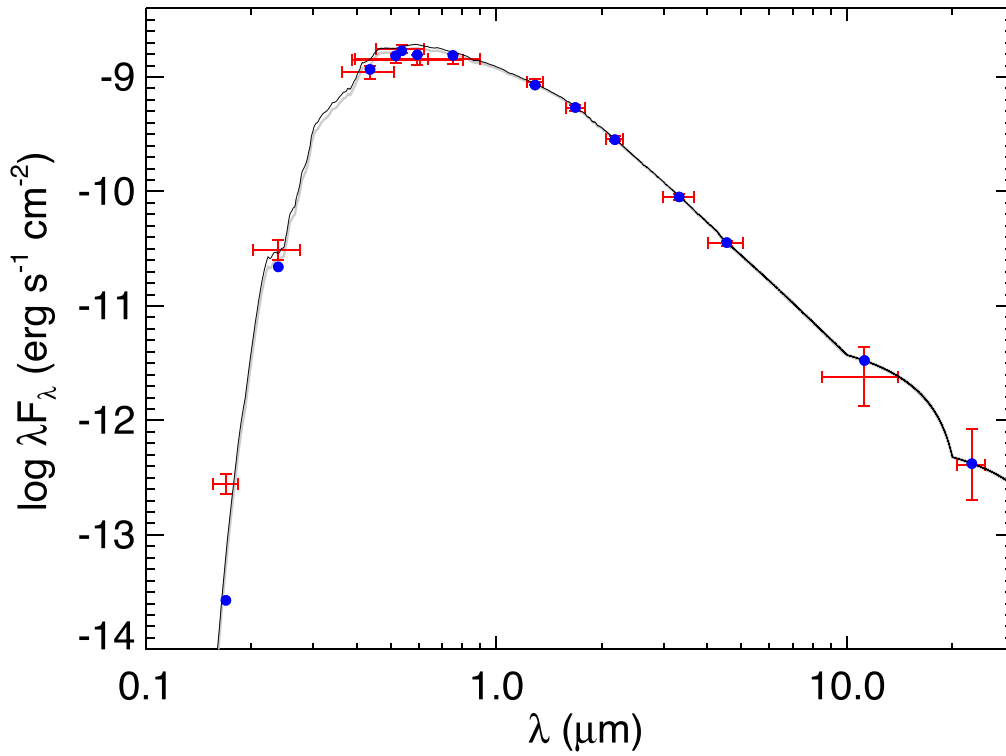


Figure 22. Spectral energy distribution of TIC 1729 showing the fit obtained by combining two stellar components with effective temperatures and radii as described in the text. The solid line is the best-fit Kurucz atmosphere model (reddened in gray, unreddened in black), blue dots are the predicted fluxes in each observed bandpass (see the text), and the measurements are indicated with red error bars (the horizontal ones representing the wavelength range).

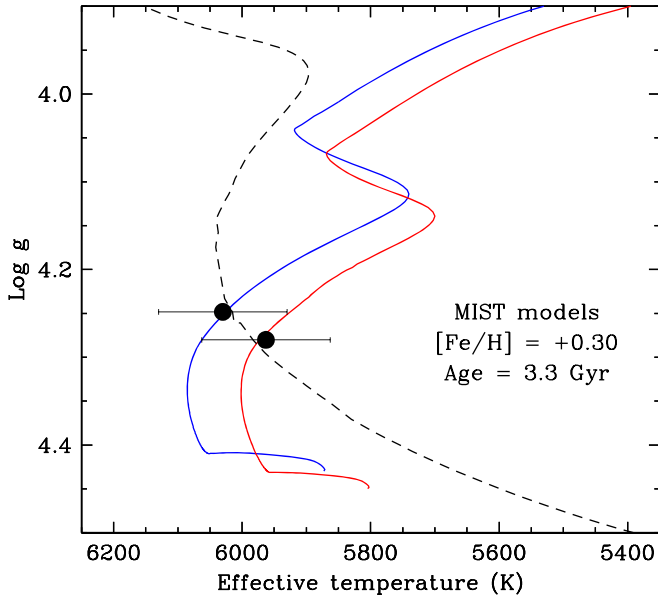


Figure 23. Observations for TIC 1729 compared against evolutionary tracks from the MIST series of models (Choi et al. 2016), for the exact masses we measured. The models match the observations for a metallicity of $[\text{Fe}/\text{H}] = +0.30$ (solar-scaled abundances), and an age of 3.3 Gyr indicated by the dashed-line isochrone. The blue/red lines correspond to the primary/secondary, respectively.

component properties (mass, radius, and temperature) differ by less than 5%, yet this is enough to cause perceptible differences in the gravitational redshift, which we expect to be larger for the secondary by 0.010 km s^{-1} . Although convective blueshifts are not as easy to quantify, based on the prescription by Dravins

Table 3
Stellar Parameters for TIC 172900988

Parameter	Value	Error	Source
Identifying Information			
TIC ID	172900988		TIC
Gaia ID	709709093301608448		Gaia EDR3
Tycho Reference ID	2483-160-1		TRC
α (hh:mm:ss)	08:34:38.799192	0.000013	Gaia EDR3
δ (dd:mm:ss)	+31:33:14.314250	0.00010	Gaia EDR3
μ_α (mas yr $^{-1}$)	-6.5329	0.0145	Gaia EDR3
μ_δ (mas yr $^{-1}$)	-22.8868	0.0115	Gaia EDR3
π (mas)	4.0607	0.0149	Gaia EDR3
Distance (pc)	246.263	0.904	Gaia EDR3
Photometric Properties			
V (mag)	10.141	0.006	TIC
Gaia (mag)	10.0477	0.0006	Gaia EDR3
T (mag)	9.6319	0.0078	TIC
Contamination	0.000453		TIC
Stellar Properties			
T_{eff} (K)	6030	100	TIC
$T_{\text{eff}, 1}$ (K)	6050	100	This work
$T_{\text{eff}, 2}$ (K)	5983	100	This work
$[\text{Fe}/\text{H}]$	+0.34	0.10	This work
Age (Gyr)	3.1	0.1	This work

et al. (1999) we expect the effect to be roughly 0.060 km s^{-1} smaller for the secondary, resulting in a more positive velocity for that component. The two effects combine to give a larger expected velocity for the secondary by about 0.070 km s^{-1} , which appears to explain the bulk of the shifts mentioned above.

Table 4
Radial Velocities for TIC 172900988

Time (BJD-2,455,000)	Date	Primary Velocity (km s ⁻¹)	Secondary Velocity (km s ⁻¹)	Instrument
3982.63491	2020-May-13T03:14:15.8	-9.248 ± 0.060	61.677 ± 0.067	Tull
3982.65341	2020-May-13T03:40:54.9	-9.114 ± 0.064	61.534 ± 0.043	Tull
3982.67077	2020-May-13T04:05:54.7	-8.995 ± 0.057	61.460 ± 0.064	Tull
3983.63222	2020-May-14T03:10:24.2	-2.758 ± 0.056	54.759 ± 0.054	Tull
4003.61687	2020-Jun-03T02:48:17.6	0.000 ± 0.027	53.057 ± 0.027 ^a	ARCES
4009.62264	2020-Jun-09T02:56:35.8	0.000 ± 0.027	-44.992 ± 0.028 ^a	ARCES
4131.99887	2020-Oct-09T11:58:22.1	93.471 ± 0.111	-43.072 ± 0.066	TRES
4135.02023	2020-Oct-12T12:29:08.2	-9.340 ± 0.098	62.841 ± 0.051	TRES
4138.65484	2020-Oct-16T03:42:58.3	-16.383 ± 0.071	69.606 ± 0.077	Sophie
4147.67188	2020-Oct-25T04:07:30.9	52.738 ± 0.022	-1.369 ± 0.026	Sophie
4147.67188	2020-Oct-25T04:07:30.9	52.738 ± 0.022	-1.369 ± 0.026	Sophie
4153.67808	2020-Oct-31T04:16:26.4	Sophie
4164.70059	2020-Nov-11T04:48:50.7	Sophie
4171.63576	2020-Nov-18T03:15:29.8	91.962 ± 0.019	-41.769 ± 0.021	Sophie
4175.69111	2020-Nov-22T04:35:11.8	-23.475 ± 0.025	77.104 ± 0.027	Sophie
4181.59568	2020-Nov-28T02:17:47.0	7.353 ± 0.022	45.441 ± 0.024	Sophie
4190.69055	2020-Dec-07T04:34:23.7	92.689 ± 0.017	-42.547 ± 0.019	Sophie
4191.97004	2020-Dec-08T11:16:51.5	77.852 ± 0.096	-27.075 ± 0.061	TRES
4194.99147	2020-Dec-11T11:47:42.7	-22.177 ± 0.099	76.021 ± 0.063	TRES

Note.

^a Velocity difference between primary and secondary.

As noted earlier, the solution for Family 5 is formally the best. With one exception, there does not seem to be any pattern in how the various parameters change from family to family. That one exception is the mass of the planet: it is the smallest ($M_3 = 823.9 \pm 4.8 M_{\oplus}$) for Family 1 (where the planet's period P_3 is the shortest) and largest ($M_3 = 981.3 \pm 5.7 M_{\oplus}$) for Family 6 (where the planet's period P_3 is the largest). This trend is easy to understand. The planet is responsible for most of the apsidal motion seen in the binary. As the planet's orbital period gets longer, the planet's mass needs to go up to have the same effect on the binary.

Future transit and eclipse observations will allow us to determine which family represents the correct solution. We used the models from the posterior samples for each family to compute the times (and their uncertainties) of future transits (see Table 7) and eclipses (see Tables 8–19 in the Appendix). As one might expect, the predicted times of the next pair of observable transits depends on the orbital period of the planet. A clear detection of one or more transits in the future will unequivocally tell us which family represents the true solution. If future transit observations are not available, then observations of future eclipses will eventually allow us to discriminate between the various families. Figure 17 shows differences in the predicted eclipse times between Family 5 and Family 3, and between Family 5 and Family 6. The differences between the predicted times can be on the order of one to two minutes, which should be easy to detect.

Finally, we note that there is a distinction between the initial conditions of the best-fitting models for each family and the parameters given in Table 5, which come from the medians of the posterior distributions. The parameters in Table 5 represent our best estimates of the parameters and their statistical uncertainties. However, those parameters collectively will not necessarily produce an optimal fit to the data owing to the complexity of the model and correlations among the various parameters. For the purposes of computing an optimal model, the initial conditions for the best-fitting models should be used.

The initial conditions for the best-fitting models for all of the families are given in Tables 20–25 in the Appendix.

3.2. Observational Data for Predicted Transits in 2021 February–March

The photodynamical model predicted transits of the planet occurring during a conjunction in early 2021 (February–March, depending on the family). To detect the transits, we obtained four observations from CHEOPS via a generous allocation of Director's Discretionary Time. These data are shown in Figure 18. We note that these observations were scheduled to be centered on the predicted transit ingress corresponding to the best-fit model for the respective family based on the radial-velocity data available at the time, i.e., less than half of the RV measurements. As we received more measurements, the model fit to the binary star in particular improved and, as a result, some of the times of the predicted transits changed. This is the reason the current best-fit transit models for Family 1, 2, and 3 do not overlap with the CHEOPS observations.

The egress part of an eclipse was observed near day 4264, and this observation includes a small part of the out-of-eclipse light curve. A fit to this partial eclipse was used to normalize all of the CHEOPS data. CHEOPS data were obtained near the expected transits for the Family 4 and Family 5 solutions. Unfortunately, there are two problems that make the interpretation of these data difficult. First, there are small but significant flux offsets between each visit as seen in Figure 18 (e.g., the observations covering out-of-eclipse phases in panels 1, 2, and 3 have fluxes that are different by a few tenths of a percent). These offsets might be produced by either a genuine stellar variability (which would be undetectable in TESS data), or could represent a systematic instrumental effect. Second, the duration of each visit was relatively short. As a result, the data near day 4266 could be consistent with being at the bottom of the Family 4 transit, or could be consistent with the out-of-transit light curve for all other families. Likewise, the predicted transit from the Family 5 solution partially overlaps with the egress of an eclipse. The light curve at the end of the corresponding CHEOPS visit is flat, but that could be consistent with being the out-of-eclipse light curve

Table 5
Fitted Parameters for TIC 172900988^a

Parameter	Family 1	Family 2	Family 3	Family 4	Family 5	Family 6
χ_{\min}^2	11,410.26	11,192.97	11,174.33	11,164.23	11,141.53	11,187.00
Planet orbital parameters						
P_2 (days)	188.835 ± 0.092	190.375 ± 0.053	193.965 ± 0.078	198.856 ± 0.099	200.452 ± 0.011	204.046 ± 0.057
$T_{\text{conj},2}^b$	3976.3 ± 2.2	3932.5 ± 1.1	3877.5 ± 2.8	3954.2 ± 3.1	3937.5 ± 0.5	3932.0 ± 0.9
$\sqrt{e_2} \cos \omega_2$	-0.2779 ± 0.0048	-0.2510 ± 0.0070	-0.2677 ± 0.0068	-0.2810 ± 0.0045	-0.1536 ± 0.0063	-0.1150 ± 0.0126
$\sqrt{e_2} \sin \omega_2$	-0.0734 ± 0.0091	-0.0058 ± 0.0176	0.0329 ± 0.0144	-0.0951 ± 0.0083	0.0578 ± 0.0149	0.1168 ± 0.0213
i_2 (deg)	88.20 ± 0.21	88.18 ± 0.19	89.67 ± 0.25	91.84 ± 0.20	91.79 ± 0.19	90.50 ± 0.32
Ω_2 (deg)	-0.88 ± 0.22	-0.74 ± 0.17	-2.18 ± 0.24	0.72 ± 0.17	0.32 ± 0.11	1.65 ± 0.15
Planet parameters						
M_3 (M_{\oplus})	823.9 ± 4.8	845.7 ± 4.7	837.0 ± 4.7	869.7 ± 5.0	942.0 ± 5.6	981.3 ± 5.7
R_1/R_3	13.44 ± 0.54	13.54 ± 0.50	13.36 ± 0.47	13.49 ± 0.52	13.42 ± 0.53	13.40 ± 0.47
Binary orbital parameters						
P_1 (days)	19.657444	19.658083	19.658171	19.656652	19.658173	19.658016
	±0.000027	±0.000035	±0.000030	±0.000033	±0.000025	±0.000040
$T_{\text{conj},1}^b$	3878.1746	3878.3572	3878.3823	3877.9473	3878.3835	3878.3386
	±0.0079	±0.0100	±0.0085	±0.0095	±0.0072	±0.0114
$\sqrt{e_1} \cos \omega_1$	0.23338 ± 0.00008	0.23326 ± 0.00008	0.23324 ± 0.00008	0.23354 ± 0.00008	0.23323 ± 0.00008	0.23326 ± 0.00008
$\sqrt{e_1} \sin \omega_1$	0.62716 ± 0.00017	0.62718 ± 0.00017	0.62729 ± 0.00015	0.62721 ± 0.00015	0.62730 ± 0.00016	0.62728 ± 0.00015
i_1 (deg)	89.4182 ± 0.0049	89.4198 ± 0.0051	90.5940 ± 0.0046	90.5795 ± 0.0046	90.5762 ± 0.0047	89.4077 ± 0.0055
Ω_1 (deg)	0 ^c	0 ^c	0 ^c	0 ^c	0 ^c	0 ^c
Stellar parameters						
M_1 (M_{\odot})	1.2388 ± 0.0008	1.2388 ± 0.0007	1.2388 ± 0.0007	1.2388 ± 0.0007	1.2384 ± 0.0007	1.2384 ± 0.0007
$Q \equiv M_2/M_1$	0.9706 ± 0.0003	0.9706 ± 0.0003	0.9706 ± 0.0003	0.9705 ± 0.0003	0.9705 ± 0.0003	0.9706 ± 0.0003
R_1 (R_{\odot})	1.3846 ± 0.0019	1.3841 ± 0.0020	1.3842 ± 0.0017	1.3843 ± 0.0017	1.3842 ± 0.0016	1.3844 ± 0.0016
R_1/R_2	1.0527 ± 0.0017	1.0535 ± 0.0017	1.0539 ± 0.0016	1.0532 ± 0.0015	1.0547 ± 0.0015	1.0558 ± 0.0015
T_2/T_1	0.9903 ± 0.0029	0.9887 ± 0.0035	0.9882 ± 0.0022	0.9864 ± 0.0024	0.9866 ± 0.0030	0.9833 ± 0.0027

Notes.

^a Instantaneous parameters valid at BJD 2,453,250.0.

^b BJD-2,455,000.

^c Fixed.

for Families 1 through 4 and Family 6, or it could be consistent with the bottom of the transit for the Family 5 solution.

We attempted to separately fit the CHEOPS data near the Family 4 and Family 5 transits. ELC is currently limited to eight distinct filter bandpasses, so we removed the data for the *B* filter and replaced the specific intensities in the model atmosphere table with intensities for CHEOPS using the appropriate filter response.

Thanks to a fantastic response from the community, we also obtained several ground-based observations of the predicted transits. In particular, for the potential Family 4 transit we obtained observations from KeplerCam in the Sloan *i* filter. These data are consistent with a flat line, as seen in Figure 19, where we also show the results of the fitting of the potential Family 4 solution using both the CHEOPS (black points) and KeplerCam (red points). We note that it is possible to orient the planet's orbit in such a way that no transit is observable near day 4265.5, so the model near the CHEOPS data and KeplerCam data is nearly flat. However, this occurs at the expense of the fit to the transit of the secondary star observed by TESS (middle panel in the figure). As a result, we can likely rule out the Family 4 solution, although the confidence level is not as high as one would normally like.

For the potential Family 5 transit, we also have KeplerCam observations that are nearly simultaneous with the CHEOPS observations, so we fit these data in a similar manner as above.

The results are shown in Figure 20. Here, the families where there is no transit blended with the egress of the eclipse fit the CHEOPS data better than does the Family 5 model ($\chi^2 \approx 249$ versus $\chi^2 = 290$ for Family 5). However, the Family 5 model fits the KeplerCam data better than the other families ($\chi^2 = 4089$ for Family 5 versus $\chi^2 \approx 4381$ for the others). Given the relatively short time span of the follow-up observations and the noise present in the KeplerCam data (especially near the end when morning twilight was approaching), Family 5 remains a viable solution.

We also attempted to catch some of the predicted transits from TRAPPIST-North but the observations did not reach the necessary precision.

4. Discussion

4.1. Stellar Properties and Comparison with Stellar Evolution Models

We discuss here the determination of the effective temperatures of the binary components as well as the system metallicity, based on the TRES spectra of TIC 1729 described earlier. We followed a cross-correlation procedure similar to the one described by Torres et al. (2002) to optimize the match of the observed spectrum against synthetic spectra, except that in this case the spectrum is double lined, so instead of 1D cross-correlations we used TODCOR (Zucker & Mazeh 1994),

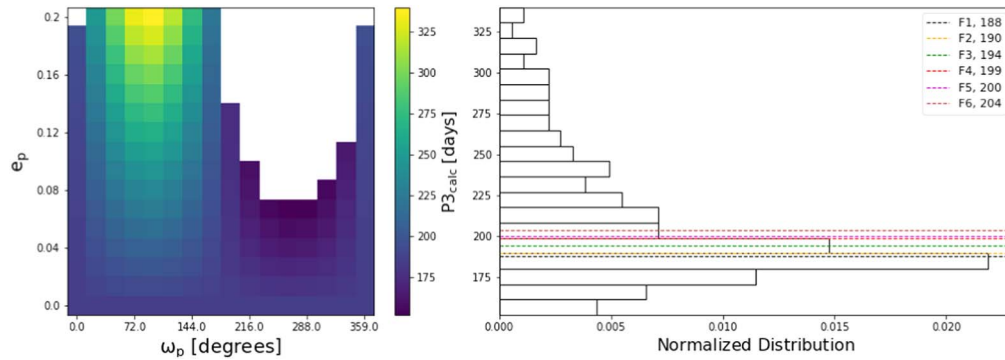


Figure 24. Left panel: calculated CBP orbital period ($P_{3,\text{calc}}$) based on the duration of the detected transits and using the RV-derived EB parameters (Kostov et al. 2020b), as a function of (e_3, ω_3), and for $e_3 = [0.0, 0.2]$. The white area represents $P_{3,\text{calc}}$ that is ruled out based on Quarles et al. (2018) critical eccentricity, i.e., $0.8(1 - (P_{3,\text{stab}}/P_{3,\text{calc}})^{2/3})$, where $P_{3,\text{stab}} = 129.7$ days. Right panel: normalized distribution of $P_{3,\text{calc}}$. The horizontal dashed lines represent the true value P_3 from the photodynamical modeling for the six families of solutions presented above.

which is a two-dimensional correlation algorithm. This allows us to account for the presence of the secondary star in determining the stellar properties. Calculated templates were taken from a library of pre-computed spectra based on model atmospheres by R. L. Kurucz (see Nordström et al. 1994; Latham et al. 2002) covering the region centered on the Mg I b triplet at 5187 \AA . We ran a grid of correlations solving for a mean effective temperature (strictly, a luminosity-weighted mean) and the rotational broadening of components, $V_{\text{rot}} \sin i$, assumed to be the same for the two stars. Initial tests indicated the rotational broadening is below our spectral resolution, so we adopted $V_{\text{rot}} \sin i = 0 \text{ km s}^{-1}$. As discussed by Torres et al. (2012), the temperatures determined in this way tend to be strongly correlated with the surface gravity and with metallicity, with higher values of these parameters leading to hotter temperatures. Given that in this case the surface gravities are well determined from the photodynamical analysis, we fixed them to a common value of $\log g = 4.25$, near the average for the two components. On the assumption that the metallicity is solar, the resulting mean temperature we obtained is $\langle T_{\text{eff}} \rangle = 5770 \text{ K}$. Increasing the metallicity to $[\text{Fe}/\text{H}] = +0.5$ gave a hotter mean temperature of $\langle T_{\text{eff}} \rangle = 6140 \text{ K}$, as expected. Estimated uncertainties for these values are 100 K . Individual temperatures for the components were then computed by using the temperature ratio as measured from the photodynamical analysis.

A preliminary comparison against stellar evolution models from the PARSEC 1.2S series (Chen et al. 2014) indicated a satisfactory fit in the mass–radius plane for either metallicity (at different ages), but revealed that the predicted temperatures were hotter than we obtained when assuming solar metallicity, and cooler than we obtained when adopting the higher composition of $[\text{Fe}/\text{H}] = +0.5$. We then explored intermediate metallicity values, and found good agreement in both the mass–radius and mass–temperature diagrams for a composition of $[\text{Fe}/\text{H}] = +0.34 \pm 0.10$. The mean system temperature at this composition is 6030 K , and the individual values are 6050 and 5983 K for the primary and secondary, respectively, corresponding to spectral types of approximately F9 and G0. This fit is shown in Figure 21, in which model isochrones are plotted for ages between 2 and 4 Gyr, in steps of 0.5 Gyr. The best simultaneous agreement with all observations is achieved for an age of about 3.1 Gyr, according to these models.

As an independent test on the absolute temperatures, we gathered photometry for TIC 1729 from the literature and

constructed 14 different but nonindependent color indices. We de-reddened them using an estimate of the interstellar reddening of $E(B - V) = 0.03$ from Schlafly & Finkbeiner (2011), and then applied 19 different empirical color–temperature calibrations from Casagrande et al. (2010) and Huang et al. (2015). Adopting $[\text{Fe}/\text{H}] = +0.34$ from the spectroscopic analysis above, we obtained a mean photometric temperature of $\langle T_{\text{eff}} \rangle = 5940 \pm 100 \text{ K}$, marginally lower than the spectroscopic value, but within the uncertainties.

We ran an additional test on the spectroscopic parameters by performing a fit of the spectral energy distribution (SED) of TIC 1729 using the methods of Stassun & Torres (2016). Brightness measurements in the GALEX near-ultraviolet, Tycho-2 (B_T, V_T), Gaia ($G, G_{\text{BP}}, G_{\text{RP}}$), 2MASS (J, H, K_S), and WISE (W1–W4) passbands were gathered from the VizieR database, and cover the range from 0.2 to $22 \mu\text{m}$ (Figure 22). In addition, we pulled the GALEX far-ultraviolet flux to provide an estimate of the chromospheric activity. With the $\log g$ and effective temperature values as above, we obtained an excellent fit with $\chi_\nu^2 = 0.85$ (excluding the far-ultraviolet flux, which appears in excess) and a best-fit extinction $A_V = 0.08 \pm 0.03$. The best-fit metallicity is $[\text{M}/\text{H}] = +0.25 \pm 0.05$, strongly constrained by the near-ultraviolet flux in particular; this is somewhat lower but comparable to the estimate of $+0.34$ above. The distance inferred from comparing the integrated bolometric flux to the bolometric luminosity given by the radii and temperatures is $241.0 \pm 3.6 \text{ pc}$, consistent with the distance of $245.0 \pm 2.7 \text{ pc}$ from Gaia EDR3, adjusted by the parallax offset recommended by Lindegren et al. (2021).

The above results clearly point to a supersolar composition for TIC 1729, which is consistent with expectations for a massive planet and late F- to early G-type stars of the masses we determine (see, e.g., Santos et al. 2017).

To illustrate the evolutionary state of the stars, Figure 23 compares the surface gravity and temperature determinations against a different set of models from the MIST series (Choi et al. 2016). Evolutionary tracks are shown for the measured masses, and a metallicity of $[\text{Fe}/\text{H}] = +0.30 \pm 0.10$ that best fits the observations, at which the individual spectroscopic temperatures are 6030 and 5963 K for the primary and secondary (6000 K for the luminosity-weighted mean). The best-fit age is 3.3 Gyr. These results are consistent with those obtained from the PARSEC models. Both stars are seen to be evolved, and are near the midpoint of their main-sequence lifetimes. For the final stellar parameters we adopt the average

Table 6
Derived Parameters for TIC 172900988^a

Parameter	Family 1	Family 2	Family 3	Family 4	Family 5	Family 6
Planet orbital parameters						
P_2 (days)	188.835 ± 0.092	190.375 ± 0.053	193.965 ± 0.078	198.856 ± 0.099	200.452 ± 0.011	204.046 ± 0.057
$T_{\text{conj},2}$ ^b	3976.3 ± 2.2	3932.5 ± 1.1	3877.5 ± 2.8	3954.2 ± 3.1	3937.5 ± 0.5	3932.0 ± 0.9
a_2 (au)	0.86762 ± 0.00033	0.87235 ± 0.00023	0.88328 ± 0.00027	0.89809 ± 0.00034	0.90281 ± 0.00016	0.91359 ± 0.00023
e_2	0.0826 ± 0.0038	0.0631 ± 0.0037	0.0728 ± 0.0028	0.0880 ± 0.0037	0.0271 ± 0.0011	0.0269 ± 0.0021
ω_2 (deg)	194.8 ± 1.6	181.3 ± 4.0	173.0 ± 3.2	198.7 ± 1.4	159.4 ± 5.5	134.6 ± 8.4
i_2 (deg)	88.20 ± 0.21	88.18 ± 0.19	89.67 ± 0.25	91.84 ± 0.20	91.79 ± 0.19	90.50 ± 0.32
Ω_2 (deg)	-0.88 ± 0.22	-0.74 ± 0.17	-2.18 ± 0.24	0.72 ± 0.17	0.32 ± 0.11	1.65 ± 0.15
T.A. ^c (deg)	152.4 ± 1.6	326.4 ± 4.0	272.2 ± 3.3	17.1 ± 2.0	160.1 ± 5.7	15.1 ± 7.7
M.A. ^c (deg)	147.7 ± 2.0	330.3 ± 3.4	280.5 ± 3.0	14.3 ± 1.8	159.1 ± 6.0	14.3 ± 7.3
M.L. ^c (deg)	346.3 ± 1.3	507.1 ± 1.0	443.0 ± 1.0	216.7 ± 1.1	319.9 ± 1.1	149.8 ± 1.3
I^d (deg)	1.50 ± 0.30	1.45 ± 0.25	2.37 ± 0.33	1.45 ± 0.26	1.26 ± 0.22	1.97 ± 0.30
Planet parameters						
M_3 (M_{\oplus})	823.9 ± 4.8	845.7 ± 4.7	837.0 ± 4.7	869.7 ± 5.0	942.0 ± 5.6	981.3 ± 5.7
R_3 (R_{\oplus})	11.24 ± 0.45	11.15 ± 0.41	11.30 ± 0.40	11.20 ± 0.43	11.25 ± 0.44	11.27 ± 0.40
ρ_3 (g cm^{-3})	3.19 ± 0.38	3.36 ± 0.37	3.18 ± 0.34	3.40 ± 0.40	3.64 ± 0.43	3.77 ± 0.40
Binary orbital parameters						
P_1 (days)	19.657444 ± 0.000027	19.658083 ± 0.000035	19.658171 ± 0.000030	19.656652 ± 0.000033	19.658173 ± 0.000025	19.658016 ± 0.000040
$T_{\text{conj},1}$ ^b	3878.1746 ± 0.0079	3878.3572 ± 0.0100	3878.3823 ± 0.0085	3877.9473 ± 0.0095	3878.3835 ± 0.0072	3878.3386 ± 0.0114
a_1 (au)	0.191934 ± 0.000038	0.191936 ± 0.000037	0.191936 ± 0.000032	0.191928 ± 0.000034	0.191915 ± 0.000034	0.191918 ± 0.000033
e_1	0.44780 ± 0.00018	0.44777 ± 0.00018	0.44789 ± 0.00015	0.44793 ± 0.00016	0.44790 ± 0.00017	0.44789 ± 0.00015
ω_1 (deg)	69.589 ± 0.012	69.599 ± 0.011	69.604 ± 0.010	69.578 ± 0.011	69.605 ± 0.011	69.602 ± 0.010
i_1 (deg)	89.4182 ± 0.0049	89.4198 ± 0.0051	90.5940 ± 0.0046	90.5795 ± 0.0046	90.5762 ± 0.0047	89.4077 ± 0.0055
T.A. ^c (deg)	214.796 ± 0.017	214.795 ± 0.016	214.784 ± 0.015	214.791 ± 0.015	214.780 ± 0.016	214.783 ± 0.014
M.A. ^c (deg)	254.508 ± 0.010	254.503 ± 0.010	254.499 ± 0.009	254.516 ± 0.010	254.492 ± 0.010	254.497 ± 0.009
M.L. ^c (deg)	284.384 ± 0.006	284.394 ± 0.006	284.388 ± 0.005	284.369 ± 0.005	284.384 ± 0.006	284.384 ± 0.005
Stellar parameters						
M_1 (M_{\odot})	1.2388 ± 0.0008	1.2388 ± 0.0007	1.2388 ± 0.0007	1.2388 ± 0.0007	1.2384 ± 0.0007	1.2384 ± 0.0007
M_2 (M_{\odot})	1.2024 ± 0.0007	1.2023 ± 0.0007	1.2023 ± 0.0006	1.2023 ± 0.0007	1.2019 ± 0.0007	1.2020 ± 0.0006
R_1 (R_{\odot})	1.3846 ± 0.0019	1.3841 ± 0.0020	1.3842 ± 0.0017	1.3843 ± 0.0017	1.3842 ± 0.0016	1.3844 ± 0.0016
R_2 (R_{\odot})	1.3153 ± 0.0013	1.3138 ± 0.0013	1.3134 ± 0.0011	1.3144 ± 0.0011	1.3124 ± 0.0012	1.3112 ± 0.0012
$\log g_1$	4.2484 ± 0.0012	4.2487 ± 0.0012	4.2487 ± 0.0010	4.2486 ± 0.0011	4.2485 ± 0.0010	4.2484 ± 0.0010
$\log g_2$	4.2801 ± 0.0009	4.2810 ± 0.0009	4.2813 ± 0.0007	4.2806 ± 0.0008	4.2818 ± 0.0008	4.2826 ± 0.0008
Long-term parameters						
apsidal precession period (yr)	42.314 ± 0.038	43.938 ± 0.029	43.442 ± 0.036	44.478 ± 0.036	49.261 ± 0.027	51.399 ± 0.038
nodal precession period (yr)	44.116 ± 0.038	46.050 ± 0.029	45.455 ± 0.035	46.640 ± 0.036	52.039 ± 0.027	54.384 ± 0.039
primary transit fraction	0.333 ± 0.125	0.320 ± 0.122	0.210 ± 0.047	0.330 ± 0.132	0.323 ± 0.124	0.230 ± 0.082
secondary transit fraction	0.398 ± 0.127	0.378 ± 0.105	0.234 ± 0.054	0.385 ± 0.121	0.396 ± 0.118	0.261 ± 0.109

Notes.^a Instantaneous parameters valid at BJD 2,453,250.0.^b BJD-2,455,000.^c True anomaly, mean anomaly, mean longitude.^d Mutual inclination between orbital planes.

of the determinations based on the PARSEC and MIST models ($T_1 = 6040$ K, $T_2 = 5970$ K, $[\text{Fe}/\text{H}] = +0.32$), and report them in Table 3.

We end this section with a note about the expected rotation of the stars. Given the 19.7 days orbital period, one might expect

the stars to have been tidally spun-down and thus be rotating slowly. The timescale for reaching spin-orbit synchronicity is approximately 1.5 Gyr, significantly shorter than the age of the system (though the timescale for orbital circularization is much longer). However, the binary is quite eccentric ($e = 0.45$) and

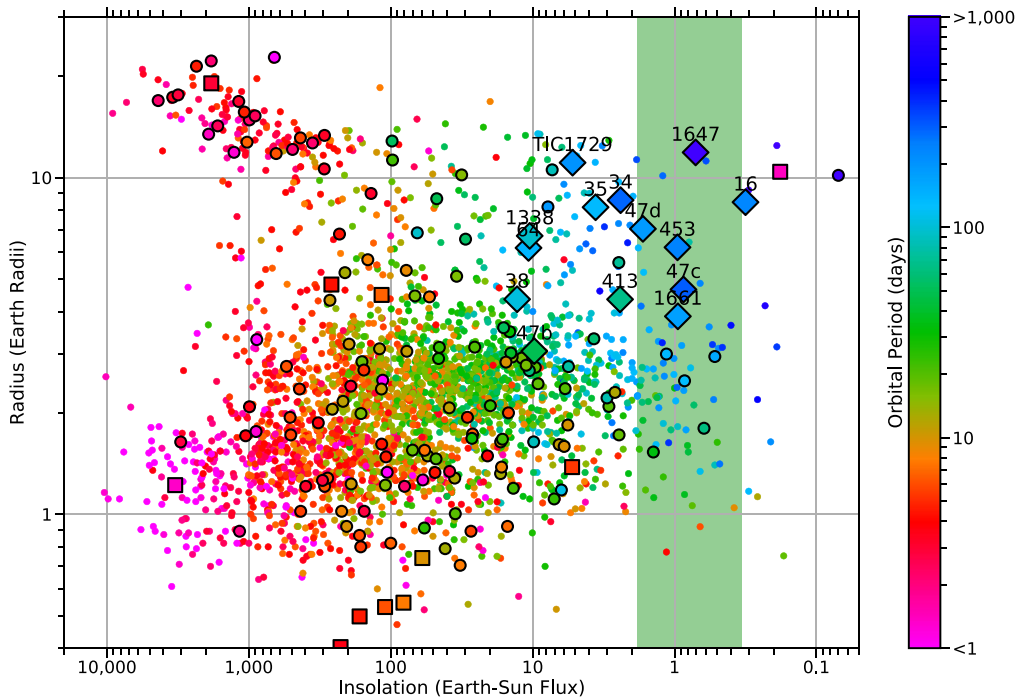


Figure 25. Planet radius vs. insolation, using the NExSci Exoplanet Archive confirmed transiting planet sample (as of 2021 June 27). The transiting circumbinary planets are shown as diamond symbols, and tend to lie in the large-radius and low-insolation portion of the diagram. Shown in green is the approximate position of the habitable zone, based on the “late Venus” and “early Mars” insulations (Kopparapu et al. 2014). Note that the insolation increases toward the left. For comparison, non-CBP planets that reside in binary star systems are outlined with circles, and planets in triple or higher systems are outlined in squares.

this means the equilibrium pseudosynchronous spin period (Hut 1981) is only about 8.3 days. The corresponding $V_{\text{rot}} \sin i$ is 8.4 km s^{-1} for the primary star. This somewhat relatively rapid spin may induce stellar activity that could be detected (e.g., starspot-induced photometric modulations, or the Mount Wilson Ca II H and K S -index). Such enhanced activity, persistent on a long timescale, is reminiscent of the “forever young” effect (Mason et al. 2013), where the stars remain more rapidly rotating, and hence active, than their ages would imply.

The observed far-ultraviolet excess in the SED (Figure 22) can be used as a check on these ideas. For simplicity we assume that both of the (nearly identical) stars in the system contribute equally to the observed excess. We then infer a chromospheric activity of $\log R'_{\text{HK}} = -4.8 \pm 0.2$ via the empirical relations of Findeisen et al. (2011), which in turn predicts a rotation period of 10.8 ± 2.0 days via the empirical rotation–activity relations of Mamajek & Hillenbrand (2008). The latter relations also imply an age of 3.5 ± 1.4 Gyr, consistent with that determined above.

4.2. Apsidal Motion, Transit Durations, Gaia EDR3 Astrometry

Based on the analysis of all available data, the observed phase change amounts to a change in the binary’s argument of periastron of 2.88×10^{-3} degrees per cycle. Precession due to the effects of General Relativity accounts for a change of 1.70×10^{-4} degrees per cycle, and precession due to tidal bulges (assuming zero obliquity) accounts for 2.32×10^{-5} degrees per cycle, assuming apsidal constants of $k_2 = 0.01$ for both stars (Torres et al. 2010). Thus we see that most of the apsidal precession must be accounted for by another source, which is the circumbinary body of planetary mass.

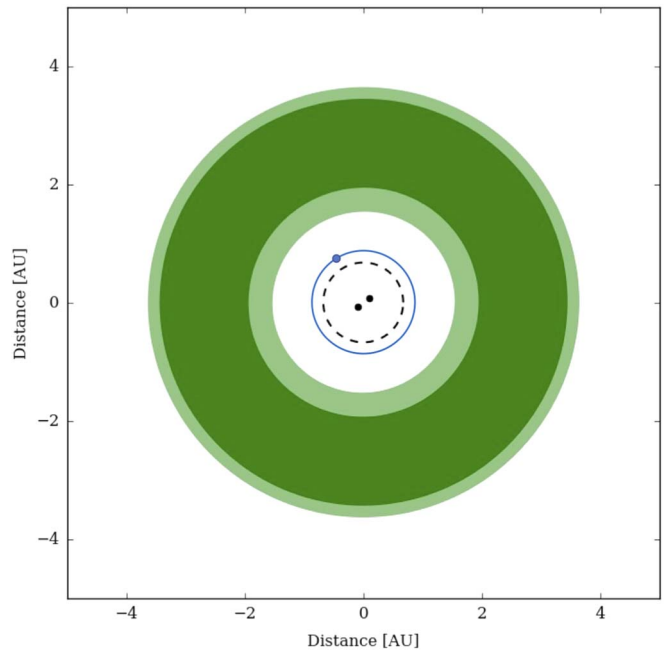


Figure 26. Conservative (dark green) and optimistic (light green) habitable zones of the TIC 1729 system. The orbit of the CBP is shown in blue. The dashed black circle represents the planet’s critical instability orbit. (Figure obtained using Binary-HZ calculator: <http://astro.twam.info/hz/>, Mueller & Haghighipour 2014.)

As mentioned above, the measured times of the two CBP transits, combined with the RV-derived stellar masses and EB orbital parameters, allow an analytical estimate of the planet’s orbital period (e.g., Kostov et al. 2020b) independent of the photodynamical analysis. Assuming $e_3 = [0.0, 0.2]$ for the eccentricity of the planet—the range for the known transiting

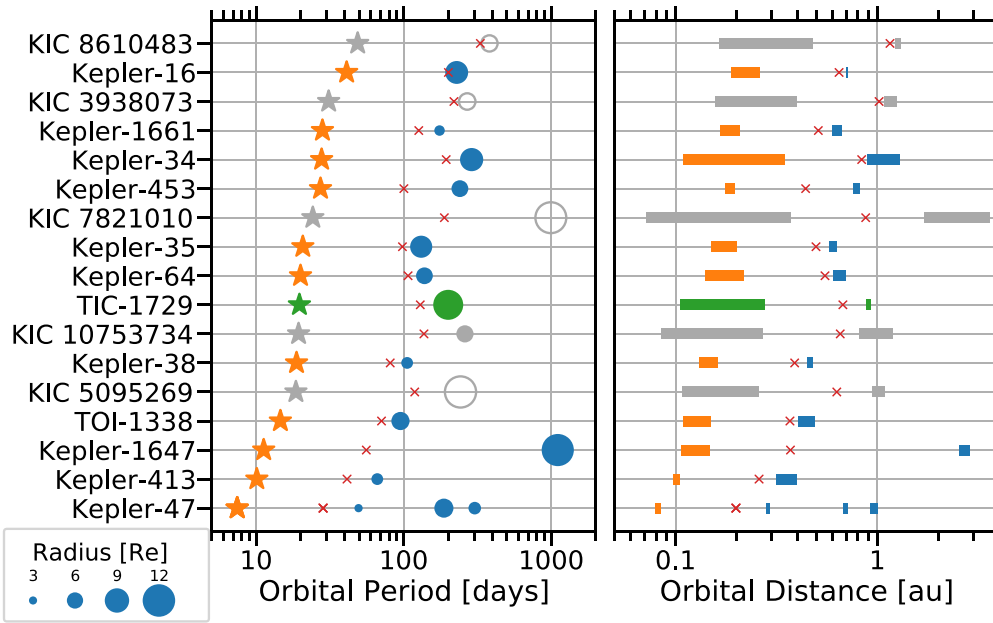


Figure 27. Periods and semimajor axes for all the currently known Kepler and TESS circumbinary planets and host stars. The orange and blue colors represent the binary stars and planets, respectively, with TIC 1729 shown in green, and the gray color representing the CBP candidates. The red “x” denotes the critical stability orbit. In the left-hand panel, the size of the blue dots represent the radius of the planet; the nontransiting planets are shown as gray circles with a radius estimated via a mass–radius relation. In the right-hand panel, the horizontal bars denote the range in orbital distance spanned, due to the eccentricity of the orbits.

CBPs (Welsh & Orosz 2018)—and taking into account orbital stability, the calculated period of the CBP, $P_{3,\text{calc}}$, ranges from ≈ 152 days to ≈ 340 days, with an average of 209.8 days and a median of 194.1 days (see Figure 24). This is in line with the CBP orbital periods corresponding to the families of solutions listed in Table 6, and further strengthens their validity.

Gaia measured an astrometric excess noise above a single-star model for TIC 1729 of 0.069 mas, with a significance of $\sigma = 5.707$ (Gaia EDR3, Gaia Collaboration et al. 2020). According to the catalog, there are 291 good observations ($N = \text{astrometric_n_good_obs_al}$) so the target falls in the large N limit and the excess noise is significant. At the measured parallax of 4.0608 mas, the astrometric excess noise for TIC 1729 corresponds to a measured physical displacement of $\Delta a_{\text{measured}} = 0.017$ au (Belokurov et al. 2020). We note that the binary has a high eccentricity ($e = 0.45$) and the two stars spend most of the time near apastron ($r_{\text{max}} = a(1 + e) = 0.27$ au). Accounting for the argument of periastron of the binary ($69^\circ.6$), the projected apastron is 0.25 au and thus the expected photocenter-induced physical displacement is $\Delta a_{\text{expected}} = 0.01$ au⁷⁵—comparable to the measured displacement. Additionally, Stassun & Torres (2021) have shown using a set of benchmark eclipsing binaries that the renormalized unit weight error (RUWE) statistic can be quantitatively used as an estimator of photocenter motion. Their empirical relation for the RUWE value for TIC 1729 (0.882) suggests a photocenter semimajor axis of ~ 0.064 mas, or 0.016 au at the distance of the system. Thus there is evidence for binarity based on Gaia’s astrometric excess noise as well as on RUWE.

4.3. TIC 172900988 in the Circumbinary Planet Context

Compared with single-star transiting exoplanets, the CBPs are required to have longer orbital periods and larger planetary

radii. The longer period is due to the stability requirement around the binary, coupled with the lack of CBPs around the shortest-period binaries (Armstrong et al. 2014; Martin & Triaud 2015; Welsh et al. 2014). The larger radius is possibly a detection bias against finding smaller planets due to the CBPs’ being intrinsically more difficult to detect than planets orbiting a single star (see, e.g., Windemuth et al. 2019; Martin & Fabrycky 2021). Yet the CBPs have smaller radii, on average, than the hot Jupiter subset. The observed radius distribution of the known CBPs may be an interesting combination of orbital migration history and observational bias against detecting planets that have not migrated or have been scattered to longer periods (see, e.g., Pierens & Nelson 2008; Pierens & Nelson 2013; Kley & Haghighipour 2015; Kley et al. 2019; Penzlin et al. 2021). In general, the currently known CBPs experience low insolation, and a sizeable fraction of them are in the habitable zone of their host binaries, likely a fortuitous consequence of the bias of the Kepler sample toward G- and K-type stars. A comparison of the radii and insulations of the CBPs versus those of other transiting exoplanets is shown in Figure 25 (for CBP habitability see also Kane & Hinkel 2013). As seen in the figure, CBPs tend to reside in the larger-radius and lower-insolation portion of the diagram. However, it is difficult to know if the CBPs have a different parent population because of the different detection biases and small sample size. For comparison, the figure also marks planets that have two or more host stars but are not circumbinary (i.e., S-type planets). S-type planets in binary star systems are outlined with circles and those in triple or higher-order stellar systems are outlined with squares. Of the 2761 planets with radius and insolation estimates shown in the figure, 137 (5.0%) are in multiple star systems. Currently there are 125 (4.5%) noncircumbinary planets in multiple star systems, roughly a factor of 10 more than the circumbinary planets. Unlike the circumbinary planets, these S-type planets do not appear to favor any particular region in the diagram; they seem to follow the single-star

⁷⁵ Taking into account the binary mass ratio of 0.97 and luminosity ratio of 0.87.

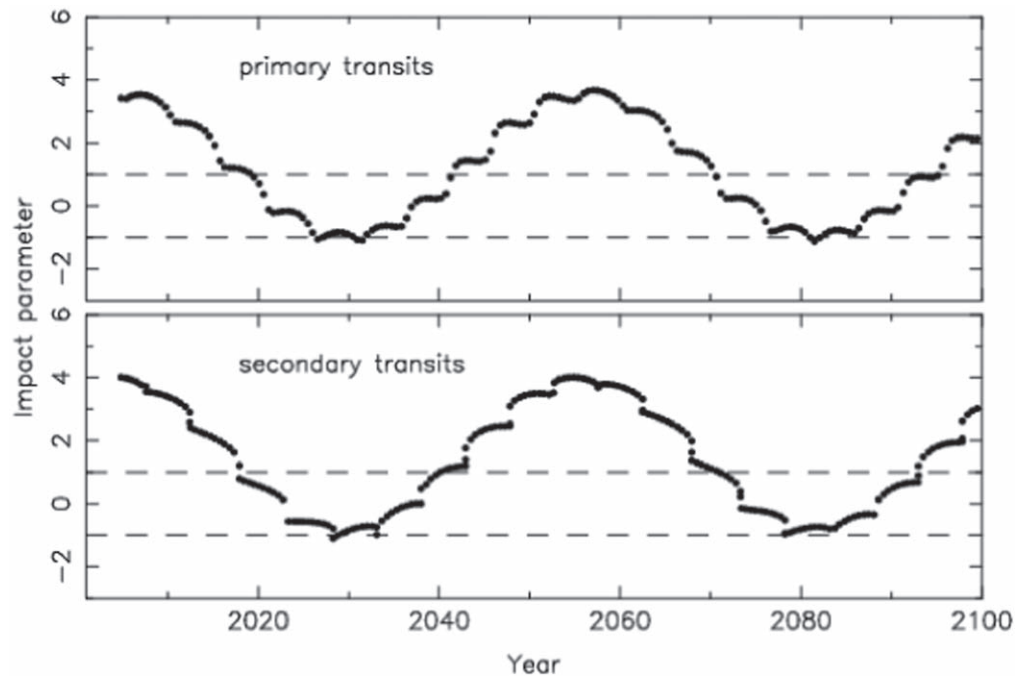


Figure 28. Evolution of the CBP impact parameter b over the course of 100 yr for the primary (upper panel) and secondary transits (lower) for Family 5. Transits occur when b is in between the two dashed lines, e.g., $|b| < 1$. The planet produces transits for $\approx 40\%$ of its precession cycle for this solution.

distribution. Certainly this population does not show a tendency for experiencing low insolation or residing in the habitable zone. TIC 1729 b itself is too hot to be in the habitable zone, given its mean insolation of $\sim 5.2 S_{\oplus}$. Figure 26 shows a schematic birds-eye view of the TIC 1729 system, with the habitable zone region shown in green.

With solar-like stars in a moderately high eccentricity ($e = 0.45$) 19.7 days orbit, the binary hosting TIC 1729 b falls neatly into the distribution of known CBP systems, albeit with a higher than typical metallicity. The planet’s orbit has a small mutual inclination and the ~ 200 days period is typical of the known CBP population. The planet is close to the critical (in) stability radius: $a/a_{\text{crit}} = 1.34$ ($P/P_{\text{crit}} = 1.55$) using either the more sophisticated interpolation scheme in Quarles et al. (2018)⁷⁶ or the approximation given in Holman & Wiegert (1999). In Figure 27 we show TIC 1729 b in comparison with the other known CBPs. With the notable exception of Kepler 1647 and KIC 7821010, the figure shows the accumulation of the orbits of the currently known CBPs near their boundaries of stability. This figure includes five candidate CBPs presented at various conferences going back as far as the Extreme Solar Systems II meeting.⁷⁷ One of the candidates, KIC 10753734, is transiting (Orosz et al. 2016) and four others do not transit: KIC 7821010, KIC 8610483, KIC 3938073 (presented as a group for the first time at the “Toward Other Earths II” conference⁷⁸), and KIC 5095269 (discovered by Getley et al. 2017). For consistency with the other 16 systems shown in Figure 27, we use our own preliminary photodynamical values for KIC 5095269 (J. Orosz et al. 2021, in preparation). The nontransiting planets are

detected by their gravitational perturbation of the binary star’s orbit, as manifested by eclipse timing variations (ETVs). While such a planet’s radius is unknown, its mass is measurable by the pattern it produces in the ETVs (e.g., Borkovits et al. 2015). For the nontransiting cases, we used an approximate radius obtained by employing the mass–radius relation given in Bashi et al. (2017). While TIC 1729 b has the second-largest radius of the published circumbinary planets, exceeded only by Kepler 1647 b, its radius is in no way atypical. Where TIC 1729 b does differ from the published CBP is its mass: with a mass $\approx 2.9 M_{\text{Jup}}$, it is the most massive transiting CBP known, a factor of 2 times larger than the next most massive planet, Kepler 1647b. However, both candidate CBPs KIC 7821010 and KIC 5095269 likely have comparable or larger masses.

4.4. Near-term “Transitability” and Long-term Dynamical Stability

Models from the posterior samples for the six families were integrated using the GRK12 routine in ELC starting at day -1700 and going out to day 200,000 (i.e., from BJD 2,453,300 to BJD 2,655,000, which is about 530 yr into the future) in order to investigate near-term variations in the orbital elements and transit probabilities. For each model, the conjunction times and impact parameters for various combinations of the bodies over that time span are computed (e.g., primary eclipse, secondary eclipse, transits of the primary, etc.) and saved. In addition, the instantaneous values of the orbital elements and the Cartesian coordinates of all of the bodies are recorded every 10 days. A Lomb–Scargle periodogram was computed for the planet’s orbital inclination time series to find the precession period of the planet’s orbital plane. The results are given in Table 6. The precessional periods are between about 44 yr for Family 1 to about 54 yr for Family 6. Both the binary’s inclination and the planet’s orbital inclination vary with the same ≈ 50 yr period (depending on the family), but are out of phase. The

⁷⁶ We note that the stability limit is not a sharp boundary and has dependencies on the planet eccentricity, mutual inclination, and locations of mean motion resonances; see Figure 30.

⁷⁷ 2011 September 11–17, Grand Teton National Park, WY.

⁷⁸ Slides of the talk presented at “Toward Other Earths II, The Star-Planet Connection,” 2014 September 15–19, Porto, Portugal are available at <https://www.astro.up.pt/investigacao/conferencias/toe2014/files/wwelsh.pdf>.

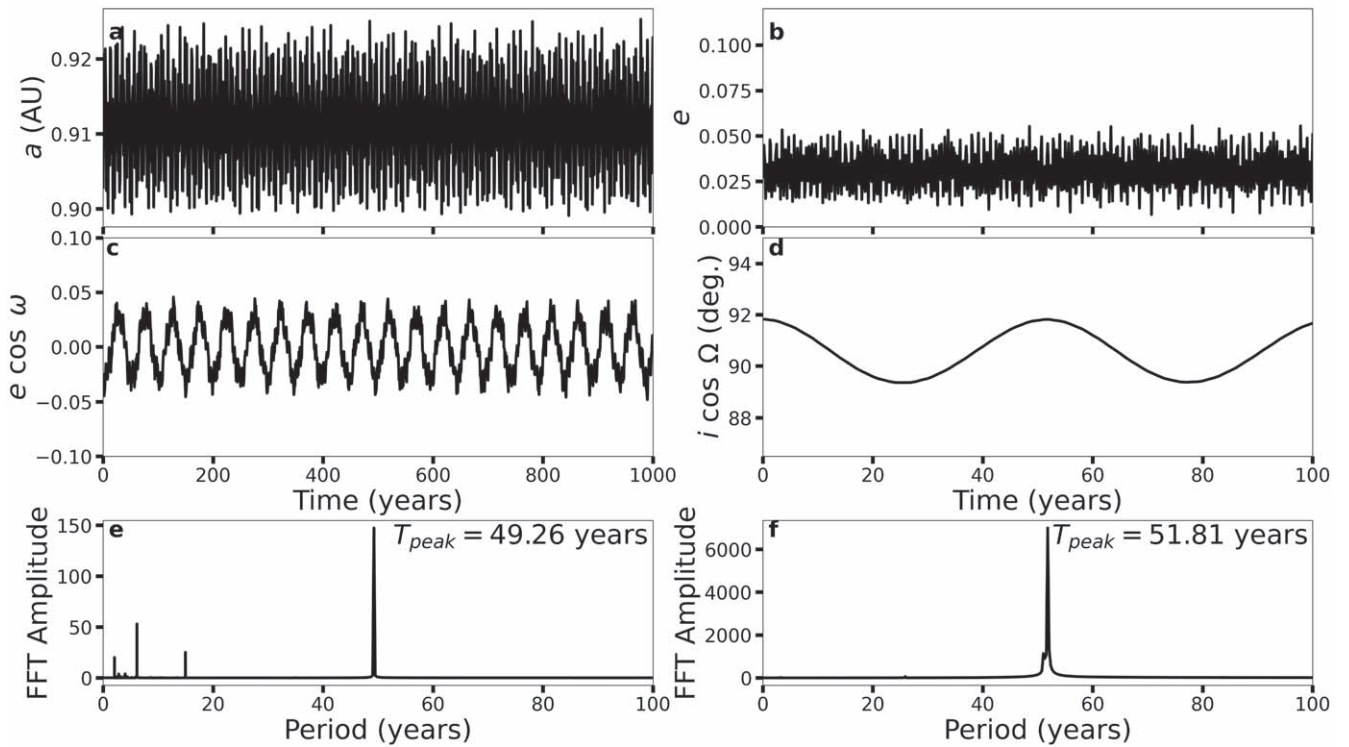


Figure 29. Short-term (1000 yr) orbital evolution of the planet using Family 5 for the (a) semimajor axis, (b) eccentricity, (c) x -component of eccentricity vector, and (d) x -component of (sky) inclination vector. The simulations are extended to 10,000 yr to calculate the periodogram of the (e) apsidal and (f) nodal precession.

binary’s inclination varies by only about $0^{\circ}.5$, and as such the binary will always be eclipsing.

However, the inclination of the planet’s orbit varies by $\approx 5^{\circ}$, and this is a large enough change that transits will not always be possible (see also Schneider 1994, Kostov et al. 2014; Martin 2017). Figure 28 shows the impact parameter b of the (inferior) conjunctions of the planet with the primary and with the secondary over the span of about 100 yr (using the Family 5 solution). Only $\approx 40\%$ of the conjunctions have $|b| < 1$, which is a necessary condition to have an observable transit. As seen from Table 6, the transit fractions η_{prim} and η_{sec} are about 15% and 40%. This transit fraction is consistent with the rough average of $\approx 36\%$ for the first 10 known CBP systems (Martin 2017). Given that TESS observed TIC 1729 for only one sector out of thirteen in the Northern Hemisphere sky during its second year of operation, we were fortunate that TESS was able to observe the transits. Overall, the expected yield of TESS CBPs producing two (or more) transits during a single conjunction from Cycles 1 and 2 is on the order of a hundred (Kostov et al. 2020b).

We performed 3-body integrations to understand both the short- and long-term evolution of Family 5 better. We used the `ias15` integrator in REBOUND (Rein & Liu 2012) for the short-term (1000 yr) integrations, which shows the planetary semimajor axis and eccentricity vary in time (Figures 29(a) and (b)). These variations are bounded with a small amplitude, which is indicative of long-term stability (i.e., no secular growth). As a result the x -component of the eccentricity (Figure 29(c)) and inclination (29(d)) vectors also show a well-behaved evolution, where the small-scale variations in the eccentricity (Figure 29(c)) are due to the 3-body interaction with the inner binary. As mentioned in the discussion of “transitability,” the orbital plane of the planet precesses over several

decades. Thus, we extended the initial short-term integrations to 10,000 yr and identified the dominant secular frequencies (transformed to periods) using the `fft` module from `scipy`. Figures 29(e) and (f) illustrate the periodograms associated with the evolution of the planetary eccentricity and inclination vectors, respectively. The secular cycle for the planetary eccentricity using Family 5 is ≈ 49.3 yr, while the inclination is a little longer (≈ 51.8 yr). There is a longer variation in the inclination over ≈ 4000 yr (not shown in Figure 29(d)), where this envelope expands slightly in the range of inclination variation to $\approx 88^{\circ}.8$ – $92^{\circ}.3$ without changing the mean value.

The long-term evolution of Family 5 used a different approach, where we investigated the stability of many initial conditions using 10^5 yr integrations with the well-established `mercury6` code that is modified to efficiently evolve planets in binary systems (Chambers et al. 2002). These simulations keep the binary solution for Family 5 fixed while varying the planetary semimajor axis and eccentricity in the planetary solution in the ranges 0.45–1.0 au (0.001 au steps) and 0.0–0.36 (0.002 steps), respectively. A simulation is terminated if the planet collides with the inner binary (i.e., pericenter crosses the inner binary orbits), escapes the system (i.e., distance to the center of mass is greater than 10 au), or the full simulation time (10^5 yr) elapses. We use these simulations to measure the amplitude of eccentricity variation ($e_{\text{max}} - e_{\text{min}}$) of a planet for a given initial condition in semimajor axis a_p and eccentricity e_p . This technique is similar to using the chaos indicator MEGNO (Cincotta & Simó 2000), but is less computationally expensive. Figure 30 illustrates the nominal location of the binary $N:1$ mean motion resonances (MMRs) with gray curves, which typically shape the parameter space that stable CBPs can inhabit (Mardling 2013). The white cells denote initial conditions that undergo an instability, where the

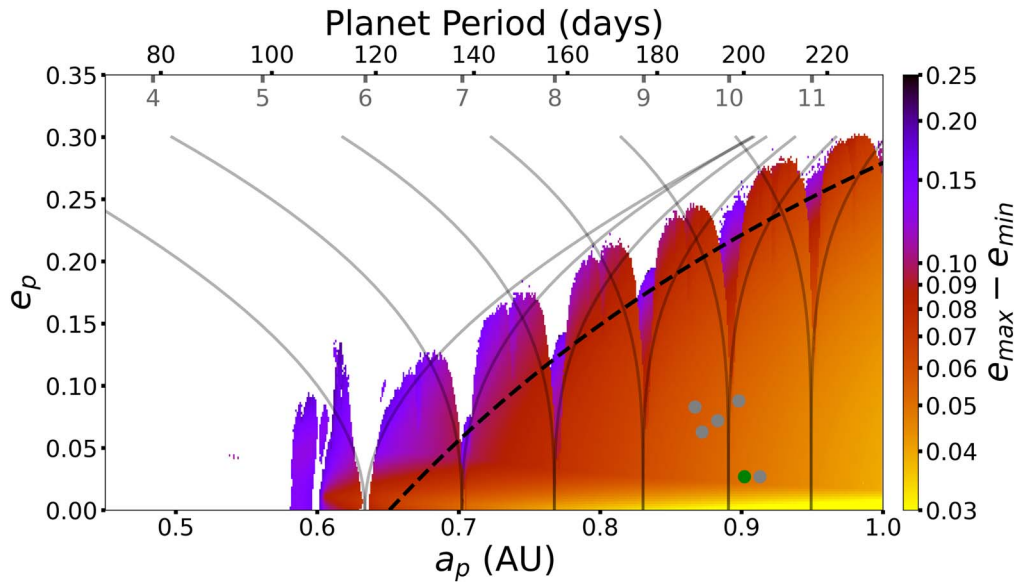


Figure 30. Amplitude of eccentricity variation (colored cells) for a planet using the Family 5 solution, where the white cells denote unstable initial conditions. The black dashed curve marks the stability limit using the fitting function from Quarles et al. (2018). The upper axis shows corresponding planet period for a given semimajor axis. The nominal location of the $N:1$ mean motion resonances are marked (gray ticks) and the potential libration regions for each resonance are indicated (gray curves).

colored cells show the amplitude of eccentricity oscillations. The dashed curve marks the estimate for the stability boundary accounting for planetary eccentricity using Quarles et al. (2018). The green dot marks the nominal parameters for Family 5 (just outside the 10:1 MMR), where the parameters for other Families (gray dots) also lie in the stable regions around the 10:1 MMR. Note that solutions for interior to Family 5 have elevated eccentricity. All six Families represent stable 3-body solutions as long as the planetary eccentricity remains low ($e_p \lesssim 0.15$) despite the forced eccentricity (~ 0.02 , yellow strip in Figure 30) from the inner binary.

5. Conclusions

We presented the discovery of a new transiting CBP from TESS, TIC 17290098 b. The target was observed in a single sector and the planet produced just two transits—one across each star—during the same conjunction. The host system is a double-lined spectroscopic binary exhibiting primary and secondary eclipses. Extensive archival data from multiple surveys (ASAS-SN, KELT, SuperWASP) shows clear apsidal motion of the EB caused by the gravitational perturbation from the CBP. The host binary star has an orbital period of 19.7 days, eccentricity of 0.45, stellar masses of 1.24 and $1.2M_{\odot}$, respectively, and stellar radii of 1.38 and $1.31R_{\odot}$ for the primary and secondary stars, respectively. We estimated an age for the system of about 3.1 Gyr and a metallicity of $[\text{Fe}/\text{H}] = +0.34$. The CBP is slightly larger than Jupiter ($R_3 = 11.07R_{\oplus}$). The orbital period and mass of the CBP cannot be uniquely constrained from the available data, and are between about 190–205 days and about $820\text{--}980M_{\oplus}$, respectively.

We note that TESS will observe the target again in Sectors 44 through 47 (2021 October to 2022 January). Unfortunately, it will miss the predicted transits for the corresponding conjunctions by several weeks. Thus follow-up observations from other instruments are key for strongly constraining the orbit and mass of the CBP. In particular, observing the predicted 2022 February–March conjunction of the CBP is critical for solving the currently ambiguous orbit of the planet.

As a relatively bright target ($V = 10.141$ mag), the system is accessible for high-resolution spectroscopy, e.g., Rossiter–McLaughlin effect, transit spectroscopy. TIC 172900988 demonstrates the discovery potential of TESS for circumbinary planets with orbital periods greatly exceeding the duration of the observing window.

This paper includes data collected by the TESS mission, which are publicly available from the Mikulski Archive for Space Telescopes (MAST). Funding for the TESS mission is provided by NASA’s Science Mission directorate.

V.B.K. is thankful for support from NASA grants 80NSSC20K0054 and 80NSSC20K0850. This material is based upon work supported by the National Science Foundation under Grant NSF AST-1617004 to W.F.W. and J.A.O.. We are also deeply grateful to John Hood, Jr. for his generous support of exoplanet research at San Diego State University. D.J.S. is supported as an Eberly Research Fellow by the Eberly College of Science at The Pennsylvania State University. The Center for Exoplanets and Habitable Worlds is supported by The Pennsylvania State University, the Eberly College of Science, and the Pennsylvania Space Grant Consortium. N.H. acknowledges support from NASA XRP through grant No. 80NSSC18K051. Support for this work was provided by NASA through the NASA Hubble Fellowship grant HF2-51464 awarded by the Space Telescope Science Institute, which is operated by the Association of Universities for Research in Astronomy, Inc., for NASA, under contract NAS5-26555.

Resources supporting this work were provided by the NASA High-End Computing (HEC) Program through the NASA Center for Climate Simulation (NCCS) at Goddard Space Flight Center, and through the NASA Advanced Supercomputing (NAS) Division at Ames Research Center for the production of the SPOC data products. Personnel directly supporting this effort were Mark L. Carroll, Laura E. Carriere, Ellen M. Salmon, Nicko D. Acks, Matthew J. Stroud, Bruce E. Pfaff, Lyn E. Gerner, Timothy M. Burch, and Savannah L.

Table 7
Future Transit Times for TIC 172900988

Type	Time (BJD-2,455,000)	Date	Impact Parameter	Duration (hr)	Fraction ^a
Family 1					
secondary	4443.242 ± 0.055	2021-Aug-16T17:47:51.6	-0.202 ± 0.181	6.90 ± 0.22	0.999
primary	4446.986 ± 0.047	2021-Aug-20T11:40:07.1	0.364 ± 0.258	5.84 ± 0.93	0.980
primary	4627.972 ± 0.075	2022-Feb-17T11:20:20.0	-0.032 ± 0.174	7.50 ± 0.17	0.999
secondary	4633.473 ± 0.076	2022-Feb-22T23:20:52.3	0.423 ± 0.284	6.55 ± 1.43	0.935
secondary	4815.934 ± 0.090	2022-Aug-24T10:24:29.3	0.172 ± 0.268	6.60 ± 0.59	0.993
primary	4819.611 ± 0.121	2022-Aug-28T02:39:53.9	0.688 ± 0.192	6.79 ± 2.36	0.748
primary	5000.753 ± 0.096	2023-Feb-25T06:03:38.0	0.300 ± 0.249	5.89 ± 0.73	0.987
secondary	5006.108 ± 0.122	2023-Mar-02T14:35:54.6	0.675 ± 0.213	5.59 ± 1.98	0.699
Family 2					
primary	4450.728 ± 0.063	2021-Aug-24T05:27:45.9	-0.196 ± 0.116	6.86 ± 0.18	1.000
secondary	4456.259 ± 0.063	2021-Aug-29T18:13:25.7	0.303 ± 0.247	7.05 ± 0.87	0.997
secondary	4640.479 ± 0.095	2022-Mar-01T23:29:57.8	-0.053 ± 0.173	7.42 ± 0.13	1.000
primary	4644.060 ± 0.059	2022-Mar-05T13:25:45.9	0.433 ± 0.236	4.64 ± 0.81	0.987
primary	4828.391 ± 0.295	2022-Sep-05T21:22:51.5	0.265 ± 0.175	17.41 ± 1.25	1.000
secondary	4832.467 ± 0.105	2022-Sep-09T23:12:04.5	0.385 ± 0.267	6.11 ± 1.09	0.985
primary	5019.279 ± 0.091	2023-Mar-15T18:42:07.3	0.404 ± 0.239	4.33 ± 0.70	0.991
secondary	5024.002 ± 0.177	2023-Mar-20T12:02:36.6	0.761 ± 0.197	5.96 ± 2.34	0.596
secondary	5208.615 ± 0.161	2023-Sep-21T02:45:45.6	0.473 ± 0.266	5.82 ± 1.37	0.957
primary	5212.035 ± 0.300	2023-Sep-24T12:49:52.5	0.845 ± 0.164	6.93 ± 3.00	0.416
Family 3					
primary	4449.224 ± 0.035	2021-Aug-22T17:22:15.6	0.448 ± 0.188	4.28 ± 0.59	1.000
secondary	4454.023 ± 0.065	2021-Aug-27T12:32:32.8	0.863 ± 0.171	4.60 ± 2.15	0.215
secondary	4637.931 ± 0.068	2022-Feb-27T10:20:48.6	0.824 ± 0.176	3.73 ± 1.68	0.517
primary	4640.460 ± 0.213	2022-Mar-01T23:02:21.2	0.799 ± 0.210	13.67 ± 5.98	0.486
primary	4823.802 ± 0.080	2022-Sep-01T07:15:07.5	0.685 ± 0.205	4.54 ± 1.49	0.891
secondary	4829.183 ± 0.086	2022-Sep-06T16:24:06.6	0.878 ± 0.301	3.59 ± 2.64	0.016
secondary	5012.856 ± 0.122	2023-Mar-09T08:33:01.8	0.896 ± 0.149	3.04 ± 1.49	0.131
primary	5016.576 ± 0.120	2023-Mar-13T01:50:02.7	0.901 ± 0.242	3.29 ± 2.51	0.024
primary	5198.892 ± 0.183	2023-Sep-11T09:24:18.5	0.812 ± 0.187	5.41 ± 2.41	0.510
secondary	5204.216 ± 0.092	2023-Sep-16T17:11:40.5	0.839 ± 0.207	3.49 ± 1.49	0.003
Family 4					
primary	4453.397 ± 0.055	2021-Aug-26T21:32:15.6	0.155 ± 0.108	13.26 ± 0.24	1.000
secondary	4458.314 ± 0.027	2021-Aug-31T19:31:47.3	-0.129 ± 0.236	6.69 ± 0.07	1.000
secondary	4650.489 ± 0.049	2022-Mar-11T23:44:09.6	-0.599 ± 0.234	7.40 ± 2.28	0.862
primary	4645.755 ± 0.025	2022-Mar-07T06:06:41.2	-0.112 ± 0.197	4.69 ± 0.19	1.000
secondary	4835.720 ± 0.048	2022-Sep-13T05:16:44.6	-0.165 ± 0.237	6.67 ± 0.47	0.999
primary	4839.456 ± 0.056	2022-Sep-16T22:57:07.2	-0.687 ± 0.195	6.25 ± 2.18	0.782
primary	5023.646 ± 0.115	2023-Mar-20T03:30:19.1	-0.337 ± 0.207	12.90 ± 1.39	0.999
secondary	5028.440 ± 0.057	2023-Mar-24T22:33:12.8	-0.548 ± 0.256	5.60 ± 1.62	0.888
primary	5215.911 ± 0.046	2023-Sep-28T09:52:06.6	-0.520 ± 0.247	4.08 ± 1.01	0.939
secondary	5220.660 ± 0.087	2023-Oct-03T03:50:31.7	-0.796 ± 0.178	5.46 ± 2.28	0.453
Family 5					
secondary	4481.592 ± 0.037	2021-Sep-24T02:11:55.6	0.219 ± 0.108	6.61 ± 0.14	1.000
primary	4485.298 ± 0.062	2021-Sep-27T19:09:34.5	-0.406 ± 0.220	9.28 ± 1.36	0.983
secondary	4679.413 ± 0.053	2022-Apr-09T21:55:06.1	0.111 ± 0.120	7.20 ± 0.08	0.999
primary	4683.134 ± 0.046	2022-Apr-13T15:13:15.3	-0.395 ± 0.231	5.22 ± 0.79	0.980
secondary	4877.460 ± 5.128	2022-Oct-24T23:03:06.4	-0.149 ± 0.213	9.03 ± 0.34	1.000
primary	4880.550 ± 0.045	2022-Oct-28T01:12:12.2	-0.376 ± 0.236	4.15 ± 0.61	0.980
primary	5077.879 ± 0.053	2023-May-13T09:05:52.0	-0.374 ± 0.239	4.16 ± 0.62	0.980
secondary	5082.223 ± 0.121	2023-May-17T17:21:11.4	-0.748 ± 0.199	7.25 ± 1.89	0.720
Family 6					
primary	4490.701 ± 0.076	2021-Oct-03T04:48:49.6	0.083 ± 0.154	8.30 ± 0.22	1.000
secondary	4496.278 ± 0.065	2021-Oct-08T18:40:33.7	-0.683 ± 0.303	5.23 ± 2.02	0.727
secondary	4696.304 ± 0.082	2022-Apr-26T19:18:12.4	-0.671 ± 0.291	4.90 ± 1.83	0.805
primary	4696.776 ± 0.478	2022-Apr-27T06:37:06.6	-0.378 ± 0.313	35.99 ± 6.87	0.984

Table 7
(Continued)

Type	Time (BJD–2,455,000)	Date	Impact Parameter	Duration (hr)	Fraction ^a
secondary	4896.416 ± 0.130	2022-Nov-12T21:59:25.6	–0.560 ± 0.281	6.60 ± 1.86	0.942
primary	4899.879 ± 0.072	2022-Nov-16T09:05:09.3	–0.719 ± 0.300	3.33 ± 1.39	0.569
primary	5098.752 ± 0.112	2023-Jun-03T06:02:39.7	–0.629 ± 0.300	4.57 ± 1.62	0.856
secondary	5104.164 ± 0.155	2023-Jun-08T15:55:26.7	–0.803 ± 0.248	4.69 ± 2.11	0.136

Note.^a Fraction of posterior sample with observable transits.**Table 8**
Future Primary Eclipses for TIC 172900988, Family 1

Cycle	Time (BJD–2,455,000)	Date (UT)	Duration (hr)
313	4369.78998 ± 0.00004	2021-Jun-04T06:57:34.2	6.1608 ± 0.0052
314	4389.44763 ± 0.00007	2021-Jun-23T22:44:35.2	6.1621 ± 0.0052
315	4409.10436 ± 0.00004	2021-Jul-13T14:30:16.3	6.1616 ± 0.0052
316	4428.76285 ± 0.00004	2021-Aug-02T06:18:30.2	6.1604 ± 0.0052
317	4448.42189 ± 0.00005	2021-Aug-21T22:07:31.5	6.1604 ± 0.0052
318	4468.08001 ± 0.00005	2021-Sep-10T13:55:13.2	6.1612 ± 0.0052
319	4487.73732 ± 0.00005	2021-Sep-30T05:41:44.6	6.1617 ± 0.0052
320	4507.39453 ± 0.00005	2021-Oct-19T21:28:07.3	6.1613 ± 0.0052
321	4527.05248 ± 0.00004	2021-Nov-08T13:15:34.2	6.1604 ± 0.0052
322	4546.71157 ± 0.00005	2021-Nov-28T05:04:39.3	6.1600 ± 0.0052

Table 9
Future Secondary Eclipses for TIC 172900988, Family 1

Cycle	Time (BJD–2,455,000)	Date (UT)	Duration (hr)
313	4362.01453 ± 0.00011	2021-May-27T12:20:55.3	14.8352 ± 0.0106
314	4381.67141 ± 0.00011	2021-Jun-16T04:06:49.5	14.8338 ± 0.0106
315	4401.33021 ± 0.00011	2021-Jul-05T19:55:30.2	14.8329 ± 0.0107
316	4420.98881 ± 0.00010	2021-Jul-25T11:43:52.8	14.8345 ± 0.0107
317	4440.64583 ± 0.00011	2021-Aug-14T03:29:59.7	14.8355 ± 0.0107
318	4460.30277 ± 0.00011	2021-Sep-02T19:15:58.9	14.8349 ± 0.0107
319	4479.96048 ± 0.00011	2021-Sep-22T11:03:05.7	14.8338 ± 0.0107
320	4499.61886 ± 0.00011	2021-Oct-12T02:51:09.1	14.8335 ± 0.0107
321	4519.27721 ± 0.00011	2021-Oct-31T18:39:11.2	14.8346 ± 0.0107
322	4538.93466 ± 0.00011	2021-Nov-20T10:25:54.3	14.8359 ± 0.0107

Table 10
Future Primary Eclipses for TIC 172900988, Family 2

Cycle	Time (BJD–2,455,000)	Date (UT)	Duration (hr)
313	4369.78969 ± 0.00005	2021-Jun-04T06:57:09.5	6.1560 ± 0.0058
314	4389.44783 ± 0.00008	2021-Jun-23T22:44:52.9	6.1572 ± 0.0058
315	4409.10459 ± 0.00006	2021-Jul-13T14:30:36.6	6.1574 ± 0.0058
316	4428.76238 ± 0.00004	2021-Aug-02T06:17:49.7	6.1562 ± 0.0058
317	4448.42138 ± 0.00005	2021-Aug-21T22:06:47.1	6.1557 ± 0.0058
318	4468.07998 ± 0.00006	2021-Sep-10T13:55:10.0	6.1563 ± 0.0058
319	4487.73758 ± 0.00006	2021-Sep-30T05:42:06.9	6.1570 ± 0.0058
320	4507.39469 ± 0.00007	2021-Oct-19T21:28:20.9	6.1570 ± 0.0058
321	4527.05226 ± 0.00005	2021-Nov-08T13:15:15.0	6.1562 ± 0.0058
322	4546.71104 ± 0.00005	2021-Nov-28T05:03:53.7	6.1554 ± 0.0058

Table 11
Future Secondary Eclipses for TIC 172900988, Family 2

Cycle	Time (BJD-2,455,000)	Date (UT)	Duration (hr)
313	4362.01482 ± 0.00010	2021-May-27T12:21:20.1	14.8254 ± 0.0117
314	4381.67151 ± 0.00010	2021-Jun-16T04:06:58.7	14.8244 ± 0.0117
315	4401.32977 ± 0.00011	2021-Jul-05T19:54:52.4	14.8231 ± 0.0117
316	4420.98866 ± 0.00009	2021-Jul-25T11:43:40.4	14.8240 ± 0.0117
317	4440.64622 ± 0.00009	2021-Aug-14T03:30:33.7	14.8255 ± 0.0117
318	4460.30304 ± 0.00010	2021-Sep-02T19:16:22.8	14.8255 ± 0.0117
319	4479.96037 ± 0.00010	2021-Sep-22T11:02:55.8	14.8244 ± 0.0117
320	4499.61855 ± 0.00010	2021-Oct-12T02:50:43.0	14.8236 ± 0.0117
321	4519.27709 ± 0.00010	2021-Oct-31T18:39:00.6	14.8242 ± 0.0117
322	4538.93496 ± 0.00010	2021-Nov-20T10:26:20.6	14.8257 ± 0.0117

Table 12
Future Primary Eclipses for TIC 172900988, Family 3

Cycle	Time (BJD-02,455,000)	Date (UT)	Duration (hr)
313	4232.18215 ± 0.00004	2021-Jan-17T16:22:18.0	6.1570 ± 0.0044
314	4251.84096 ± 0.00004	2021-Feb-06T08:10:58.8	6.1561 ± 0.0044
315	4271.49978 ± 0.00005	2021-Feb-25T23:59:40.9	6.1565 ± 0.0044
316	4291.15765 ± 0.00005	2021-Mar-17T15:47:01.2	6.1573 ± 0.0044
317	4310.81482 ± 0.00005	2021-Apr-06T07:33:20.4	6.1576 ± 0.0044
318	4330.47215 ± 0.00005	2021-Apr-25T23:19:54.0	6.1570 ± 0.0044
319	4350.13061 ± 0.00003	2021-May-15T15:08:04.3	6.1560 ± 0.0044
320	4369.78988 ± 0.00004	2021-Jun-04T06:57:25.2	6.1563 ± 0.0044
321	4389.44777 ± 0.00007	2021-Jun-23T22:44:47.0	6.1575 ± 0.0044
322	4409.10452 ± 0.00005	2021-Jul-13T14:30:30.2	6.1574 ± 0.0044

Table 13
Future Secondary Eclipses for TIC 172900988, Family 3

Cycle	Time (BJD-02,455,000)	Date (UT)	Duration (hr)
313	4224.41118 ± 0.00008	2021-Jan-09T21:52:05.9	14.8319 ± 0.0090
314	4244.06916 ± 0.00008	2021-Jan-29T13:39:34.9	14.8339 ± 0.0090
315	4263.72605 ± 0.00009	2021-Feb-18T05:25:30.4	14.8344 ± 0.0090
316	4283.38316 ± 0.00009	2021-Mar-09T21:11:44.6	14.8334 ± 0.0090
317	4303.04111 ± 0.00009	2021-Mar-29T12:59:12.1	14.8326 ± 0.0090
318	4322.69965 ± 0.00009	2021-Apr-18T04:47:29.4	14.8333 ± 0.0090
319	4342.35782 ± 0.00009	2021-May-07T20:35:15.2	14.8352 ± 0.0090
320	4362.01477 ± 0.00009	2021-May-27T12:21:15.9	14.8360 ± 0.0090
321	4381.67157 ± 0.00009	2021-Jun-16T04:07:03.7	14.8348 ± 0.0090
322	4401.33006 ± 0.00010	2021-Jul-05T19:55:17.4	14.8342 ± 0.0090

Table 14
Future Primary Eclipses for TIC 172900988, Family 4

Cycle	Time (BJD-02,455,000)	Date (UT)	Duration (hr)
313	4369.78957 ± 0.00004	2021-Jun-04T06:56:58.7	6.1577 ± 0.0047
314	4389.44805 ± 0.00005	2021-Jun-23T22:45:11.2	6.1589 ± 0.0047
315	4409.10486 ± 0.00005	2021-Jul-13T14:30:59.5	6.1594 ± 0.0047
316	4428.76234 ± 0.00004	2021-Aug-02T06:17:46.5	6.1583 ± 0.0047
317	4448.42129 ± 0.00005	2021-Aug-21T22:06:39.0	6.1575 ± 0.0047
318	4468.08005 ± 0.00005	2021-Sep-10T13:55:16.5	6.1580 ± 0.0047
319	4487.73781 ± 0.00005	2021-Sep-30T05:42:26.5	6.1588 ± 0.0047
320	4507.39493 ± 0.00006	2021-Oct-19T21:28:42.1	6.1590 ± 0.0047
321	4527.05233 ± 0.00005	2021-Nov-08T13:15:21.6	6.1583 ± 0.0047
322	4546.71086 ± 0.00004	2021-Nov-28T05:03:38.0	6.1573 ± 0.0047

Table 15
Future Secondary Eclipses for TIC 172900988, Family 4

Cycle	Time (BJD-02,455,000)	Date (UT)	Duration (hr)
313	4362.01493 ± 0.00009	2021-May-27T12:21:30.3	14.8303 ± 0.0097
314	4381.67153 ± 0.00010	2021-Jun-16T04:07:00.0	14.8296 ± 0.0097
315	4401.32948 ± 0.00010	2021-Jul-05T19:54:27.0	14.8281 ± 0.0097
316	4420.98848 ± 0.00009	2021-Jul-25T11:43:24.7	14.8286 ± 0.0097
317	4440.64629 ± 0.00009	2021-Aug-14T03:30:39.5	14.8302 ± 0.0097
318	4460.30310 ± 0.00010	2021-Sep-02T19:16:28.1	14.8305 ± 0.0097
319	4479.96028 ± 0.00010	2021-Sep-22T11:02:48.1	14.8295 ± 0.0097
320	4499.61833 ± 0.00010	2021-Oct-12T02:50:23.9	14.8285 ± 0.0097
321	4519.27687 ± 0.00010	2021-Oct-31T18:38:41.6	14.8289 ± 0.0097
322	4538.93495 ± 0.00010	2021-Nov-20T10:26:19.8	14.8304 ± 0.0098

Table 16
Future Primary Eclipses for TIC 172900988, Family 5

Cycle	Time (BJD-02,455,000)	Date (UT)	Duration (hr)
313	4369.78853 ± 0.00004	2021-Jun-04T06:55:29.0	6.1528 ± 0.0047
314	4389.44775 ± 0.00004	2021-Jun-23T22:44:45.6	6.1530 ± 0.0047
315	4409.10584 ± 0.00005	2021-Jul-13T14:32:24.6	6.1541 ± 0.0047
316	4428.76281 ± 0.00004	2021-Aug-02T06:18:27.0	6.1544 ± 0.0047
317	4448.42022 ± 0.00004	2021-Aug-21T22:05:06.8	6.1535 ± 0.0047
318	4468.07879 ± 0.00004	2021-Sep-10T13:53:27.8	6.1527 ± 0.0047
319	4487.73773 ± 0.00005	2021-Sep-30T05:42:19.9	6.1528 ± 0.0047
320	4507.39587 ± 0.00005	2021-Oct-19T21:30:03.2	6.1537 ± 0.0047
321	4527.05304 ± 0.00005	2021-Nov-08T13:16:22.6	6.1542 ± 0.0047
322	4546.71021 ± 0.00005	2021-Nov-28T05:02:42.1	6.1536 ± 0.0047

Table 17
Future Secondary Eclipses for TIC 172900988, Family 5

Cycle	Time (BJD-02,455,000)	Date (UT)	Duration (hr)
313	4362.01555 ± 0.00009	2021-May-27T12:22:23.2	14.8238 ± 0.0103
314	4381.67250 ± 0.00010	2021-Jun-16T04:08:23.6	14.8247 ± 0.0103
315	4401.32930 ± 0.00010	2021-Jul-05T19:54:11.5	14.8238 ± 0.0103
316	4420.98735 ± 0.00010	2021-Jul-25T11:41:47.1	14.8225 ± 0.0103
317	4440.64611 ± 0.00010	2021-Aug-14T03:30:23.6	14.8228 ± 0.0103
318	4460.30415 ± 0.00010	2021-Sep-02T19:17:58.6	14.8243 ± 0.0103
319	4479.96117 ± 0.00010	2021-Sep-22T11:04:04.8	14.8251 ± 0.0103
320	4499.61809 ± 0.00010	2021-Oct-12T02:50:03.1	14.8243 ± 0.0103
321	4519.27589 ± 0.00010	2021-Oct-31T18:37:16.7	14.8231 ± 0.0103
322	4538.93452 ± 0.00010	2021-Nov-20T10:25:42.8	14.8230 ± 0.0103

Table 18
Future Primary Eclipses for TIC 172900988, Family 6

Cycle	Time (BJD-02,455,000)	Date (UT)	Duration (hr)
313	4369.78821 ± 0.00004	2021-Jun-04T06:55:01.5	6.1514 ± 0.0047
314	4389.44736 ± 0.00004	2021-Jun-23T22:44:11.5	6.1509 ± 0.0048
315	4409.10606 ± 0.00005	2021-Jul-13T14:32:43.2	6.1518 ± 0.0048
316	4428.76341 ± 0.00007	2021-Aug-02T06:19:19.0	6.1526 ± 0.0048
317	4448.42044 ± 0.00005	2021-Aug-21T22:05:25.9	6.1523 ± 0.0048
318	4468.07838 ± 0.00004	2021-Sep-10T13:52:52.4	6.1513 ± 0.0048
319	4487.73727 ± 0.00005	2021-Sep-30T05:41:40.5	6.1509 ± 0.0048
320	4507.39600 ± 0.00005	2021-Oct-19T21:30:14.5	6.1514 ± 0.0048
321	4527.05368 ± 0.00006	2021-Nov-08T13:17:17.8	6.1523 ± 0.0048
322	4546.71066 ± 0.00006	2021-Nov-28T05:03:20.9	6.1524 ± 0.0048

Table 19
Future Secondary Eclipses for TIC 172900988, Family 6

Cycle	Time (BJD−02,455,000)	Date (UT)	Duration (hr)
313	4362.01554 ± 0.00009	2021-May-27T12:22:22.9	14.8311 ± 0.0103
314	4381.67298 ± 0.00009	2021-Jun-16T04:09:05.2	14.8328 ± 0.0103
315	4401.32963 ± 0.00010	2021-Jul-05T19:54:40.3	14.8325 ± 0.0103
316	4420.98706 ± 0.00010	2021-Jul-25T11:41:22.1	14.8311 ± 0.0103
317	4440.64561 ± 0.00010	2021-Aug-14T03:29:40.8	14.8309 ± 0.0103
318	4460.30415 ± 0.00010	2021-Sep-02T19:17:58.5	14.8325 ± 0.0103
319	4479.96169 ± 0.00010	2021-Sep-22T11:04:49.9	14.8342 ± 0.0103
320	4499.61851 ± 0.00010	2021-Oct-12T02:50:38.9	14.8342 ± 0.0103
321	4519.27571 ± 0.00010	2021-Oct-31T18:37:01.3	14.8330 ± 0.0103
322	4538.93396 ± 0.00010	2021-Nov-20T10:24:54.0	14.8323 ± 0.0103

Table 20
Initial Dynamical Parameters, Family 1 Solution^a

Parameter ^b	Orbit 1	Orbit 2
Period (days)	1.96574580221424142E+01	1.88789475383543561E+02
$e \cos \omega$	1.56170869428264247E−01	−7.84627636359548492E−02
$e \sin \omega$	4.19679141794474964E−01	−1.95706955564456352E−02
i (rad)	1.56065838061355966E+00	1.54077852290273420E+00
Ω (rad)	0.00000000000000000E+00	−1.39615402591776010E−02
T_{conj} (days) ^c	3.87817840712633324E+03	3.97504901993195290E+03
a (au)	1.91922057111088368E−01	8.67437940438783306E−01
e	4.47794509250981132E−01	8.08666643429462734E−02
ω (deg)	6.95887754265467748E+01	1.94005315149095878E+02
true anomaly (deg)	2.14795791997321089E+02	1.52599413335829297E+02
mean anomaly (deg)	2.54508036598815352E+02	1.48094540591452386E+02
mean longitude (deg)	2.84384567423867907E+02	3.45804791152572307E+02
i (deg)	8.94191384708786217E+01	8.82801065267277210E+01
Ω (deg)	0.00000000000000000E+00	−7.99937332352862018E−01

Parameter ^d	body 1	body 2	body 3
Mass (M_{\odot})	1.23855333251973199E+00	1.20216020381416144E+00	2.47248739828866224E−03
x (au)	−3.06081938367827738E−02	2.96795061441613300E−02	9.02071058130503922E−01
y (au)	1.19305835485099677E−03	−1.19000678898439839E−03	−1.90446258039909458E−02
z (au)	1.15993046787125756E−01	−1.19062797707022411E−01	−2.14770554349837495E−01
v_x (au day ^{−1})	−1.85584244286306627E−02	1.91052733765369812E−02	7.27974838035594634E−03
v_y (au day ^{−1})	−1.39291603333074979E−04	1.42119901856559741E−04	6.75105288472446622E−04
v_z (au day ^{−1})	−1.36979028799990733E−02	1.40593823850855386E−02	2.58659627721818629E−02

Notes.^a Reference time = −1750.00000, integration step size = 0.05000 days.^b Jacobian instantaneous (Keplerian) elements.^c Times are relative to BJD 2,455,000.000.^d Barycentric Cartesian coordinates.

Strong. This research has made use of the Exoplanet Follow-up Observation Program website, which is operated by the California Institute of Technology, under contract with the National Aeronautics and Space Administration under the Exoplanet Exploration Program. Resources supporting this work were provided by the NASA High-End Computing (HEC) Program through the NASA Advanced Supercomputing (NAS) Division at Ames Research Center for the production of the SPOC data products. This research was supported in part through research cyberinfrastructure resources and services provided by the Partnership for an Advanced Computing Environment (PACE) at the Georgia Institute of Technology. This is University of Texas Center for Planetary Systems Habitability contribution #0035.

This work has made use of data from the European Space Agency (ESA) mission Gaia (<https://www.cosmos.esa.int/gaia>), processed by the Gaia Data Processing and Analysis Consortium (DPAC, <https://www.cosmos.esa.int/web/gaia/dpac/consortium>). Funding for the DPAC has been provided by national institutions, in particular the institutions participating in the Gaia Multilateral Agreement. This work makes use of observations from the LCOGT network. LCOGT telescope time was granted by NOIRLab through the Mid-Scale Innovations Program (MSIP). MSIP is funded by NSF. Based in part on observations obtained with the Apache Point Observatory 3.5 m telescope, which is owned and operated by the Astrophysical Research Consortium. Based in part on observations made at Observatoire de Haute Provence (CNRS),

Table 21
Initial Dynamical Parameters, Family 2 Solution^a

Parameter ^b	Orbit 1	Orbit 2
Period (days)	1.96581050348207640E+01	1.90344409654595211E+02
$e \cos \omega$	1.56095399121964296E-01	-6.41839330129671676E-02
$e \sin \omega$	4.19562643942974267E-01	-3.41531319824112719E-03
i (rad)	1.56069168597231789E+00	1.53995695080737560E+00
Ω (rad)	0.0000000000000000E+00	-1.23272607174403446E-02
T_{conj} (days) ^c	3.87836379440340716E+03	3.93178612576113301E+03
a (au)	1.91935253129229433E-01	8.72243497642089749E-01
e	4.47659006186029829E-01	6.42747354817963384E-02
ω (deg)	6.95926282414263540E+01	1.83045912695301638E+02
true anomaly (deg)	2.14804271728057756E+02	3.24164173494033321E+02
mean anomaly (deg)	2.54507023924052760E+02	3.28312436731456785E+02
mean longitude (deg)	2.84396899969484082E+02	5.06503786177268239E+02
i (deg)	8.94210467273706371E+01	8.82330339130979553E+01
Ω (deg)	0.0000000000000000E+00	-7.06300012066742977E-01

parameter ^d	body 1	body 2	body 3
Mass (M_{\odot})	1.23865008563608670E+00	1.20240624074018676E+00	2.54202204119478945E-03
x (au)	-2.89989640535398066E-02	3.13384111311550972E-02	-6.93122161080714894E-01
y (au)	1.14666117155765176E-03	-1.22840795182390088E-03	2.23182286318032649E-02
z (au)	1.15309882199540956E-01	-1.19729475461112553E-01	4.46445001440231859E-01
v_x (au day ⁻¹)	-1.85374662427125192E-02	1.91290459164667540E-02	-1.55191574714838246E-02
v_y (au day ⁻¹)	-1.37562887969058562E-04	1.43005132355077748E-04	-6.12890294872434787E-04
v_z (au day ⁻¹)	-1.36493848720297753E-02	1.41159237785312384E-02	-2.60670849525854072E-02

Notes.^a Reference time = -1750.00000, integration step size = 0.05000 days.^b Jacobian instantaneous (Keplerian) elements.^c Times are relative to BJD 2,455,000.000.^d Barycentric Cartesian coordinates.

Table 22
Initial Dynamical Parameters, Family 3 Solution^a

Parameter ^b	Orbit 1	Orbit 2
Period (days)	1.96581966864200162E+01	1.93904791889272900E+02
$e \cos \omega$	1.56121806427791304E-01	-7.08444993703360865E-02
$e \sin \omega$	4.19668697760405940E-01	1.08423492641878030E-02
i (rad)	1.58116590285353231E+00	1.56931046735959434E+00
Ω (rad)	0.0000000000000000E+00	-3.38391048322012472E-02
T_{conj} (days) ^c	3.87839003218881726E+03	3.87537072364502910E+03
a (au)	1.91945485746299049E-01	8.83128528073461538E-01
e	4.47767611962044176E-01	7.16693772025415871E-02
ω (deg)	6.95941932123379985E+01	1.71298721780941207E+02
true anomaly (deg)	2.14795441024058704E+02	2.74646126215441598E+02
mean anomaly (deg)	2.54504198476389234E+02	2.82789419717797102E+02
mean longitude (deg)	2.84389634236396660E+02	4.44006010106996939E+02
i (deg)	9.05941329434997300E+01	8.99148665254074899E+01
Ω (deg)	0.0000000000000000E+00	-1.93883788938588131E+00

parameter ^d	body 1	body 2	body 3
Mass (M_{\odot})	1.23902297233212821E+00	1.20240102867346055E+00	2.52147590926568360E-03
x (au)	-2.97692203634119038E-02	3.05464886787758655E-02	6.17172221993351131E-02
y (au)	-1.19976916867427967E-03	1.23797844739104482E-03	-7.95168071186067743E-04
z (au)	1.14876961143937931E-01	-1.20201139078512154E-01	8.70434422401247354E-01
v_x (au day ⁻¹)	-1.85204348360698545E-02	1.91450868478993050E-02	-2.88830443386271958E-02
v_y (au day ⁻¹)	1.40774477895423434E-04	-1.47112457600004489E-04	9.77744149518047908E-04
v_z (au day ⁻¹)	-1.36726091131929104E-02	1.40890481761541085E-02	-3.66336001417871924E-02

Notes.^a Reference time = -1750.00000, integration step size = 0.05000 days.^b Jacobian instantaneous (Keplerian) elements.^c Times are relative to BJD 2,455,000.000.^d Barycentric Cartesian coordinates.

Table 23
Initial Dynamical Parameters, Family 4 Solution^a

Parameter ^b	Orbit 1	Orbit 2
Period (days)	1.96566477698221753E+01	1.98857206991129431E+02
$e \cos \omega$	1.56289724178110490E-01	-8.40521311420768802E-02
$e \sin \omega$	4.19818036408871220E-01	-2.78742314301126115E-02
i (rad)	1.58093148741641842E+00	1.60390271144704388E+00
Ω (rad)	0.0000000000000000E+00	1.36027426644736976E-02
T_{conj} (days) ^c	3.87794613658087519E+03	3.95443034920364471E+03
a (au)	1.91930046466682352E-01	8.98087983771095555E-01
e	4.47966138874212660E-01	8.85535630414952535E-02
ω (deg)	6.95807237358540789E+01	1.98347083790672144E+02
true anomaly (deg)	2.14786792939669255E+02	1.73373556051096500E+01
mean anomaly (deg)	2.54512430957598497E+02	1.44954035862529889E+01
mean longitude (deg)	2.84367516675523348E+02	2.16463819140258664E+02
i (deg)	9.05807019283003854E+01	9.18968561155047183E+01
Ω (deg)	0.0000000000000000E+00	7.79379744476882963E-01

parameter ^d	body 1	body 2	body 3
Mass (M_{\odot})	1.23900170636175599E+00	1.20221789267038504E+00	2.60954702249461146E-03
x (au)	-2.89464716999712768E-02	3.12794468249556618E-02	-6.66775804910971437E-01
y (au)	-1.1807499088969556E-03	1.20216567347655365E-03	6.77744802185890893E-03
z (au)	1.16293056699475289E-01	-1.18812639065407483E-01	-4.78479643436138524E-01
v_x (au day ⁻¹)	-1.85677966845622412E-02	1.90981829330462670E-02	1.73802332586521120E-02
v_y (au day ⁻¹)	1.37359014083570014E-04	-1.43907711936180395E-04	1.08079039193696648E-03
v_z (au day ⁻¹)	-1.36389941853373095E-02	1.41116360952543637E-02	-2.54926771978428897E-02

Notes.^a Reference time = -1750.00000, integration step size = 0.05000 days.^b Jacobian instantaneous (Keplerian) elements.^c Times are relative to BJD 2,455,000.000.^d Barycentric Cartesian coordinates.

Table 24
Initial Dynamical Parameters, Family 5 Solution^a

Parameter ^b	Orbit 1	Orbit 2
Period (days)	1.96581697466411960E+01	2.00453455776095382E+02
$e \cos \omega$	1.56120265129208902E-01	-2.53238980408201642E-02
$e \sin \omega$	4.19765514968936770E-01	1.03126288031170597E-02
i (rad)	1.58078123663466807E+00	1.60276140444680815E+00
Ω (rad)	0.0000000000000000E+00	6.15744651978666815E-03
T_{conj} (days) ^c	3.87838264397195871E+03	3.93739746952321866E+03
a (au)	1.91925787812358140E-01	9.02849883123379215E-01
e	4.47857817550560366E-01	2.73431915623053474E-02
ω (deg)	6.95986966505942490E+01	1.57842415515142477E+02
true anomaly (deg)	2.14784117775033934E+02	1.61873909957105752E+02
mean anomaly (deg)	2.54494715844195582E+02	1.60879788562848717E+02
mean longitude (deg)	2.84382814425628169E+02	3.20069121170409460E+02
i (deg)	9.05720931926375528E+01	9.18314640412624783E+01
Ω (deg)	0.0000000000000000E+00	3.52795698161293025E-01

parameter ^d	body 1	body 2	body 3
Mass (M_{\odot})	1.23872067209601799E+00	1.20195846007516960E+00	2.84367305505320387E-03
x (au)	-3.05117762048147702E-02	2.97755496161732185E-02	7.05634622502878561E-01
y (au)	-1.18334732414564496E-03	1.16402958706238267E-03	2.34631694465425554E-02
z (au)	1.16468463181218757E-01	-1.18616173378369855E-01	-5.97881635138625467E-01
v_x (au day ⁻¹)	-1.85668502216597038E-02	1.90921472185390795E-02	1.79954987672769490E-02
v_y (au day ⁻¹)	1.37117431317775707E-04	-1.39996410566221895E-04	-5.55734287033887329E-04
v_z (au day ⁻¹)	-1.36914505868482791E-02	1.40608913970410084E-02	2.08446965916781538E-02

Notes.^a Reference time = -1750.00000, integration step size = 0.05000 days.^b Jacobian instantaneous (Keplerian) elements.^c Times are relative to BJD 2,455,000.000.^d Barycentric Cartesian coordinates.

Table 25
Initial Dynamical Parameters, Family 6 Solution^a

Parameter ^b	Orbit 1	Orbit 2
Period (days)	1.96580278267864692E+01	2.04044351487866408E+02
$e \cos \omega$	1.56130598769293610E-01	-2.03399939845695932E-02
$e \sin \omega$	4.19636617208692664E-01	1.32000037143129752E-02
i (rad)	1.56039566396540219E+00	1.58295631134958925E+00
Ω (rad)	0.00000000000000000E+00	3.01046537868270951E-02
T_{conj} (days) ^c	3.87834172008000996E+03	3.93188579064755913E+03
a (au)	1.91938897677575687E-01	9.13681045402537806E-01
e	4.47740610593246102E-01	2.42477927521248318E-02
ω (deg)	6.95917073329280527E+01	1.47017722156016418E+02
true anomaly (deg)	2.14797706768949269E+02	6.42833095688426615E-01
mean anomaly (deg)	2.54505026854790316E+02	6.12217097320448711E-01
mean longitude (deg)	2.84389414101877321E+02	1.49385424857392564E+02
i (deg)	8.94040859157313861E+01	9.06967157939281634E+01
Ω (deg)	0.00000000000000000E+00	1.72486960568772396E+00

parameter ^d	body 1	body 2	body 3
Mass (M_{\odot})	1.23884162569136502E+00	1.20237293468549433E+00	2.95621181546849420E-03
x (au)	-2.87948280961208697E-02	3.15166528469546653E-02	-7.51819850433428138E-01
y (au)	1.23863285644749575E-03	-1.20629020343918417E-03	-2.84347857229910010E-02
z (au)	1.15200082179167565E-01	-1.19865215145484580E-01	4.76296524896512863E-01
v_x (au day ⁻¹)	-1.85331209302203349E-02	1.91331285091844751E-02	-1.54096579736414628E-02
v_y (au day ⁻¹)	-1.42010521096675851E-04	1.46731256297197537E-04	-1.68170095547856991E-04
v_z (au day ⁻¹)	-1.36436249042942107E-02	1.41172371312928042E-02	-2.43194286919287544E-02

Notes.

^a Reference time = -1750.00000, integration step size = 0.05000 days.

^b Jacobian instantaneous (Keplerian) elements.

^c Times are relative to BJD 2,455,000.000.

^d Barycentric Cartesian coordinates.

France. The SOPHIE observations were obtained under an OHP DDT program (PI Triaud) and this work received funding from the European Research Council (ERC) under the European Union's Horizon 2020 research and innovation program (grant agreement No. 803193/BEBOP) as well as from the Leverhulme Trust (research project grant No. RPG-2018-418). This work makes use of observations from CHEOPS, which is an ESA mission in partnership with Switzerland with important contributions to the payload and the ground segment from Austria, Belgium, France, Germany, Hungary, Italy, Portugal, Spain, Sweden, and the United Kingdom. We thank Kate Isaak, the ESA CHEOPS Project Science Scientist, and the CHEOPS Science Operations Centre for their help and support with the CHEOPS observations.

The ongoing AAVSO Photometric All-Sky Survey (APASS) is funded by the Robert Martin Ayers Sciences Fund.






























Facilities: Gaia, CHEOPS, MAST, TESS, ASAS-SN, Evryscope, KELT, WASP, NCCS, LCOGT.

Software: AstroImageJ (Collins et al. 2017), ELC (Orosz et al. 2019), eleanor (Feinstein et al. 2019), EXOFASTv2 (Eastman et al. 2019), TAPIR (Jensen et al. 2013), mercury6 (Chambers et al. 2002), Rebound (Rein & Liu 2012; Rein & Spiegel 2015) <http://astrutils.astronomy.ohio-state.edu/time/>.

Appendix

Here we provide additional information for the predicted future eclipses and transits, as well as initial dynamical parameters.

ORCID iDs

Veselin B. Kostov  <https://orcid.org/0000-0001-9786-1031>
 Brian P. Powell  <https://orcid.org/0000-0003-0501-2636>
 Jerome A. Orosz  <https://orcid.org/0000-0001-9647-2886>
 William F. Welsh  <https://orcid.org/0000-0003-2381-5301>
 William Cochran  <https://orcid.org/0000-0001-9662-3496>
 Karen A. Collins  <https://orcid.org/0000-0001-6588-9574>
 Michael Endl  <https://orcid.org/0000-0002-7714-6310>
 Coel Hellier  <https://orcid.org/0000-0002-3439-1439>
 David W. Latham  <https://orcid.org/0000-0001-9911-7388>
 Joshua Pepper  <https://orcid.org/0000-0002-3827-8417>
 Billy Quarles  <https://orcid.org/0000-0002-9644-8330>
 Lalitha Sairam  <https://orcid.org/0000-0001-8102-3033>
 Guillermo Torres  <https://orcid.org/0000-0002-5286-0251>
 Robert F. Wilson  <https://orcid.org/0000-0002-4235-6369>
 David R. Ciardi  <https://orcid.org/0000-0002-5741-3047>
 Kevin I. Collins  <https://orcid.org/0000-0003-2781-3207>
 Dennis M. Conti  <https://orcid.org/0000-0003-2239-0567>
 Nader Haghighipour  <https://orcid.org/0000-0002-5234-6375>
 Eric G. Hintz  <https://orcid.org/0000-0002-9867-7938>
 Ward S. Howard  <https://orcid.org/0000-0002-0583-0949>
 Eric L. N. Jensen  <https://orcid.org/0000-0002-4625-7333>
 John F. Kielkopf  <https://orcid.org/0000-0003-0497-2651>
 Ethan Kruse  <https://orcid.org/0000-0002-0493-1342>
 Nicholas M. Law  <https://orcid.org/0000-0001-9380-6457>
 David Martin  <https://orcid.org/0000-0002-7595-6360>
 Pierre F. L. Maxted  <https://orcid.org/0000-0003-3794-1317>
 Benjamin T. Montet  <https://orcid.org/0000-0001-7516-8308>
 Felipe Murgas  <https://orcid.org/0000-0001-9087-1245>
 Greg Olmschenk  <https://orcid.org/0000-0001-8472-2219>

- Rucinski, S. 2002, *AJ*, **124**, 1746
- Santos, N. C., Adibekyan, V., Figueira, P., et al. 2017, *A&A*, **603**, A30
- Schlafly, E. F., & Finkbeiner, D. P. 2011, *ApJ*, **737**, 103
- Schneider, J., & Chevreton, M. 1990, *A&A*, **232**, 251
- Shappee, B. J., Prieto, J. L., Grupe, D., et al. 2014, *ApJ*, **788**, 48
- Short, D. R., Orosz, J. A., Welsh, W. F., & Windmiller, G. 2018, *AJ*, **156**, 297
- Siverd, R. J., Beatty, T. G., Pepper, J., et al. 2012, *ApJ*, **761**, 123
- Skilling, J. 2006, *BayAn*, **1**, 833
- Socia, Q. J., Welsh, W. F., & Orosz, J. A. 2020, *AJ*, **159**, 94
- Stassun, K. G., Oelkers, R. J., Pepper, J., et al. 2018, *AJ*, **156**, 102
- Stassun, K. G., & Torres, G. 2016, *AJ*, **152**, 180
- Stassun, K. G., & Torres, G. 2021, *ApJL*, **907**, L33
- Szentgyorgyi, A. H., & Furész, G. 2007, *Rev. Mex. Astron. Astrofís.*, **28**, 129
- Tegmark, M., Strauss, M. A., Blanton, M. R., et al. 2004, *PhRvD*, **69**, 103501
- Ter Braak, C. J. F. 2006, *Statistic. Comput*, **16**, 239
- Torres, G., Andersen, J., & Giménez, A. 2010, *ARA&A*, **18**, 67
- Torres, G., Fischer, D. A., Sozzetti, A., et al. 2012, *ApJ*, **757**, 161
- Torres, G., Neuhäuser, R., & Guenther, E. W. 2002, *AJ*, **123**, 1701
- Tull, R. G., MacQueen, P. J., Sneden, C., & Lambert, D. L. 1995, *PASP*, **107**, 251
- Wang, S.-i., Hildebrand, R. H., Hobbs, L. M., et al. 2003, *Proc. SPIE*, **4841**, 1145
- Welsh, W. F., & Orosz, J. A. 2018, in *Handbook of Exoplanets*, ed. H. J. Deeg & J. A. Belmonte
- Welsh, W. F., Orosz, J. A., Carter, J. A., et al. 2012, *Natur*, **481**, 475
- Welsh, W. F., Orosz, J. A., Carter, J. A., et al. 2014, *Formation, Detection, and Characterization of Extrasolar Habitable Planets*, Vol. 293 (Cambridge: Cambridge Univ. Press), 125
- Welsh, W. F., Orosz, J. A., Short, D. R., et al. 2015, *ApJ*, **809**, 26
- Windemuth, D., Agol, E., Carter, J., et al. 2019, *MNRAS*, **490**, 1313
- Ziegler, C., Tokovinin, A., Latiolais, M., et al. 2021, *AJ*, **162**, 192
- Zucker, S., & Mazeh, T. 1994, *ApJ*, **420**, 806